Additive Manufacturing of Graphene-based Patterns

by

Elahe Jabari

A thesis
presented to the University of Waterloo
in fulfilment of the
thesis requirement for the degree of
Doctor of Philosophy
in
Mechanical and Mechatronics Engineering

Waterloo, Ontario, Canada, 2016

Author’s Declaration

I hereby declare that I am the sole author of this thesis. This is a true copy of the thesis, including any required final revisions, as accepted by my examiners.

I understand that my thesis may be made electronically available to the public.

Abstract

The focus of this dissertation is on the deployment and characterization of a micro-scale aerosol-jet additive manufacturing technology to print highly conductive and flexible graphene-based patterns. For this purpose, a highly concentrated graphene ink with a viscosity of 21 cP and 3.1 mg/ml graphene flakes with the lateral size below 200 nm was developed and adopted for the aerosol-jet printing process to make a reliable and repeatable graphene deposition on the treated Si/SiO_2 wafers. To this end, the influence of the most significant process parameters, including the atomizer power, the atomizer flow rate, and the number of the printed layers, on the size and properties of graphene patterns was studied. Results showed that the aerosol-jet printing process is capable of printing micro-scale graphene pattern with variable widths in the range of 10 to 90 micron. These patterns, as the finest printed graphene patterns, with resistivity as low as 0.018 Ω.cm and a sheet resistance of 1.64 kΩ/□ may ease the development of miniaturized printed electronic applications of graphene.

In this work, a laser processing protocol for the heat treatment of the printed graphene patterns was also developed, and the results were compared with the counterpart results obtained by the conventional heat treatment process carried out in a furnace. A continuous-wave Erbium fiber laser was used to enhance electrical properties of the aerosol-jet printed graphene patterns through removing solvents and a stabilizer polymer. The laser power and the process speed were optimized to effectively treat the printed patterns without compromising the quality of the graphene flakes. Furthermore, a heat transfer model was developed, and its results were utilized to optimize the laser treatment process. It was found that the laser heat treatment process with a laser speed of 0.03 mm/s, a laser beam diameter ~50 µm, and a laser power of 10 W results in pure graphene patterns with no excessive components. The results suggested that the laser processing has the capability of removing stabilizer polymers and solvents through a localized moving heat source, which is preferable for flexible electronics with low working temperature substrates.

This dissertation also addresses the deployment of a graphene/silver nanoparticle (Ag NP) ink in an aerosol-jet additive manufacturing system in order to print highly conductive and flexible graphene/Ag patterns for flexible printed electronics. A graphene/Ag NP ink was developed using stabilized graphene powder, viscose Ag NP ink, and solvents compatible with

the printing system. Printing with this ink produced a uniform microstructure and crack-free printed interconnects. With a mean resistivity of 1.07×10^{-4} Ω.cm, these interconnects are about 100 times more conductive than graphene and three times more conductive than Ag NP interconnects printed with the same printing system. With their high degree of conductivity and a level of flexibility identical to that of graphene printed patterns, concluded from bending test results, graphene/Ag aerosol-jet printed patterns may therefore be considered as an efficient candidate compared to either graphene or Ag NP printed patterns for flexible electronics.

Acknowledgements

I would like to take this opportunity to first and foremost thank God for being my strength and guide in the writing of this thesis. Without Him, I would not have had the wisdom or the physical ability to do so.

I express my sincere gratitude to my supervisors, Dr. Ehsan Toyserkani, who has patiently guided and endlessly assisted me throughout my time as his student. I will forever be indebted by their guidance.

I hereby acknowledge my thesis examining committee members, Dr. Glenn Hibbard from University of Toronto, Dr. Shahrzad Esmaeili, Dr. Soo Jeon, and Dr. Mike Pope from University of Waterloo for taking the time to review my thesis and provide valuable feedback.

I would also like to acknowledge Natural Sciences and Engineering Research Council of Canada (NSERC; Discovery Grants of my supervisors), University of Waterloo and the Department of Mechanical and Mechatronics Engineering for financial support of the project.

I would like to extend special thanks to technical staff at University of Waterloo, especially Mark Griffett and Richard Barber, for assisting me to perform my experiments in their labs and with their equipment.

I would like to thank my colleagues at the Multi-scale Additive Manufacturing Laboratory research team at University of Waterloo, Dr. Mihaela Vlasea, Dr. Ehsan Foroozmehr, Dr. Hamidreza Alemohammad, Dr. Ahmad Basalah, Dr. Negar Rasti, Evan Wheat, Amir Azhari, Esmat Sheydaeian, Bahare Marzbanrad, Farzad Liravi, Yuze Huang, Richard Liang, Farid Behzadian, and Xixi Zhang for their friendship and assistance. I wish you guys all the best in all aspects of your life.

My work would not have been made possible without Dr. Pu Chen, Dr. Michael Mayer, Dr. Siva Sivoththaman, Dr. Aiping Yu, Dr. Ting Tsui, Dr. Fathy Hassan, Brandon Seo, and Navid Mohammad Sadegi Jahed from university of waterloo, Dr. Mark C. Hersam, and Ethan B.Secor from Northwestern University.

My heartfelt thanks go to my beloved family. Mom, I am here today because of you. Dad, you were with me when I started this job. You instilled my passion for engineering. You encouraged me to immigrate to a better place to be a better person. I wish you were here now. Thanks to my sisters, Tannaz and Elham, and my brother, Ali for their kindnesses, supports and encouragements.

Finally, to my caring, loving, and supportive husband, Arash: my deepest gratitude. You knew it would be a long and sometimes bumpy road, but encouraged and supported me along the way. Your endless patience and encouragement when the times got rough are much appreciated and duly noted. Thanks for your greatest gift, our beautiful daughter, Rose, who is happiness and joy of my life. It was a great comfort and relief to know that you were willing to take care of Rose and provide management of our household activities while I was completing my work. Thank you for everything.

Dedication

To

My father Davood

With whom this thesis would have been written with more courage and proud,

&

My mother Azam & my husband Arash

Without whom this thesis might not have been written,

&

My daughter Rose

Without whom this thesis would have been written one year earlier, but with less joy, motivation, and success.

Table of Content

List of Figures

List of Tables

Chapter 1. Introduction

1.1 Motivations

Graphene, as a 2-dimensional crystalline allotrope of carbon with extraordinary electrical and structural properties, has attracted many researchers and industrial sectors to adopt it as an alternative to traditional metallic elements for printed electronics, interconnects, and semiconductor applications. Better manufacturability and higher reproducibility of graphene have also made it a prominent competitor over carbon nanotubes (CNTs) in electronic applications. Favorable features of graphene, e.g., transparency and stretchability, also make graphene interconnects applicable in light emitting diodes (LEDs) for applications such as information displays and biomedical systems [2].

A preliminary experimental and theoretical study on printing silver nanoparticle (Ag NP) interconnects on flexible substrates, presented in Chapter 3, reveals a high chance of crack formation in the printed silver nanoparticles. Flexibility and crack formation issues in Ag NP interconnect created a keen interest to replace Ag NPs with an electrically conductive material that has better mechanical properties. Graphene, once printed, can be deformed without negatively affecting its performance due to its flexibility [3]. Thus, in this study, graphene has been considered as an ideal candidate for flexible electronics due to its high flexibility.

To create graphene patterns effectively, several techniques such as Mussel-inspired directed block copolymer [4], catalyst scanning probe lithography [5], and electron-induced self-assembly [6] have been successfully employed. Among all manufacturing techniques, additive manufacturing (AM) is considered as a more efficient process to fabricate microscale products because of its design freedom, high flexibility, reduced number of steps required for manufacturing, less generation of chemical waste, all while usually having a low cost [1, 7]. The integration of nanomaterials, such as silver nanoparticles, CNTs, and graphene, increases the strength of the layer-by-layer structure of AM products due to unique electrical and structural properties of such materials that can consequently expand the number of applications of AM made products [1].

Incorporation of the printed graphene into a variety of applications, such as supercapacitors [8], displays [9], sensors [10, 11], transparent conductors [12], and organic light-emitting diodes (OLEDs) [9, 13], has fostered the graphene printing research.

Inkjet printing is one of the most favorable fabrication processes for printed electronics due to its compatibility with a wide range of low viscous inks, its lower material waste, and its capacity for digital and additive patterning. However, the single large drop deposition and the drop randomized direction have hindered the deposition of tracks with a width less than 60 microns [14, 15].

In this study, for the first time, we have deployed an aerosol-jet printing system to fabricate microscale graphene patterns through multiple layers deposition (Chapter 4). In contrary to the ink-jet printing process, small droplet size (1-5 micron) in the aerosol-jet printing process results in a narrow aerosol stream. A focusing gas flow surrounds the atomized aerosol stream to confine the droplets in a uniform cylindrical shape resulting in printed patterns as small as 10 μm. [16-18]. The aerosol-jet process is also capable of printing inks with a wide range of viscosity (1 to 1000 cP) on non-planar and conformal substrates [18, 19]. The graphene printing with high viscosity inks is challenging by the ink-jet printing process due to the inherent features of fluid flows in the printheads that should carry with a minimum amount of friction and surface tensions. However, in the aerosol-jet printing process, an atomization technique is employed to form an aerosol stream. In the atomization step, high-frequency pressure waves are originated using an ultrasonic actuator and carried through a coupling fluid (commonly distilled water) to the ink inside a vial. In the print head, a sheath gas is also added to the stream to focus it into the narrow beam and help the beam to exit the print head without clogging. All these characteristics of aerosol-jet printing process facilitate the atomization and injection of the high viscosity inks [18]. Thus, aerosol-jet printing system is preferable to print high viscosity graphene ink that includes stabilizers to achieve a highly concentrated stable graphene ink.

In addition, the capillary wave hypothesis in the aerosol atomization process [20, 21] and its effect on crumpling of graphene sheets [22, 23] open a venue in this study to achieve wrinkled graphene sheets in the deposited tracks. As reported by other researchers [24, 25], even a low degree of crumpling in graphene sheets alters the properties of graphene. Due to the high resistivity of wrinkled graphene sheets to re-aggregation, they are more desirable than flat graphene sheets in electronic and energy storage devices [22-27]. Thus, the aerosol atomization can improve performance of graphene-based printed patterns.

However, printing graphene encounters many challenges. The first challenge is making graphene ink with high concentration to attain desired properties from the tracks created by the less number of the printed layers. All commercial graphene inks have very low concentrations around 0.001 mg/ml and cannot form a continuous pattern with connected graphene flakes. So, the first step is to make high concentration graphene inks. To date, some of the most applicable developed approaches for the production of graphene are chemical vapor deposition growth (CVD) [28], liquid-phase chemical exfoliation of graphite [29], and liquid-phase exfoliation of reduced graphene oxide (rGO) [30]. The outcome of the low-cost liquid-phase exfoliation technique is favorable for the printing methods. Despite many attempts for the inkjet printing of liquid-phase exfoliated rGO [12, 31], the inkjet printing of pristine graphene is more on demand due to defective structure of rGO yielding lower electronic transportation compared to pristine graphene [14]. In the present work, chemical exfoliation of graphite flakes, using long-term sonication, is employed to make a high concentrated graphene ink. Ethyl cellulose (EC) is used as a stabilizer polymer to prevent agglomeration of the graphene flakes in high concentration. To make the stabilized final ink, graphene powder is extracted from dispersion and redispersed in the needed solvent as explained in details in Chapter 4 [14].

In all ink-based additive manufacturing processes of graphene patterns such as ink-jet and aerosol-jet printing processes, the utilized inks, and consequently the printed patterns, include solvents and stabilizers in addition to the graphene flakes. The extra ingredients in the ink are required to prevent agglomeration of the flakes [14, 15, 32]. To optimize the properties of the printed patterns, all of the solvents and the polymer should be completely removed or partially decomposed. Thus, it is imperative to develop an effective post heat treatment process to decompose undesired elements after printing. To date, different heat treatment processes such as annealing in a vacuum oven [33], a tube furnace [14], and a regular hot plate [15, 32] are employed for printed graphene patterns. One of the main applications of the printed graphene is the development of conductive patterns on flexible substrates. Although some of the flexible substrates are functional at temperatures close to the required temperature for heat treatment of printed graphene patterns (e.g., 250 °C) [15, 34], low temperature or localized heat treatment processes are preferable for those substrates with low melting temperature for preventing any major warping [35]. The utilized aerosol-jet technology in this research, which is called laser-assisted maskless microdeposition (LAMM) technique, is integrated in-house with a CW fiber laser. This laser system was used as a post heat treatment source to remove solvents and the stabilizer polymer from the aerosol-jet additive manufactured graphene patterns (Chapter 5).

Despite the potential benefits of printed graphene, some challenges limit the electrical conductivity of printed graphene patterns and prevent the printed pattern from reflecting the unique electrical properties of the graphene. The most important factor is the necessity of keeping the lateral sizes of the graphene flakes in the inks small so that they can be printed and to prevent clogging of the nozzles. This requirement results in an increased number of flake edges and random joints in the printed patterns, which are consequently characterized by increased resistivity. Printing flexible graphene patterns whose electrical conductivity is comparable to that of metallic interconnects, therefore, seems to remain a challenge and opens an avenue for the printing of a combination of graphene and conventional conductive metals that can offer the advantages of both materials. Investigation of this possibility, however, has been limited. Thus far, only a few studies have been conducted with a view to either increasing conductivity or reducing costs by decreasing the concentration of silver nanoparticles (Ag NPs) through the addition of materials such as carbon nanotubes [36-39] and graphene sheets [39-41]. In the present study, we have developed an ink consisting of graphene as the flexible counterpart and Ag NPs as the conductive counterparts and have employed an aerosol-jet printing system for printing combined graphene/Ag NP conductive patterns (Chapter 6). Figure 1.1 shows the correlation of the different chapters of the present dissertation.

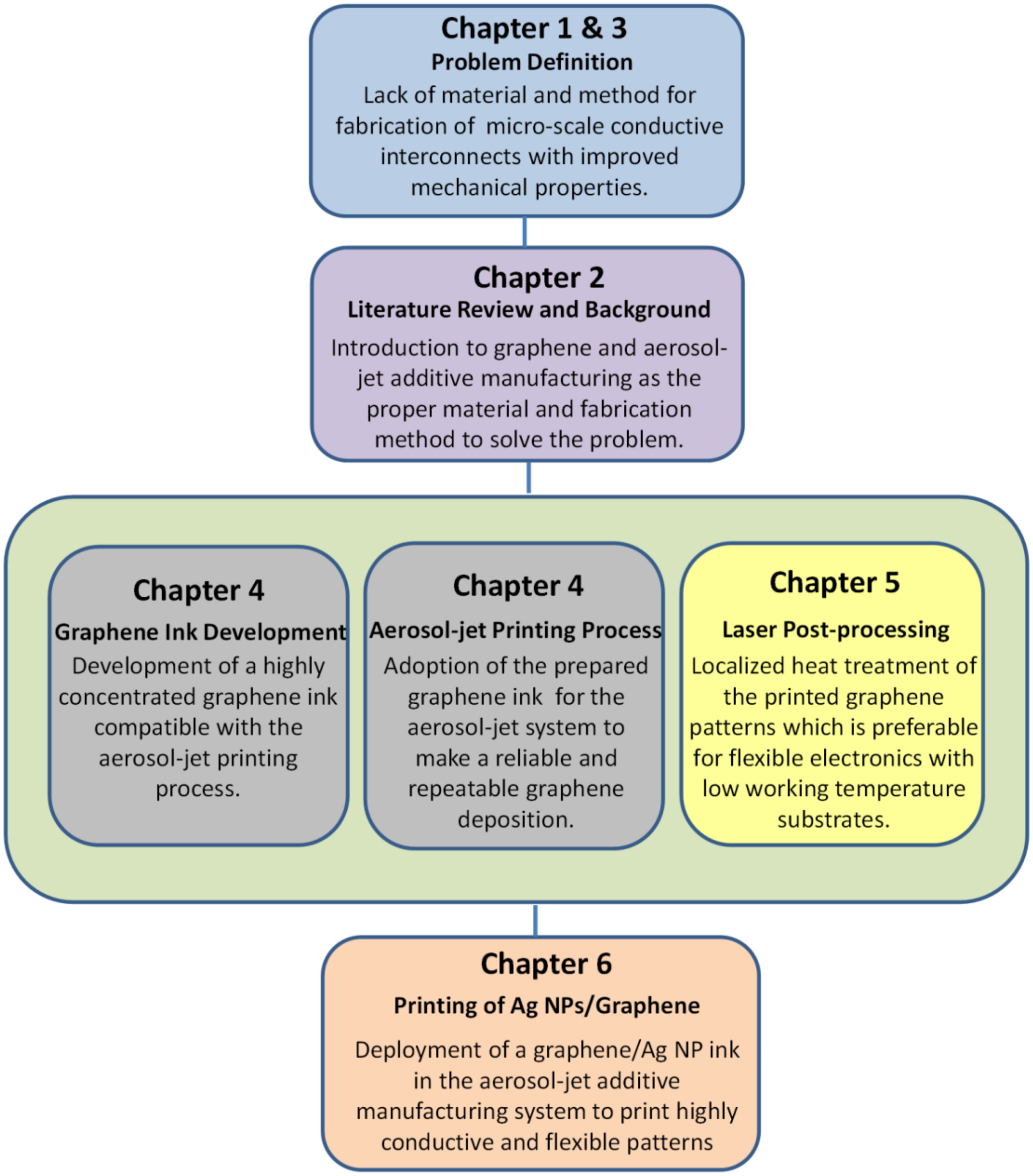

Figure 1.1. Motivation of the studies conducted in different chapters of the present dissertation.

1.2 Thesis Objectives

The objective of this thesis is the development of "*additive manufacturing of graphene-based patterns*". To this end, the following tasks were pursued:

- **Development of a high-concentration graphene-based ink** that is compatible with the aerosol-jet printing system,

- **Optimization of the aerosol-jet printing parameters** required for printing of the graphene ink and realization of graphene interconnects,
- **Development of a laser post-processing protocol** for graphene printed patterns as an localized heat treatment processes preferable for the flexible substrates with low working temperature,
- **Development of a Graphene/Silver Nanoparticle ink and its printing protocol** in the context of fabricating highly flexible and conductive graphene/silver nanoparticle printed interconnects in flexible electronics.

1.3 Thesis Outline

This thesis includes seven chapters. Chapter 1 outlines the motivation and ultimate objectives of the present research. Following introduction in this chapter, the outline of the thesis is described. Chapter 2 provides background information and literature reviews on the topics related to the current research. Chapter 3 describes our preliminary study on 3D finite element modeling and experimental analysis of printing non-planar silver nanoparticle interconnects in double-sided flexible Cu-PET substrates using the LAMM process. The results of this study motivated subsequent works on replacing silver nanoparticles with materials with more advanced properties. Chapter 4 addresses the development of a highly-concentrated graphene ink and the deployment of the aerosol-jet additive manufacturing technology to print graphene interconnects. Chapter 5 theoretically and experimentally addresses the development of a laser processing protocol for heat treatment of micro-scale printed graphene patterns. Chapter 6 presents the deployment of a developed graphene/silver nanoparticle ink in the aerosol-jet additive manufacturing system in order to print highly conductive and flexible graphene/Ag NP patterns. In Chapter 6, conclusions and recommendations for the future studies are outlined. Each of the chapters 3 to 6 represents one of my published studies as follows:

- The third chapter is a journal article published in the Journal of Optics and Lasers in Engineering:
    - ❖ **Jabari, E., Tong, S., Azhari, A., & Toyserkani, E. “Non-planar interconnects in double-sided flexible Cu-PET substrates using a laser-assisted maskless**

microdeposition process: 3D finite element modeling and experimental analysis". Journal of Optics and Lasers in Engineering. Accepted May, 2014.

- The fourth chapter is from a journal article published in Carbon journal and a provisional US patent:
    - ❖ **Jabari, E., Toyserkani, E. "Micro-scale Aerosol-jet Printing of Graphene Interconnects". Carbon Journal. Accepted May, 2015.**
    - ❖ **Toyserkani, E., Jabari, E., "Graphene printing: material, device and method", submitted May, 2015, US Provisional patent, Serial #62/179,412.**
- The fifth chapter is a journal article published in the Journal of Physics D: Applied Physics:
    - ❖ **Jabari, E., Toyserkani, E. "Laser Heat Treatment of the Printed Graphene Interconnects". Journal of Physics D: Applied Physics. Accepted August, 2015.**
- The sixth chapter consists of a manuscript submitted to the Journal of Materials Letters in November 14, 2015:
    - ❖ **Jabari, E., and Toyserkani, E., "Aerosol-Jet Printing of Highly Flexible and Conductive Graphene/Silver Patterns" Journal of Materials Letters, Submitted in November, 2015.**

Chapter 2. Background and literature review

In this chapter, a literature review on graphene, its properties, preparation methods and characterization tools, is presented. Furthermore, the importance of graphene as a promising material to interconnect are discussed and reviewed. Micro-scale AM techniques including aerosol-jet printing system are also introduced in this chapter.

2.1 Graphene

Carbon, due to having the ability to form a variety of atomic structures, attracted interest of researchers in different fields of study. This ability arises from the electron configuration of carbon, which can form different kinds of valence bonds to other carbon atoms. Graphene, as a carbon allotrope, comprises a quasi-two-dimensional isolated monolayer of carbon atoms arranged in a hexagonal (honeycomb) lattice [42]. It can also be imagined as an unrolled carbon nanotube (CNT). In Figure 2.1, the atomic structure of some carbon allotropes is shown.

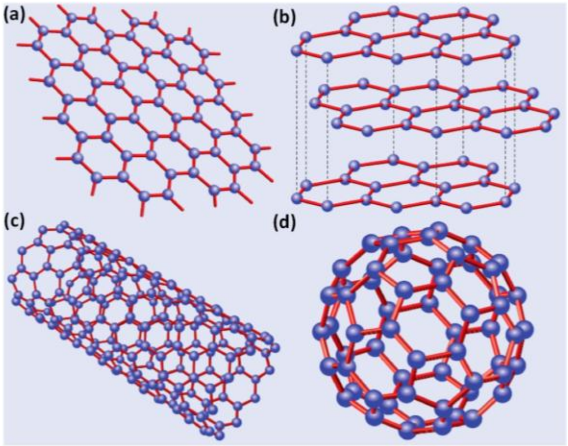

Figure 2.1. a) Graphene (a honeycomb lattice of carbon atoms). b) Graphite (a stack of graphene layers). c) Carbon nanotube (a rolled-up cylinder of graphene). d) Fullerene (a molecule consisting of wrapped graphene) [Courtesy of APS publications with permission] [43].

Although the structure of graphite has been known for a while, an individual isolated graphene layer was experimentally achieved for the first time in 2004 by Novoselov using a simple mechanical process. Graphene with a monolayer of carbon atoms, which is known as single-layer graphene (SLG), has different properties from bilayer graphene (BLG) and few-layer graphene (FLG, 3 to 10 layers). These different properties can be considered as the result of strong dependency of graphene properties to the number of graphene layers [44]. Since a structure with more than 10 stacked graphene layers has the electronic properties more like those of graphite, it is considered as a thin film of graphite. The arrangement of the stacked graphene layers is also known as a parameter which can drastically affect properties of graphene [45]. Three different stacking ways of graphene layers, i.e., simple hexagonal (AAA…), Bernal stacking (ABAB…) and rhombohedral (ABC…) exist [46]. While AA stacking is widely observed in SLG and BLG, AB- Bernal stacking occurs in FLG and graphite, and ABC stacking can be seen in chemical vapor deposition grown FLG [47].

2.1.1 Properties of Graphene

2.1.1.1 Electronic Properties of Graphene

Graphene has received enormous attention since its discovery, mostly because of its exceptional electronic properties for electronic applications. So it is worthwhile to discuss more in depth about band structure of graphene.

The 2D structure, the honeycomb lattice, and identical atoms in all the lattice sites confer unique electronic properties. In graphene structure, a strong in-plane covalent bond, so-called σ bond, connects one carbon atom to its three nearest neighbors. This bond involves three of four valence electrons of the carbon atom. The length of σ bonds (unit cell of the graphene lattice) and the angle between them are 1.42 Å and 120°, respectively. These bonds hold graphene in plane and form its 2D structure. Therefore, they have important implications for mechanical and thermal properties of graphene [48].

The second type of bond in graphene structure is known as valence bonds (occupied π bonds) or conduction bonds (unoccupied π^* bonds). The fourth valence electron of carbon atoms remains in the $2p_z$orbital perpendicular to the σ bond. These π bonds, shown in Figure 2.2, result from overlapping of half-filled $2p_z$ orbital of adjacent atoms by Van der Waals forces. These bonds are responsible for most of the transport properties of graphene.

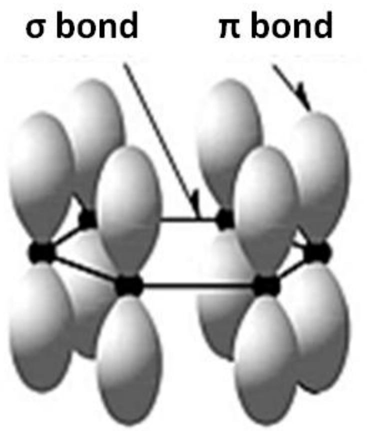

Figure 2.2. Schematic of in-plane σ bonds and perpendicular π bonds [Courtesy of Taylor & Francis publications with permission] [49].

Due to zero density of state (DOS) (like semiconductors) without any energy gap of valence and conduction bands (like metals), graphene is known as a zero-gap semiconductor [49]. Although graphene has high charge carrier density, its zero-energy band gap restricts its utilization in logic electronic application. In order to overcome this drawback in graphene-based field effect transistors, a band-gap is needed to be opened by forming graphene nanoribbons or graphene quantum dots [50].

The electronic properties of graphene depend on the number of layers, the way in which layers stacked on top of each other, structural defects, and supported substrate.

2.1.1.2 Chemical Properties of Graphene

The incorporation of graphene into various applications has increased interest in chemical properties of graphene. Compatibility and durability of graphene in various environments, exposed to a different range of materials, exemplify its unique chemical properties.

As explained in the previous section, graphene has two different kinds of bonds in its structure. The strong covalent σ bonds hold graphene in plane and make it relatively chemically inert. It has been proved that graphene can work as a chemically inert diffusion barrier for refined metals exposed to air at temperatures up to 200˚C for some hours or in contact with hydrogen peroxide [51]. Due to the flat lattice of graphene, covalent functionalization of graphene is more difficult than that of carbon nanotubes (CNTs) [52]. Many other different factors in graphene structure can strongly affect its covalent chemical functionalization. It highly depends upon the size of the graphene sheet, which defines the number of the atoms at the edge of graphene [53]. It can also be easily affected by the corrugation of the graphene sheet, the number of defects in the lattice [54, 55], and on a larger scale by the number of layers in the graphene structure [56]. It has to be noted that, although inactive graphene is desired in many applications, sometimes promoting chemical reactivity of pristine graphene has to be considered as a chemical modification for specific purposes. Chemical functionalization is done by oxidization [57], hydrogenation [52], laser excitation [56], and many other methods.

On the other hand, the existence of Van der Waals π bonds between individual layers of graphene results in high noncovalent reactivity of graphene with small molecules containing aromatic rings. These weak attachments of atoms or molecules to graphene occur in air, moisture or hydrocarbon contaminated atmosphere and lead to doping of graphene.

2.1.1.3 Mechanical Properties of Graphene

Since graphene, like carbon nanotube, has the strongest C-C chemical bond among other carbon allotropes, exceptional mechanical properties for graphene are expected. These kinds of bonds make the intrinsic strength of Graphene higher than of any other material [58]. Experimental and theoretical studies have confirmed non-linear elastic properties of graphene without chirality effects with a Poisson's ratio (ν_b) equal to 0.21 [59, 60].

Although simulations depict a strong dependence of mechanical properties, e.g., young's modulus, fracture strength, and fracture strain on temperature, experimental investigations into such dependency are still lacking due to challenges in the handling of graphene specimens [60]. Mechanical properties of graphene, like any other materials, are also defined by the density of defects, e.g. vacancies, grain boundaries, and substitutional impurities [61].

2.1.1.4 Thermal Properties of Graphene

The strong in-plane bonding in graphene results in the highest in-plane thermal conductivity (~2000- 4000 W/mK) compared to other carbon allotropes and any known material. Although diamond has as high thermal conductivity as graphene, the 2D structure of graphene provides more manageable heat transfer in various directions.

By contrast, its thermal conductivity out of plane is relatively low (100 times lower than its in-plane thermal conductivity) due to weak Van der Waals bonds. So graphene has been considered as an anisotropic thermal conductor [62]. Theoretical results suggest that graphene is a material with adjustable thermal conductivity, applicable in a huge range of applications from heat-sinking devices to thermoelectric devices.

The thermal properties of pristine graphene can be altered by various factors such as properties of the supporting substrate, strain [63], grain boundaries [64], chemical reaction, vacancies, and all other defects, which modify the structure significantly from that of pristine graphene.

2.1.2 Methods of Making Graphene

Based on material nature, 1- or 2-dimensional structures cannot be obtained by crystal growth. So the growth of a single layer of graphene, as a material with a 2D structure that is completely isolated from its environment, has not been observed. However graphene can be produced artificially. Some low-cost and easily performed methods based on the exfoliation of graphite to separate graphene layers have been developed so far [65, 66].

2.1.2.1 Mechanical Exfoliation

Mechanical exfoliation of graphene includes splitting layered graphite into graphene layers using mechanical forces. This approach is implemented in some techniques such as those based on adhesive tape and atomic force microscopy (AFM) tip. A graphene film was produced using Scotch-tape in Geim and Novoselove’s group for the first time in 2004 [67].

All attempts before their work led to a small graphite island with different properties from a single layer of graphene. They used an adhesive tape to peel off some layers of highly oriented pyrolytic graphite (HOPG). Despite the high-quality graphene sheet achieved by this easy and quick method, it cannot yield enough graphene for many applications [67].

Another technique based on atomic force microscopy (AFM) tip manipulation of graphite flakes employed for the first time by Lu et al. [68]. This method includes making some islands of HOPG with diminished height and carefully exfoliating graphene sheets by the AFM tip. Compared to other mechanical exfoliation techniques of graphene, this method is more complicated and more time consuming. Also by this way, graphene with the desired number of layers cannot be obtained.

All mechanical methods, already discussed or not, provide insufficient output for many applications. Also, the applied forces by these methods may cause various defects, e.g., wrinkles, corrugation, and atomic defects and consequently may reduce electrical conductivity in graphene [69]. These drawbacks prevent commercialization of mechanical exfoliation methods.

2.1.2.2 Chemical Exfoliation

Separating graphene layers from graphite bulk in a solvent using the energy of a sonicator is known as chemical exfoliation. Niyogi calculated the amount of energy required to be around 2 eV/nm^2 [70]. Different types of graphite, solvents, and sonication systems can be used to direct chemical exfoliation. All mentioned factors can alter the process time, output yield, number of layers, and properties of the resulting graphene.

In order to select the right source of graphite, impurities and the degree of crystallinity should be considered as the main factors. Graphite with high crystallinity, such as HOPG, is much harder to exfoliate than that with stacking faults, such as natural flakes.

The boiling point and surface energy of the solvent are dominant factors in selecting a solvent to achieve a given graphene output.

Furthermore, the sonicator, as the source of energy to separate graphene layers, plays an important role in achieving fast and efficient exfoliation. Since tip sonicators can transfer more power than bath sonicators, they can shorten the process.

2.1.2.3 Reduction of Graphene Oxide

Graphene oxide is obtained by separating single sheets from graphite oxide by sonication or stirring. The structure of oxidized graphene is completely different from that of pristine graphene. All methods of making graphite oxide that have been known since the 19th century, including Brodie (1860), Staudenmaier (1898), and Hummers (1958), are based on exposing graphite to a strong aqueous oxidizing agent [71].

To form individual graphene sheets, graphite oxide must be dispersed in water and separated by an input power. Although graphite oxide can be dispersed in different kinds of organic solvents [72], most research uses aqueous dispersions. Due to the hydrophilic nature of graphene oxide sheets, water can easily affect their arrangement and facilitate the exfoliation process [73].

Next, in order to convert graphene oxide to graphene, methods of chemical reduction, heat treatment, or electrochemical reduction are employed. Various approaches to chemical reduction have been used, e.g., adding a stabilizing polymer as a reducing agent in aqueous solution [74], and using hydrazine to reduce and disperse graphene oxide in aqueous solution [75]. Also, due to thermal expansion mechanisms of graphite oxide, a series of heat treatments at temperatures higher than 550˚C can exfoliate graphene layers and keep them separated [76]. Reduction of graphene oxide yields a highly defective graphene of lower quality than chemically or mechanically exfoliated graphene. So reduced graphene oxide is limited to applications that are not sensitive to the lattice quality, such as lightweight ultrastrong composites.

2.1.3 Characterization of Graphene Methods

2.1.3.1 Optical Microscopy

Optical microscopy is one of the most useful tools to investigate the presence of graphene and to efficiently inspect the number of graphene layers. Based on some researches, a single-layer graphene sheet is invisible on most substrates. On the other hand, some researchers have claimed that even single-layer graphene sheet can be observed by the means of straightforward optical tools [77]. The substrate also plays an important role and can easily affect the speed of the inspection. A silicon wafer with a specific thickness of silicon dioxide is usually used as the substrate on which graphene sheets of different thicknesses can be most easily found. Figure 2.3 shows optical images of different sheets of graphene on Si/SiO$_2$ substrate. Differences in the reflection from the graphene sheets and SiO$_2$ surface make the sheets visible; the reflected color varies based on the number of graphene layers [78].

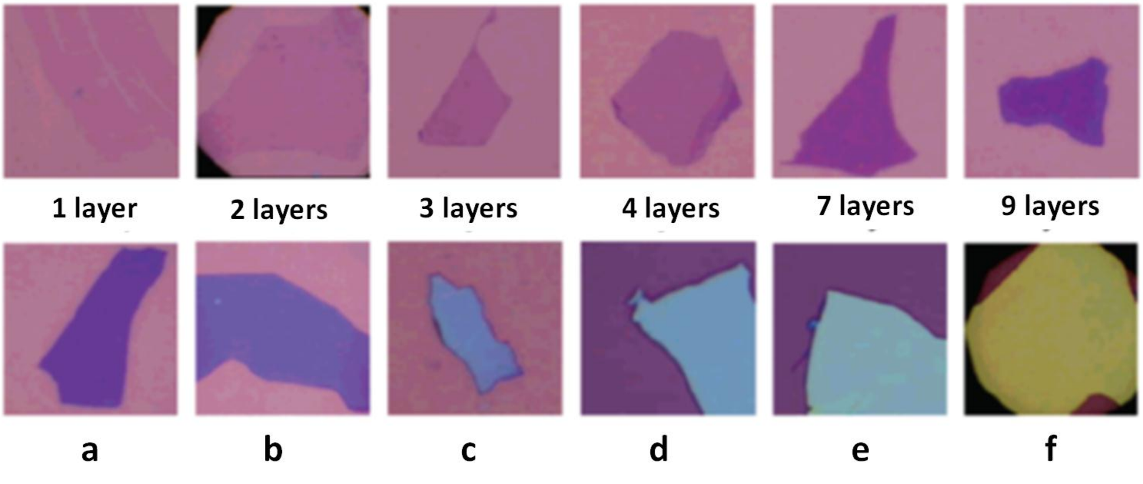

Figure 2.3. Optical images (below images) of graphene sheets with different numbers of the layers. Samples a to f have more than 10 layers and the thickness increase from a to f [Courtesy of ACS publications with permission] [78].

2.1.3.2 Raman Spectroscopy

Raman spectroscopy, as a quick, efficient, and non-destructive characterization tool, can yield high-resolution and precise information about graphene structure, the number of layers, and the amount of lattice defects. Raman technique has been used to study graphite structure for 40 years [79]. However, it was employed to characterize graphene for the first time in 2006 [80]. The main identification features of carbon allotropes in Raman spectrum are G band and 2D band which appear around 1580 and 2700 cm^{-1} respectively. However, intensity, position, and even the shape of the G and 2D bands dramatically change when the number of the layers increases. Figure 2.4 compares the Raman spectra of graphite and graphene with different numbers of layers.

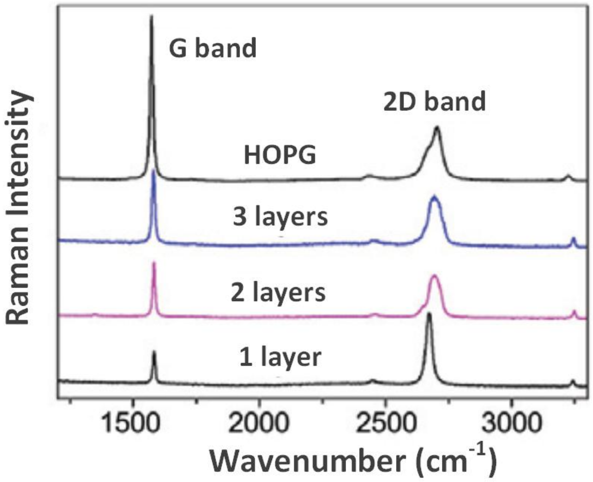

Figure 2.4. Raman spectra of HOPG and graphene with 1, 2, and 3 layers [Courtesy of Springer publications with permission] [81].

As it can be seen in Figure 2.4, by increasing the layers, G band and 2D band are subjected to red-shifting and blue-shifting, respectively. The peaks also have different shape and intensity for graphite. Spectra of graphene with more than five layers are hard to distinguish from spectra of graphite [82].

Also, there might be another peak around 1380 cm^{-1}, the so-called D band, in the Raman spectra of graphene whose intensity depends on the quantity of active defects in graphene lattice. It has to be noted that the D band depends on the number of active defects in undoped samples. Thus, silent defects such as charged impurities, perfect zigzag edges, uniaxial and biaxial strain do not result in a rising D peak. These kinds of defects are reflected in either 2D or G bands in Raman spectra [82].

2.1.3.3 Scanning Electron Microscopy

Scanning electron microscopy (SEM) is one of the most practical ways to estimate nucleation density of graphene [83], investigate its growth mechanism [84], and determine its grain size [85], morphology, and substrate coverage [83]. It is mostly used for chemical vapor deposited (CVD) graphene.

SEM can also provide chemical analysis using an energy-dispersive X-ray analysis (EDX) detector, which can be added to the microscope system. Therefore, SEM is a useful tool to verify the morphology of graphene for the desired grain size, coverage, and shape.

2.1.3.4 Transmission Electron Microscopy

Transmission electron microscopy (TEM) and scanning transmission electron microscopy (STEM) are usually employed to study the number of graphene layers and to characterize structural defects such as vacancies, grain boundaries, and dislocations. Folding of the graphene film edge produces the cross-sectional view in observation to count the number of the layers [86]. S(TEM) techniques can also be used to define extrinsic defects [87], study the edge structure of graphene [88], and observe the behavior of graphene under manipulation [89].

2.1.3.5 Atomic Force Microscopy

Atomic force microscopy (AFM) is a useful tool not only for determining graphene topology, its corrugation properties, and its number of layers, but also for examining mechanical properties of graphene, including Young’s modulus, intrinsic strength, and spring constant. It is used to see different graphene topology on different substrates [90]. AFM is also used to compare topology of graphene oxide and reduced graphene oxide [91]. By tapping mode AFM, new procedures for cleaning contaminated graphene used in different devices [92] and manipulation of single or few-layer graphene sheets [93] have been developed.

2.2 Graphene-based Interconnects

Graphene, owing to high electrical and thermal conductivity, electron mobility, mechanical strength, intrinsic flexibility, and chemical stability, is an attractive substitute to traditional metal interconnects, especially in the nano-scale. Graphene interconnects can be applied in printed electronics and semiconductors. In the nanoscale, graphene interconnects are more efficient than metal interconnects, such as copper wires, with the same dimensions. The smaller grain size of copper leads to a rising number of grain boundaries in small interconnects. So the electrons have to pass through grain boundaries more frequently and are consequently subjected to more scattering [94].

Among all carbon-based interconnects, considerable attention is focused on carbon nanotube (CNT) and graphene nanoribbon (GNR) interconnects. Although GNRs have the same electron transport properties as CNTs, GNRs advantageous to use over CNTs mainly because of easier manufacturing and material control (due to their 2D structure), and higher reproducibility [95]. In Table 2.1, the main properties of some of the most conventional interconnect materials are compared [96].

Table 2.1. Properties of Cu, SWCNT, and Graphene/GNR related to interconnect applications (adopted from [96] with permission).

		Cu	SWCNT	Graphene
Max current density (A/cm^2)		10^7	$>10^9$	$>10^8$
Melting point (K)		1356	3773(graphite)	3773(graphite)
Tensile strength (GPa)		0.22	22.2±2.2	-
Thermal conductivity ($\times 10^3$ W/mK)		0.385	1.75-5.8	3-5
Mean free path (nm) @ room temperature		40	$> 10^3$	1×10^3
Status of fabrication techniques	Films / Horizontal wires	Mature	not known	known but immature
	Vertical vias	mature	nascent stage	not known

Theoretical models have predicted that the resistivity of a GNR with smooth edges and width below 8 nm can be smaller than that of similar copper wires [97]. Other theoretical models and calculations have also shown smaller signal delays in high-quality doped GNRs compared to 11-nm copper wires [96]. Trilayer graphene (TGN) is one of the other graphene-based materials which has recently been considered as a semimetal for interconnects due to its reliability and controllability compared to bilayer graphene (BGN) [98, 99]. The flexibility of printed graphene interconnects is one of its other advantages. Graphene, once printed, can be deformed without negatively affecting its performance [3]. Favorable features of graphene, e.g., transparency and stretchability, make graphene interconnects applicable in next-generation flexible semiconductors and as a more functional replacement for conventional transparent conducting oxides (TCOs) [2].

2.3 Microscale Additive Manufacturing

Nowadays, a wide range of microfabrication technologies has been employed for microproducts with various properties and applications. Of all manufacturing techniques, AM is considered as a more efficient process to fabricate 3D microscale products [7]. The AM term, recently used instead of Rapid Prototyping (RP) and 3D printing by adopted ASTM consensus standards [100], is to describe some evolving technologies that fabricate objects from the bottom by adding layer by layer material. Some advantages of AM over conventional fabrication technologies are higher manufacturing speed, design freedom, reduced number of process, cleaner technology regarding chemical usage and waste, and lower cost [1]. Additive manufacturing was first widely used for fabrication of polymeric objects. With recent advances in AM techniques, metals, composites, and ceramics are also being employed.

The laminar structure of objects fabricated by AM resulted in poor strength of components, which is considered as a limitation of AM in manufacturing. Since material properties differ drastically from the macro to the nano scale, combining nanotechnology with AM can overcome some of these limitations. Nanomaterials such as metal nanoparticles, carbon nanotubes, nanowires, and graphene possess unique electrical and structural properties. So, in this Ph.D. project, silver nanoparticles and graphene are utilized in microscale laser-assisted AM of interconnects by taking advantage of materials and process. Figure 2.5 indicates one of the most accepted classifications of different technologies in 3D micro AM.

Inkjet printing, as an AM process placed in the first group of above classification, is one of the most favorable fabrication processes for printed electronics due to its compatibility with a wide range of substrates, its lower material waste, and its capacity for digital and additive patterning [14]. However, the technologies in this first group encounter some difficulties in micro-size fabrication. The second class of above classification is efficiently capable of fabricating micro-size structures [7]. Aerosol-jet printing systems are of new ink-based AM processes in second class with high ability to print small patterns on almost all kinds of substrates. In this system, the injection process that is completely different from inkjet yields deposition of patterns in the size range of 10 micrometers to centimeter scale.

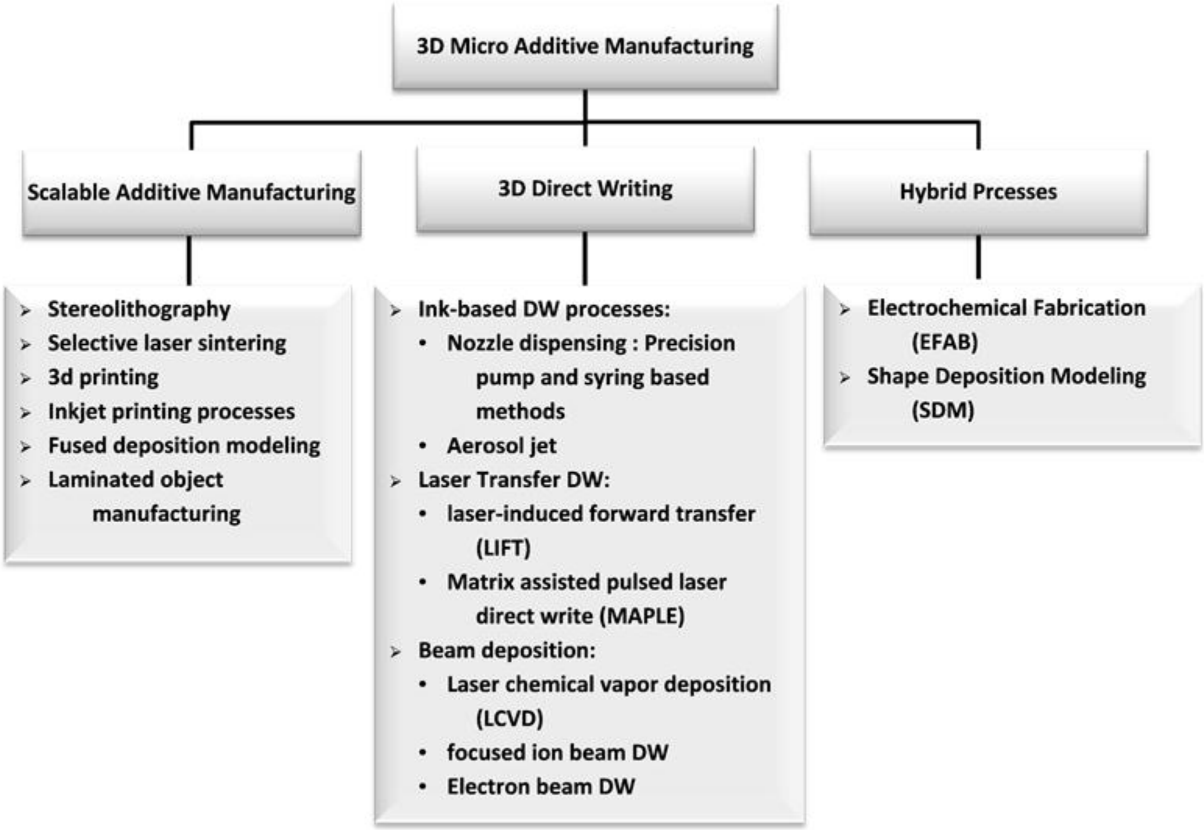

Figure 2.5. Classification of 3D microscale additive manufacturing technologies (adopted from [7] with permission).

The micro AM technique of aerosol-jet direct writing, employed in this research, is explained in the following.

2.3.1 Aerosol-jet Additive Manufacturing Technology

With recent improvements in microelectronics technology, 3D interconnects are gaining mainstream primacy in the electronics packaging industry. There are a few commercialized techniques for making 3D interconnects, such as stacked die packaging and through silicon VIAS (TSVs). Such technology allows electronic component wiring to extend beyond the 2D plane by creating interconnects in the z-axis relative to the circuit board [101]. In addition, aerosol-jet direct write printing has been used in this market but has not been commercialized yet

[102]. Several types of materials, including polymers, ceramics, and “nano-inks” made of suspensions of pure metals and alloys, can be used to create such 3D interconnects, though with different means. The aerosol-jet direct write allows for the manufacturing of conformal/3D interconnects through the injection of conductive nanoparticles on non-planar surfaces at low temperatures without imposing any pressure on the surface [102]. Aerosol-jet technology is a form of direct writing for a very rapid and flexible manufacturing process without expensive tooling, dies, or photo-lithography [103]. This method of manufacturing generally uses a moveable positioning stage and a pattern-generating device such as a deposition nozzle [104].

Ink jet systems suffer from some limitations including clogging nozzle, low density (8 to 12 cP) inks, single large drop deposition, and random directionality. Despite the ink jet systems, aerosol jet printers have clog resistant nozzle, a continuous stream of high-density microdroplets, the ability to deposition a wide range of viscosity of inks (1 to 1000 cP), and a tightly focused deposition patterns. Small droplet size (1-5 micron) in the aerosol-jet printing process results in a narrow aerosol stream. A focusing gas flow surrounds the atomized aerosol stream to confine the droplets in a uniform cylindrical shape resulting in printed patterns as small as 10 µm [16-18]. In aerosol-jet system, stand-off distance between the tip of the printing nozzle and substrate is variable and can be as high as 5 mm. These enable the aerosol-jet system to print 3D and conformal features [105]. Some advantages of aerosol-jet printing to use over ink-jet printing are illustrated in Figure 2.6.

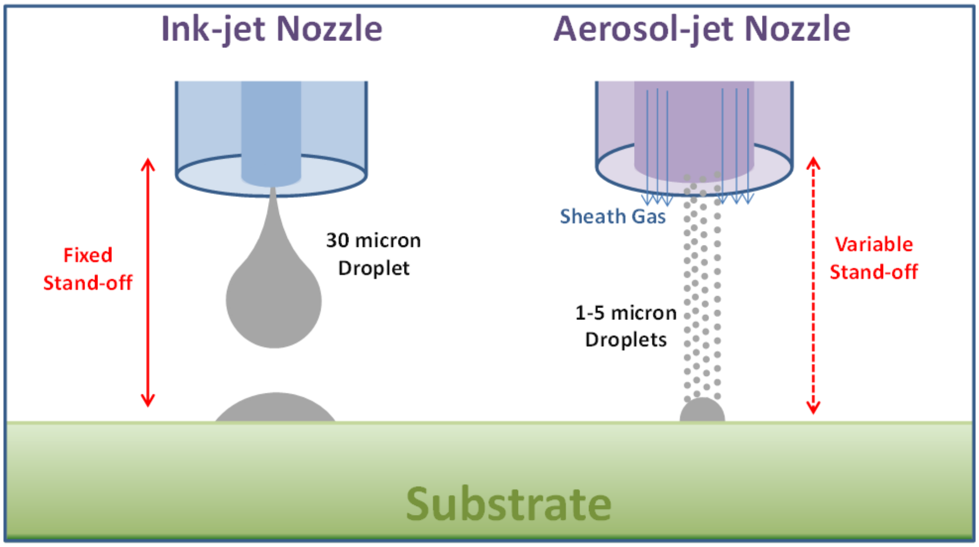

Figure 2.6. Material deposition by ink-jet and Aerosol-jet printing.

The aerosol-jet micro-scale printing system consists of three major parts: an ultrasonic actuator, a deposition nozzle, and a moveable stage to place substrate. First, the ultrasonic atomizer creates a mist of atomized droplets by the atomization of the particles on the surface of the ink. The mist is then introduced into a gas flow and carried through a tube to be delivered to the deposition nozzle. In the deposition nozzle, another gas flow is also entrained into the atomized mist to direct the particles to depart from the nozzle and print a small pattern on the substrate [19]. These steps are schematically shown in Figure 2.7.

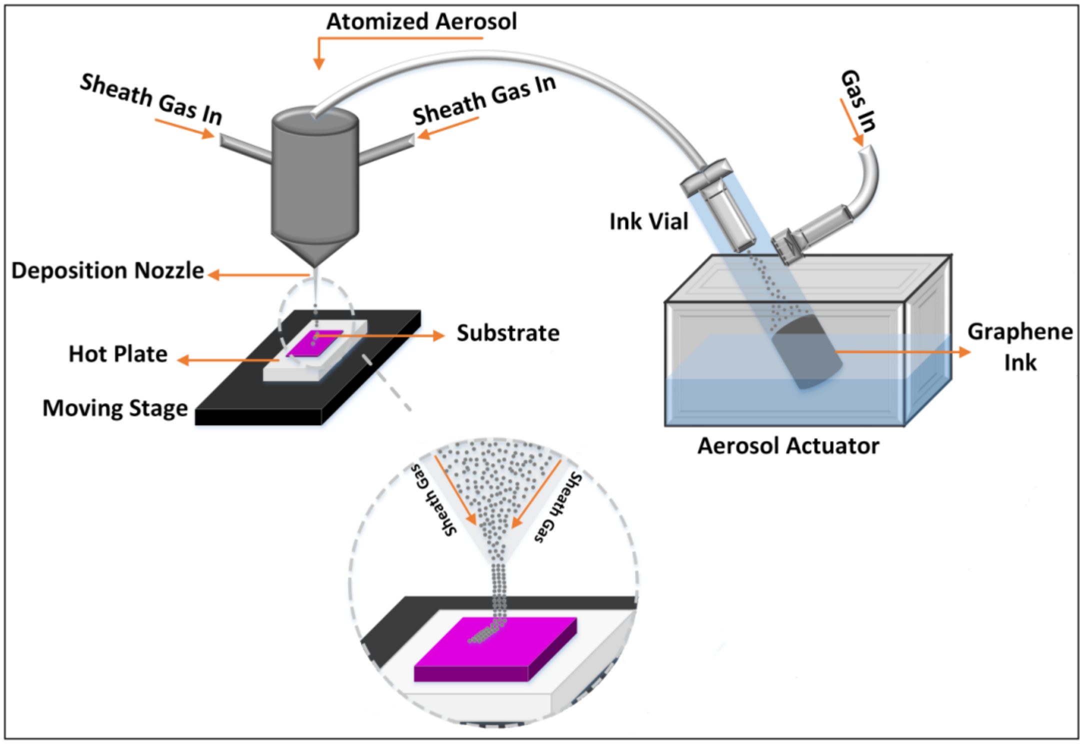

Figure 2.7. Aerosol-jet printing setup.

The size of particles suspended in the ink plays an important role in the printing process. Many important parameters, which are involved in the microdeposition process (e.g. atomizer power, atomizer gas and sheath gas flow rate, the viscosity of the nano-ink and the position of its vial in the ultrasonic actuator, the temperature of substrate, and the velocity of deposition) should be carefully determined to achieve a repeatable outcome.

2.3.2 Laser-Assisted Maskless Microdeposition System (LAMM)

In this PhD project, we used a laser assisted maskless microdeposition (LAMM) system, where aerosol-jet AM technology is integrated with an erbium laser system which is shown in

Figure 2.8. The laser is added to the aerosol-jet technology to do any needed heat treatment of the printed patterns right after printing through a moving heat source. It provides an opportunity to locally heat treat the printed patterns which is preferred for many of the substrates.

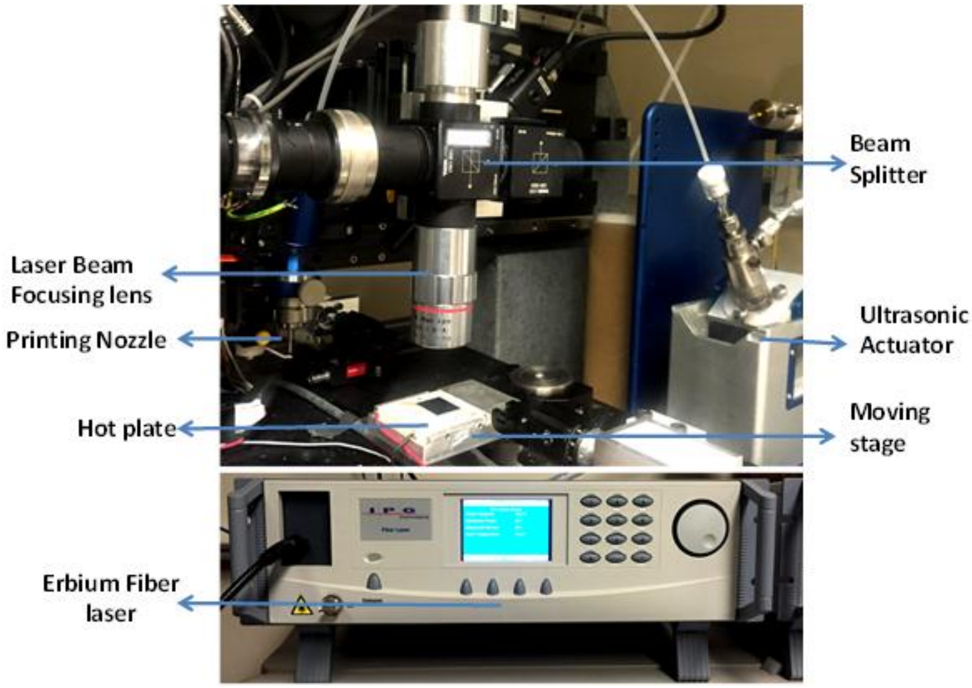

Figure 2.8. Erbium laser system.

The LAMM machine, shown in Figure 2.9, has four major components: an ultrasonic atomizer, a deposition unit, a laser with an optical head, and a positioning stage. LAMM is capable of depositing various materials, such as metals and polymers, and in complex patterns on various planar or non-planar substrates. Moreover, small droplet size (1-5 micron) enables LAMM to print small patterns (i.e., less than 20 µm in width and 25 nm to 1.5 µm in thickness) compared to other direct write methods. During deposition process and laser post processing, there is no physical contact between the pattern being printed and the tip of printing nozzle. It results in a clean and stable printing process. After the microdeposition process, laser post-processing is required to do any needed heat treatment. The resultant laser exposed materials have increased density and electrical conductivity [106].

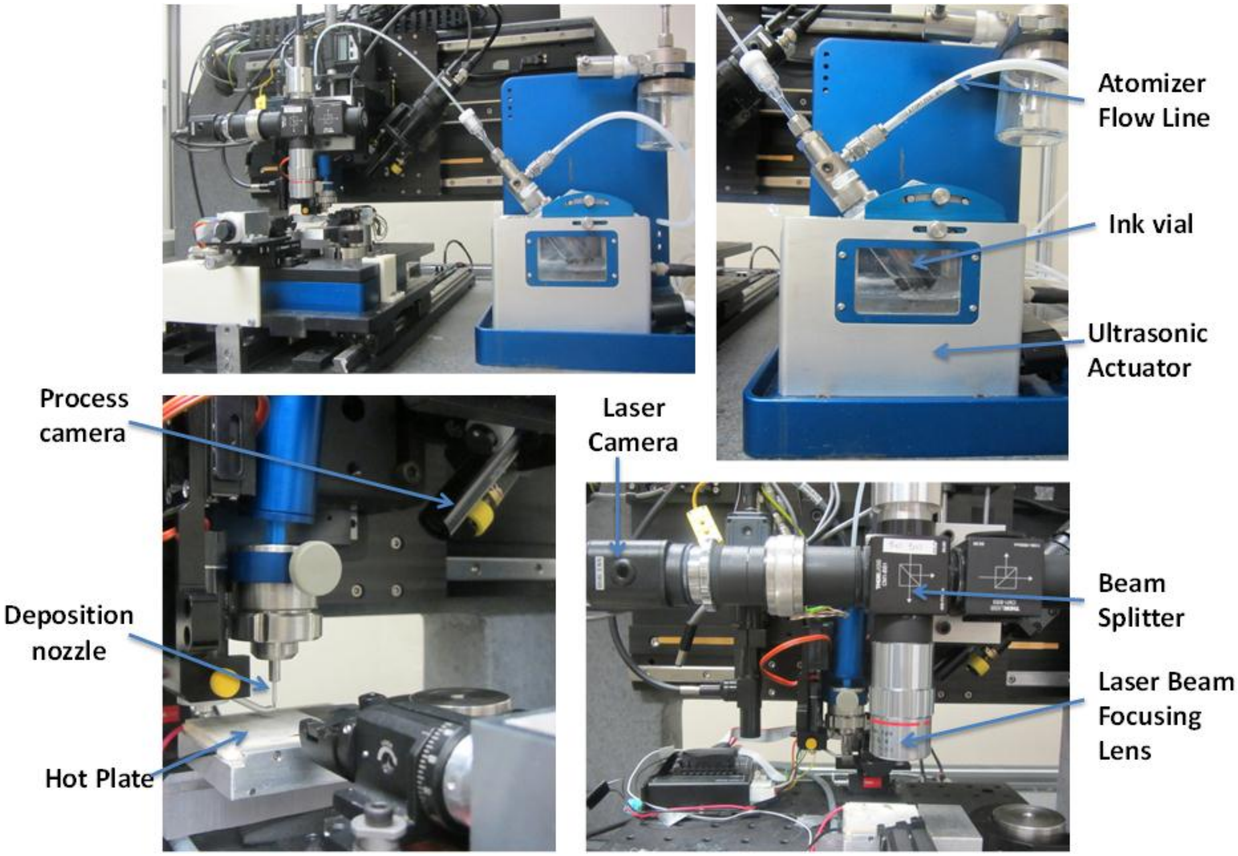

Figure 2.9. Various components of the LAMM system.

In order to achieve the desired quality of deposition (i.e., geometry and electrical conductivity), several important parameters should be carefully controlled. The most important parameters for the microdeposition process are the atomizer power, the viscosity of the nanoparticle suspension, the location of the nano-ink reservoir relative to the ultrasonic actuator, atomizer gas flow rate, deposition velocity, sheath gas flow rate, the number of layers, and substrate temperature. In the sintering step, important parameters are those that determine the heat flux delivered to the deposition: laser power, laser scanning speed, and laser beam spot size [21].

2.4 Summary

Literature suggests that graphene, owing to its high electrical conductivity, mechanical strength, and intrinsic flexibility, is an attractive substitute for traditional metal interconnects in flexible electronic applications. So incorporation of printed graphene features into a variety of electronic applications is a promising research direction. Additive manufacturing (AM) is also one of the most efficient fabrication techniques for micro-scale products. The integration of graphene as a nanomaterial with unique electrical and structural properties can improve the properties of the layer-by-layer structure of additively manufactured products and can be considered as an evolution in micro-scale manufacturing technologies. Reviewing literature indicates that the area of AM of graphene-based interconnects which is the main goal of this thesis is at an early stage of the development and needs to be expanded.

Chapter 3. Aerosol-jet Printing of Non-planar Silver Nanoparticle Interconnects in Double-Sided Flexible Substrates (Preliminary Study)*

Non-planar interconnects have an important role in the electronic packaging industry these days. These unconventional interconnects allow manufacturers to save materials and space while connecting circuit components on flexible and non-planar substrates. Among a variety of flexible boards, double-sided flexible substrates have attracted the electronic industry to effectively and compactly develop miniaturized flexible devices such as sensors-on-chips. This chapter reports our developmental procedure for the creation of non-planar silver interconnects on the edge of double-sided copper substrates separated by a layer of polyethylene terephthalate (PET) using LAMM. This study consists of the characterization of the LAMM process to effectively deposit Ag nanoparticles for the production of conductive interconnects. Several parameters, including the deposition and laser processing parameters, are optimized to achieve interconnects free of pores, cracks and delamination. Furthermore, a 3D finite element numerical model was developed to predict the laser processing of silver nanoparticles on the substrate. The model includes a coupled thermal and structural governing physics to derive the temperature history throughout the simulation as well as strain/displacement within the substrate, which is identified the major source of cark formation in Ag tracks.

---

* Jabari, E., Tong, S., Azhari, A., 2014, "Non-Planar Interconnects in Double-Sided Flexible Cu-PET Substrates using a Laser-Assisted Maskless Microdeposition Process: 3D Finite Element Modeling and Experimental Analysis," Optics and Lasers in Engineering, **54**pp. 117-127.

3.1 Experimental Procedure

3.1.1 Materials

Suspended silver nanoparticles (Cabot Superior Micro suspension, Albuquerque, NM, USA) were used in the experiments. This suspension was 45-55wt% of silver with an average particle size of 60 nm in ethylene glycol ($C_2H_4(OH)_2$) (and other compatible alcohols and diols). The edges of the substrates were polished at an angle of 45° with a polishing pad and very fine abrasive (Al oxide powder with grain size of 0.05 µm) such that when placed upon a flat surface, the sample had a slanted edge which exposed the lower layer of copper. Figure 3.1 shows a schematic side view of such a sample after polishing.

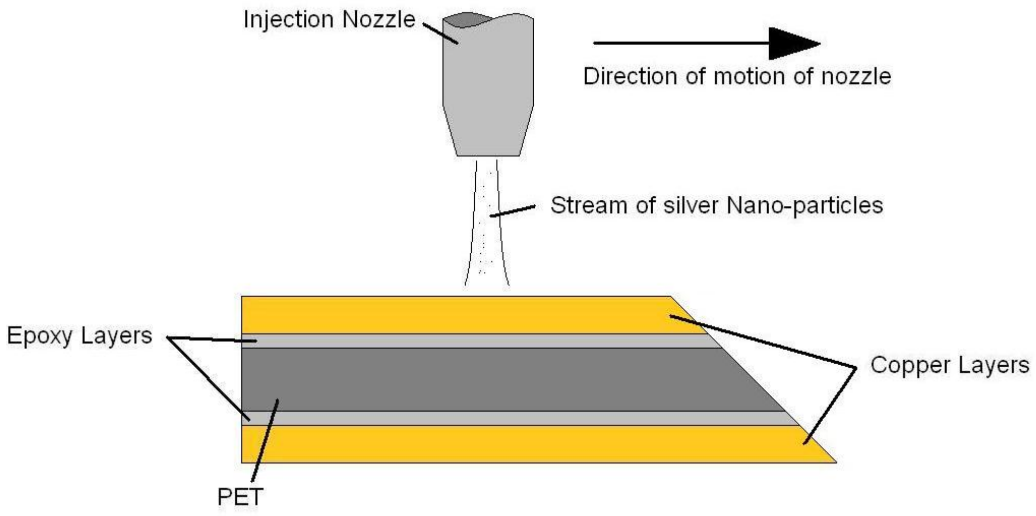

Figure 3.1. Side view of a substrate with a polished slant.

With the sample edge slanted as such, the silver nanoparticles can be deposited in a track along the face of the substrate such that the silver creates an electrical connection between the top and bottom layers of copper. In order to avoid the delamination of the silver tracks after deposition, cleaning was done before the deposition process. As-received Cu-PET flexible substrates were submerged in an isopropanol solution and sonicated by an ultrasonic cleaner. Once the samples were polished and cleaned, the deposition process was performed. For an optimized process, the viscosity of the nano-ink should be in a specific range (5 to 20 cP). To achieve this, the as-received nano-ink was diluted with distilled water at a volume ratio of 1:3 of undiluted suspension to water. With the LAMM system, silver nanoparticles were deposited upon the top layer of copper.

The LAMM process parameters in microdeposition step are listed in Table 3.1. For the deposition, the injection nozzle travels from the flat surface of the top layer of copper and deposit silver nanoparticles across the slanted surface that was created through polishing. The deposition process was then repeated to create a four-layer silver track for each sample to increase the track thickness to 5 to 8 µm.

Table 3.1. LAMM Process Parameters used in microdeposition step.

Sheath Gas flow rate (ccm)	Atomizer gas flow rate (ccm)	Ultrasonic Atomizer Power (V)	Deposition velocity (mm/s)
50	12	40	1

The deposition is followed by a laser sintering process. The LAMM process parameters in laser sintering step are listed in Table 3.2. The laser power was measured at the focused area using a power meter (L30A thermal head, OPHIR, North Logan, UT, USA). Since the laser is mounted upon the LAMM system, it is able to move on the same axis as the deposition head.

Table 3.2. LAMM Process Parameters used in laser-post processing step.

Working laser beam spot diameter at waist (µm)	Laser scanning speed (mm/s)	Laser power (W) measured at the process zone
100	1	0.44, 1.24 and 1.7

The nanoparticles are sintered using a continuous-wave (CW) single-mode Erbium fiber laser (ELR-20-1550, IPG Photonics Corporation, Oxford, MA, USA) with a wavelength of 1550 nm. The size of the laser beam at the focal point is 30 µm. For the purposes of these experiments, an offset was applied to the height of the laser such that the spot size was around 100 µm.

Noted that heating the substrate during deposition allows the silver particles to adhere better; thus forming a more uniform track. Therefore, the substrates were heated to 70˚C during deposition process using a thermoelectric heating plate.

3.1.2 Characterization Methods

After deposition and sintering, the samples were examined by optical imaging and scanning electron microscopes (SEM) to observe the quality as well as the microstructure of the deposited tracks. For performing optical imaging, a vision camera (EO-3112, Edmund Optics, Barrington, NJ, USA) was used in combination with a zoom imaging lens (Techspec® VZM 1000I, Barrington, New Jersey, USA) and a fiber optic illuminator (Dolan Jenner MI-150, Barrington, New Jersey, USA). Scanning electron microscopes (LEO 1530 FESEM, Zeiss, Oberkochen, Germany), (JSM7000F, JEOL Ltd, Tokyo, Japan) and (JSM-6460, JEOL Ltd, Tokyo, Japan) with energy-dispersive X-ray spectroscopy (EDS) were used. The samples were also analysed with X-ray Diffraction (Rigaku SA-HF3, Rigaku Corporation, Tokyo, Japan) in order to detect the crystalline structure. The samples were tested for conductivity using a digital multimeter (Omega® HHM32, Omega® Engineering Inc, Stamford, Connecticut, USA). Also, one of the conductive samples was tested using a source-measurement unit (Keithley 2612 SourceMeter, Keithley Instruments, Cleveland, Ohio, USA) to obtain a more accurate representation of the resistance as opposed to the ohmmeter.

3.2 Results and discussion

3.2.1 Experimental Analysis

The experiments were performed under different sintering process conditions. Different laser sintering conditions and the associated resistance are listed in Table 3.3.

Table 3.3. Laser post-sintering power and resistance outcomes.

Laser Power (W)	Resistance (Ω)
0.44 (Low power)	None conductive samples
1.24 (Medium power)	~ 3.2±1
1.7 (High power)	Burned samples

Among three different laser powers, which are so-called as low, medium and high power, only the medium laser power succeeded in creating conductive samples. It should be noted that some cracks are visible in all samples including conductive and nonconductive samples; however, the cracks in the medium laser power samples were not substantial. The low laser power led to nonconductive samples with the cracks and some delamination. In addition, when the laser power was increased to 1.7 W, it was observed that the PET layer burned for all samples during the sintering process. Figure 3.2 confirms the above observation where it depicts top views of substrates with polished slants when observing through an optical microscope after the experiments were performed. The substrates shown each contains a deposited silver track which has undergone sintering at specific laser powers.

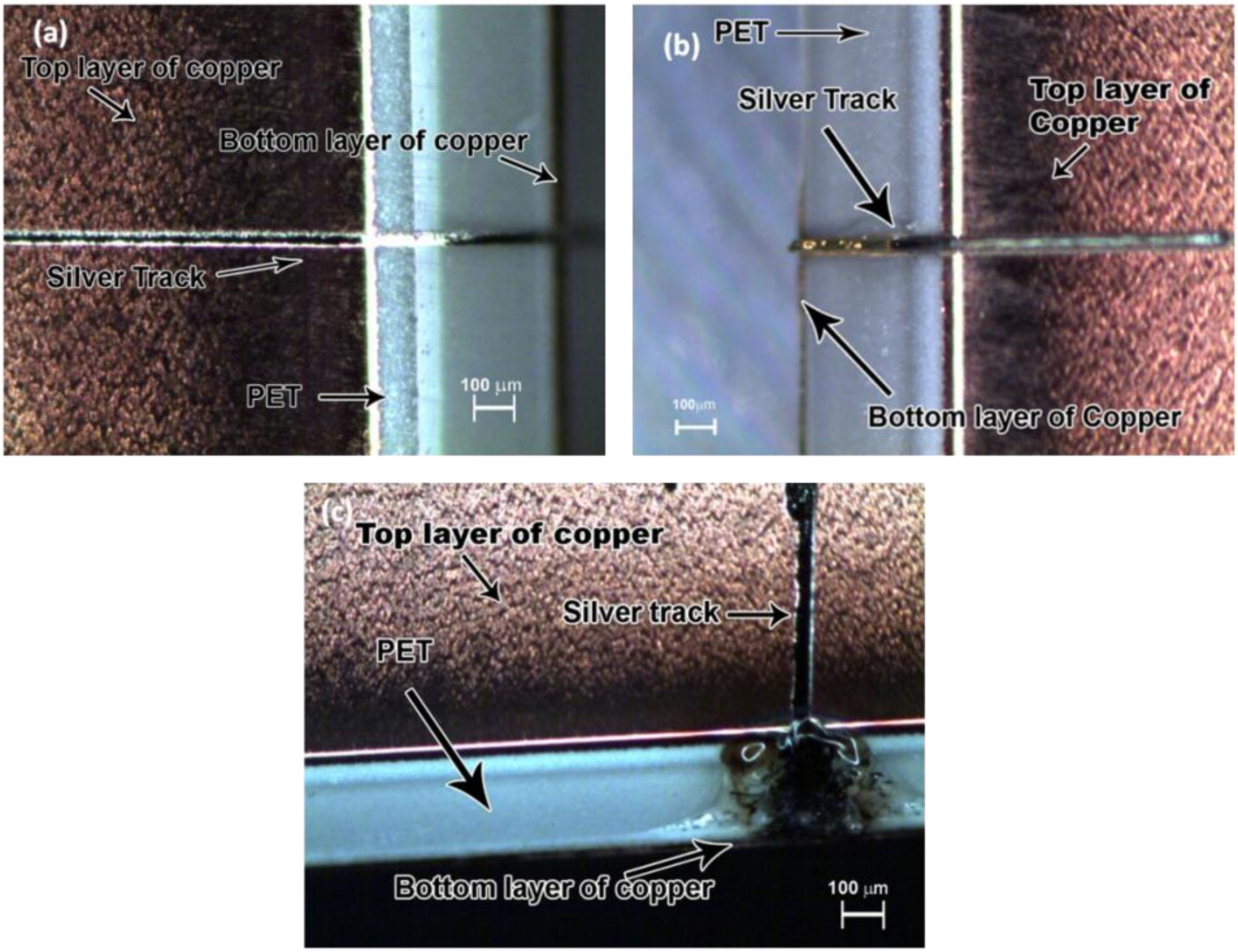

Figure 3.2. Top views of slanted edged substrates after depositing and laser sintering at (a) 0.44 W and (b) 1.24 W (c) 1.7 W at 1 mm/s speed.

To better observe the samples, an SEM analysis was performed on all processed samples. The SEM images are shown in Figure 3.3.

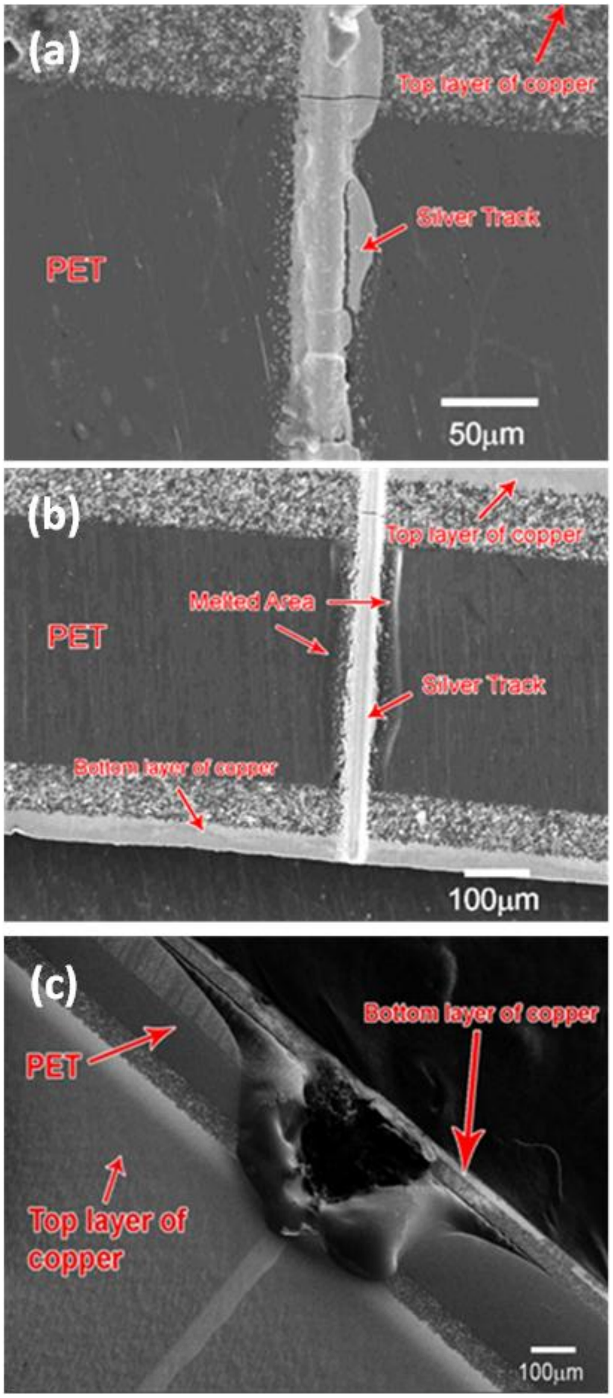

Figure 3.3. SEM Image of a sample treated at a) 0.44 W b) 1.24 W c) 1.7 W laser poser with 1 mm/s laser speed.

As seen in Figure 3.3.a and b, there are some cracks in the silver tracks. One source of these cracks can be resulted from different layers displacement due to different thermal expansion of Cu, Ag, and PET. To substantiate this claim, SEM micrographs of silver nanoparticles post-processed at low and medium laser power are shown in Figure 3.4.

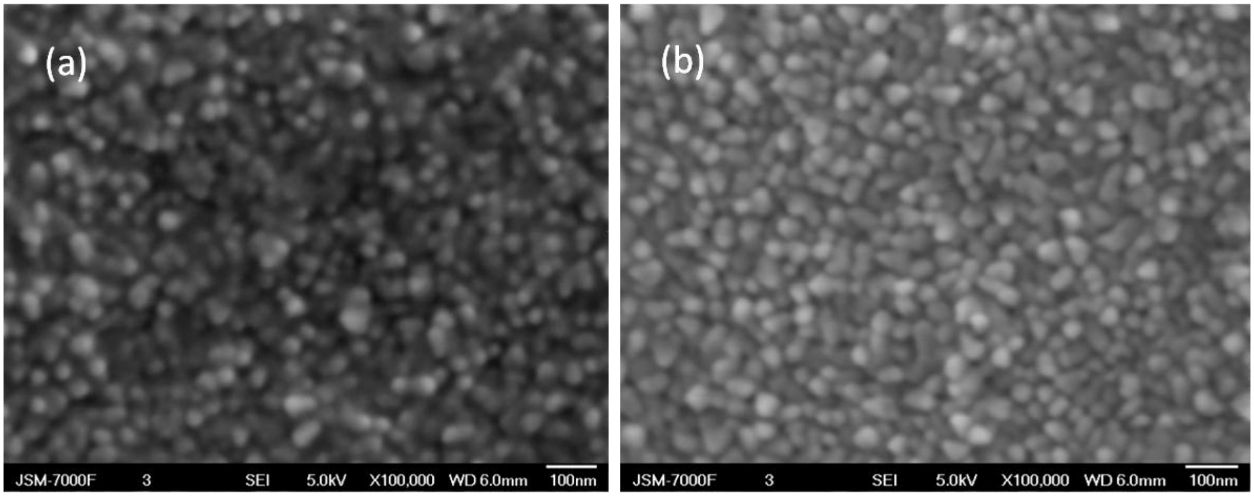

Figure 3.4. SEM images of silver nanoparticles after laser post-processing at (a) 0.44 W laser power with 1 mm/s laser speed resulted in non-conductive interconnects (b) 1.24 W laser power with 1 mm/s laser speed resulted in conductive interconnects.

Although, it is difficult to differentiate sinter necks in two images, we observed different brightness while comparing conductive samples with nonconductive ones. Considering different brightness of the SEM images, nanoparticles processed at low laser power appear to be darker compared to the counterpart samples sintered at higher laser power that yields to brighter images of agglomerated nanoparticles. This observation may imply that the higher conductivity (fully developed sinter neck) in the sample causes the brighter SEM images.

An energy-dispersive X-ray spectroscopy (EDS) analysis was performed to detect compositions and any possible contaminants. Contaminants on the surface of the copper may cause delamination of the silver particles on the copper face, compromising the conductivity. Figure 3.5 shows the locations where EDS results were produced. Table 6 lists the composition of materials at the selected locations.

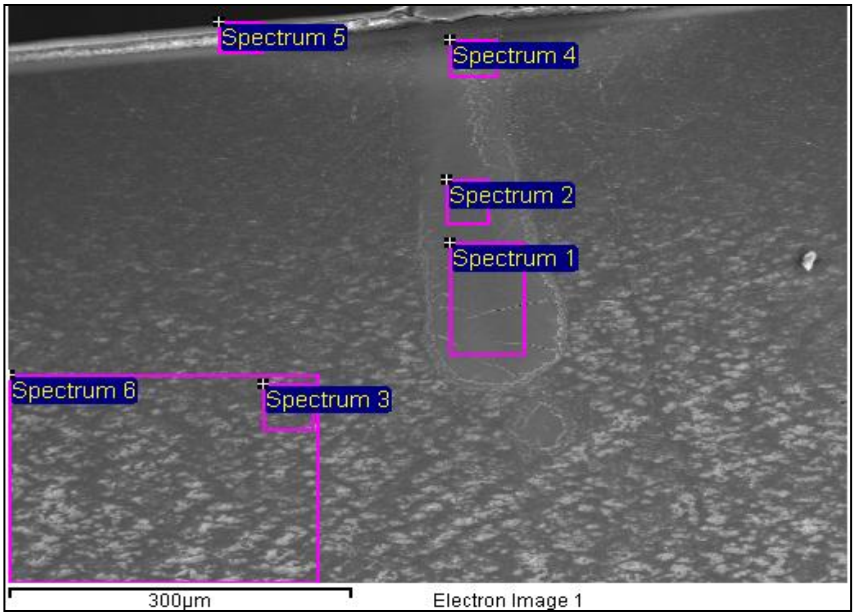

Figure 3.5. EDS image for a substrate sintered at 1.24 W with 1 mm/s laser speed.

Table 3.4. EDS results for locations shown in Figure 3.5.

Spectrum	**C**	**O**	**Al**	**Cu**	**Ag**
	(Wt%)	**(Wt%)**	**(Wt%)**	**(Wt%)**	**(Wt%)**
Spec 1					100
Spec 2					100
Spec 3				100	
Spec 4				8.78	91.2
Spec 5	58.7	13.9	3.7	23.8	
Spec 6				100	

The EDS results show that the surface of Cu does not appear to have any EDS detectable contaminants that may cause delamination. From Figure 3.5, spectrum 5 contains analysis on the edge of the substrate. Traces of aluminum were found in this area, which may also lead to cracks or delamination along the silver track that is on the edge of the substrate. The aluminum residue can be the result of the polishing with aluminum oxide powder.

The profile of the silver track on the top copper surface of a conductive sample with a slanted edge taken from the profilometer is shown in Figure 3.6 a. As seen, the profile of the silver track has a very uniform height. Another profile analysis was done on the slanted edge of the substrate as shown in Figure 3.6 b. The silver track can be seen as the red line that travels on top of the substrate. For this image, the substrate was tilted such that the slanted edge would appear in horizontal line. As seen, the surface of the edge is not as planar as expected. This may be attributed to the residual deformation after the laser processing process. Nevertheless, it shows that although the edge is not perfectly planar, it seems to have not much of an impact on the conductivity of the samples.

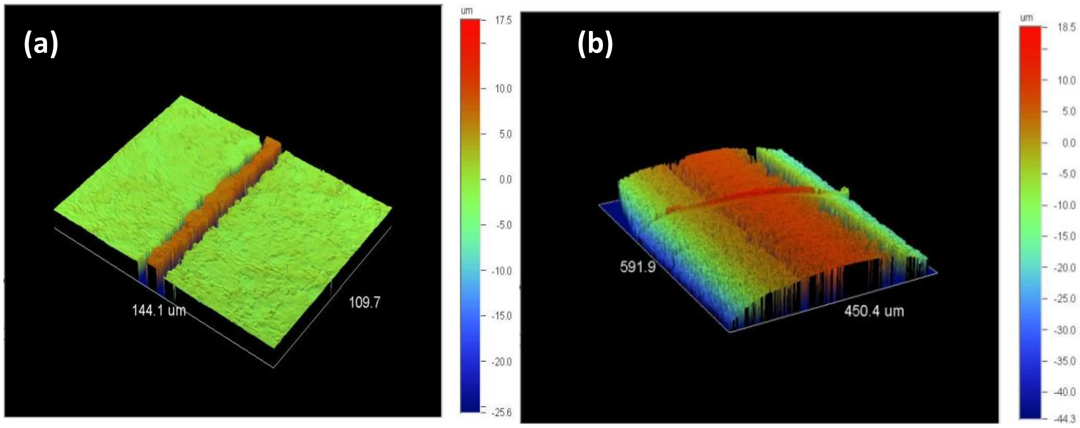

Figure 3.6. Profile of silver track on (a) a horizontal part of the top surface of copper (b) the slanted edge of the substrate.

To check the formation of any intermetallic phases XRD patterns for double sided copper samples with a track of Ag nanoparticles are shown in Figure 3.7.

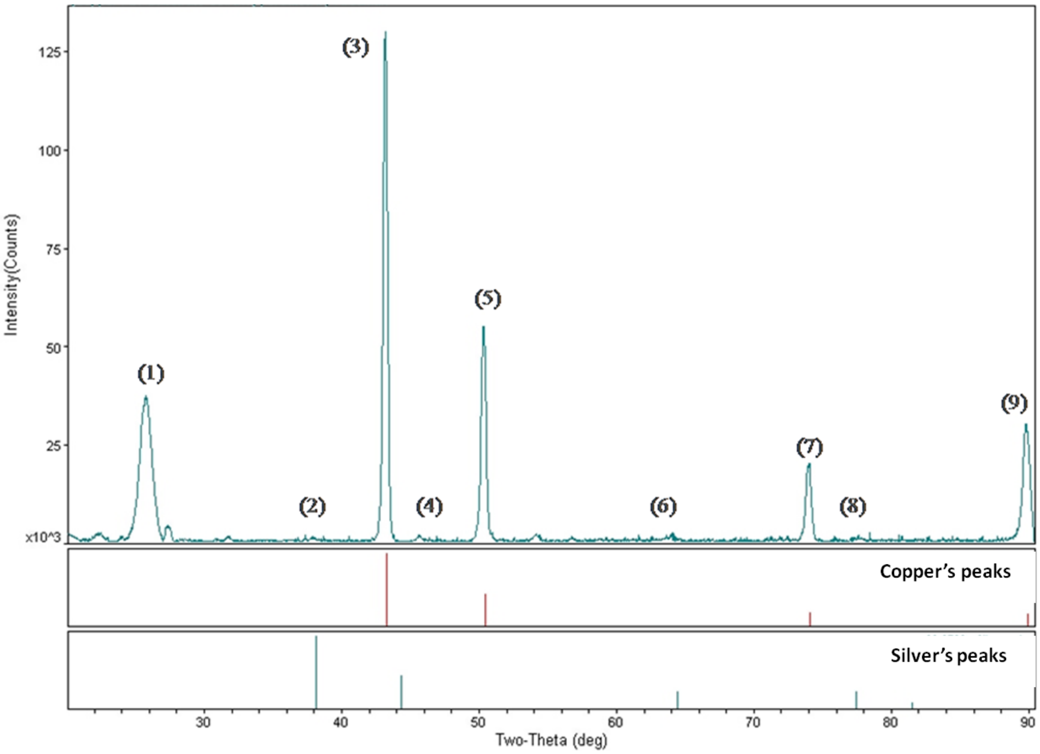

Figure 3.7. XRD result of a conductive sample.

As seen in Figure 3.7, peak (3), (5), (7) and (9) correspond to Cu and peak (2), (4), (6) and (8) are related to nano-Ag. Since a polycrystalline material without lattice strain with particle sizes larger than 500 nm causes sharp lines in an x-ray diffractogram [107], large crystallites of Cu exhibit sharp peaks, as expected. Furthermore, silver nanoparticles give peaks with very low intensity. It should be considered as a result of small crystallite size which causes wide picks with low intensity [107]. Based on Joan's work that is associated with PET's XRD curves at different particle sizes, the position of PET's peak is around 2θ = 20° [107], as a consequence, it is concluded that peak (1) is associated with PET in our sample. As expected from Ag-Cu phase diagram, no Ag-Cu intermetallic is observed after the sintering process. Also, diffractogram shows no other unexpected crystal such as oxides. Thus, we conclude that the only source of crack and delamination in this material system is residual stress/strain due to different thermal expansion of dissimilar materials in the system.

3.2.2 Three-dimensional Finite Element Modeling

A three-dimensional thermal model of the silver nanoparticles track on the Cu-PET substrate under a moving laser heat source is developed in COMSOL Multiphysics to simulate the effect of the laser sintering parameters on the temperature and strain-stress profiles. The model is developed based on a coupled thermal-structural multiphysics theory, in which the displacement of silver track during and after the laser sintering process at the interface of Cu-PET is analyzed. The domain includes a silver track of silver with thickness of 7 μm located on the surface and the slanted edge of a double-sided copper substrate with two layers of 60 μm thick Cu and a 200 μm thick PET layer in between as shown in Figure 3.8 (a). This geometry mimics the geometrical features of experimental samples.

3.2.2.1 Thermal model

The "general heat transfer with conduction" module is considered for solving a partial differential equation of heat transfer:

$$\rho C_p \frac{\partial T}{\partial t} - \nabla.(k\nabla T) = Q \qquad (3.1)$$

where Q, C_p, ρ, and k are power generation per unit volume of the substrate, specific heat capacity, density and thermal conductivity, respectively.

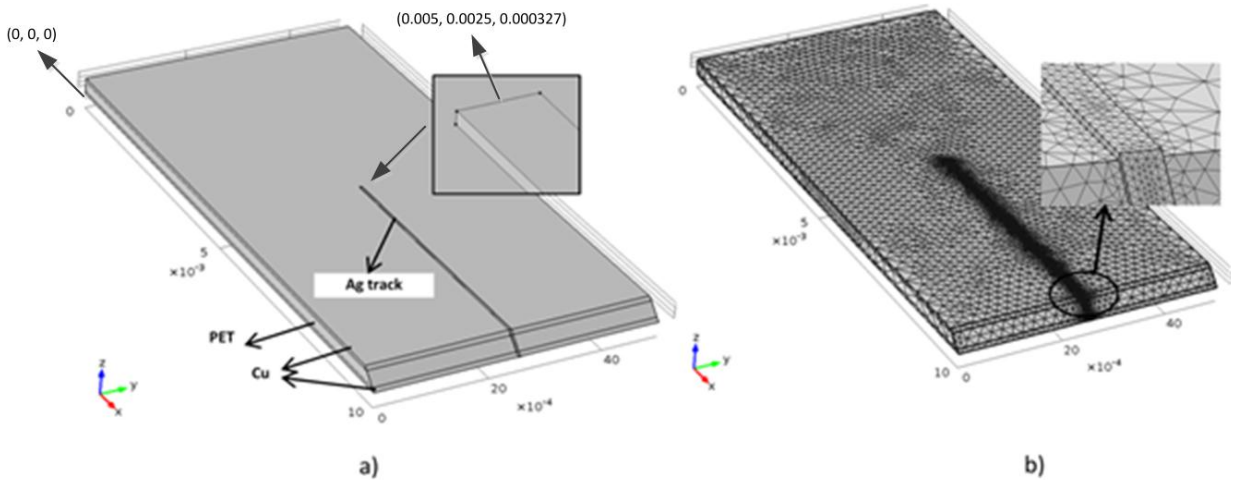

Figure 3.8. a) The geometry of the domain and materials arrangement (the scale of the coordinate is in meter); b) mesh plot of the model.

Boundary conditions for all peripheral surfaces of the domain should be defined in order to solve the heat transfer equation. The entire substrate is subject to convective heat transfer but its bottom side that has a constant temperature. In addition, a moving heat source boundary condition is set to the top surface (including silver nanoparticles track and Cu). Since we have assumed the radiation to be negligible, the heat flux boundary condition will be:

$$-k.\nabla \mathrm{T}.\,\mathrm{n}|_{\Omega} = \begin{cases} q_0 - h_c(T - T_0) & \text{if } \Omega \in [\text{laser beam location}] \\ -h_c(T - T_0) & \text{if } \Omega \in [\text{laser beam location}] \end{cases} \qquad (3.2)$$

where n is the normal vector of the boundary, q_0 is the heat flux per area, and h_c is the convective heat transfer coefficient of the surface of the Ω. Since the top surface is subject to a moving heat source as one of its boundary conditions, the heat source is then proposed as a heat flux as follows:

$$q_0 = \beta I \qquad (3.3)$$

where β is absorption factor and I is the laser energy distribution on the substrate. As the laser is Gaussian and continuous with a TEM_{00} mode, intensity of laser is given by:

$$I = I_0 \exp(-\frac{2r^2}{r_l^2}) \qquad (3.4)$$

where the variable r^2 for a laser source starting from $(x_{o,}\, y_o)$ with speed V_l in x-direction in Cartesian coordinates can be written as:

$$r^2 = (x - V_l t - x_o)^2 + (y - y_0)^2 + (z - z_0)^2 \qquad (3.5)$$

where x_o and y_0 define the position of the center line of the laser beam. Also r_l is beam radius at spot point which varies on the slanted surface based on the following equation that is a function of the laser wavelength (λ) and a distance z from the waist position of radius r_0:

$$r_l^2 = r_0^2\ [1 + \left(\frac{\lambda z}{\pi r_0^2}\right)^2] \qquad (3.6)$$

Also the constant I_0 is defined as:

$$I_0 = \frac{2P_l}{\pi r_l^2} \qquad (3.7)$$

where P_l is the laser power at the process zone.

3.2.2.2 Thermal-Structural Interaction Model

The laser beam irradiation over the silver nanoparticles track locally increases the particles temperature promoting the sintering initiation among nano-particles. In addition, coefficient of thermal expansion mismatches in the domain with multiple materials imposes varying strains (displacement) within the layers and subsequent crack formation. Given multiple materials in the domain and considering different thermal expansion properties, varying strains within the layers are presented that in turn result in crack formation which exists in most of the samples after laser post-processing. To estimate residual stresses, the following governing physics is considered. The total strain ε in the domain is given by

$$\varepsilon_{mn} = \varepsilon_{mn}^{M} + \varepsilon_{mn}^{T} \ \ (m, n = 1,2,3) \qquad (3.8)$$

where ε^M (m/m) and ε^T (m/m) are the mechanical and thermal strains caused by the mechanical forces and temperature changes, respectively.

Considering a linear function between strain and stress, stress for linear elastic materials is defined by:

$$\sigma_{ij} = D_{ijmn}\varepsilon_{mn} \ \ (i, j, m, n = 1,2,3), \qquad (3.9)$$

where σ_{ij} (Pa) is the elastic stress, and D_{ijmn} (Pa) is the tensor of elastic coefficients with 81 components. The components in the tensor decrease to 36 independent components because of symmetrical situation in strain and stress tensors.

Thus, the mechanical and thermal strains can be derived from the following equations

$$\varepsilon_{11}^{M} = \varepsilon_x;\ \varepsilon_{22}^{M} = \varepsilon_y;\ \varepsilon_{33}^{M} = \varepsilon_z;\ \varepsilon_{23}^{M} = \varepsilon_{32}^{M} = \frac{\gamma_{xy}}{2};\ \varepsilon_{31}^{M} = \varepsilon_{13}^{M} = \frac{\gamma_{yz}}{2};\ \varepsilon_{12}^{M} = \varepsilon_{21}^{M} = \frac{\gamma_{zx}}{2} \quad (3.10)$$

$$\varepsilon_{mn}^{T} = \alpha(T - T_{in})\delta_{mn} \quad (m, n = 1,2,3), \qquad (3.11)$$

where γ (m/m) is the shear strain, T_{in} (K) is the initial temperature, α (m/m K) is the linear coefficient of thermal expansion, and δ_{mn} is the Kronecker delta which is expressed as

$$\delta_{mn} = \begin{cases} 1 & for\ m = n \\ 0 & for\ m \neq n \end{cases} \qquad (3.12)$$

Eventually, based on the thermo-elastic constitutive equations, Eq. (3.9), the stresses as the function of the strains are defined by

$$\sigma_{ij} = \frac{E}{(1+\nu)(1-2\nu)}\left[\nu\delta_{ij}\varepsilon_{kk} + (1-2\nu)\varepsilon_{ij} - (1+\nu)\alpha\Delta T\delta_{ij}\right] \quad (i, j, k = 1,2,3) \qquad (3.13)$$

where ν is Poisson's ratio.

Since boundary conditions of all surfaces of the domain in this model are considered as free surfaces with no mechanical force, it is assumed that the stress in the domain is only dependent upon thermal stress formed by thermal changes during sintering as

$$\sigma_{ij} = \frac{-\alpha\Delta T\delta_{ij}E}{(1-2\nu)} \qquad (i, j, k = 1,2,3) \qquad (3.14)$$

3.2.2.3 Mesh Density

Figure 3.8b shows the meshed geometry of the proposed physical domain. In the meshing process, the critical area is the top surface of the silver track that should have finer meshes with the maximum mesh element size less than the laser beam diameter.

The developed model was run with different mesh element sizes where the maximum temperature for each element size was recorded. Increasing the number of mesh elements yields to lower difference between the two subsequent temperatures. In this case, the finer mesh has less to do with the precision of the solution. Thus, it was concluded that the solution is independent of mesh element size for the number of mesh elements above 81000.

The thermo- and opto-physical properties of the bulk materials for the substrate and deposition track are listed in Table 3.5. It has been reported that the physical properties, particularly thermal conductivity of silver nano particles differ from that of bulk material. However, since the amount of silver material applied as a track is pretty small compared to copper and PET, it has been assumed that the difference in the final results in negligible [108]. In order to prove the assumption, the simulation was run while applying two other thermal conductivity values for silver to check the difference in the maximum temperature of the domain. Figure 3.9 shows that the difference is negligible.

Table 3.5. Properties of materials in the domain [21, 22, 23].

Material	***k* (W/m.K)**	**ρ (kg/m3)**	**Cp (J/kg.K)**	**α (1/K)**	***E* (Pa)**	**v**	**β**
Ag	419	10500	244	18.9e-6	83e9	0.37	0.2
Cu	400	8700	385	17e-6	110e9	0.35	0.2
PET	0.38	930	1900	150e-6	1e9	0.35	0.02

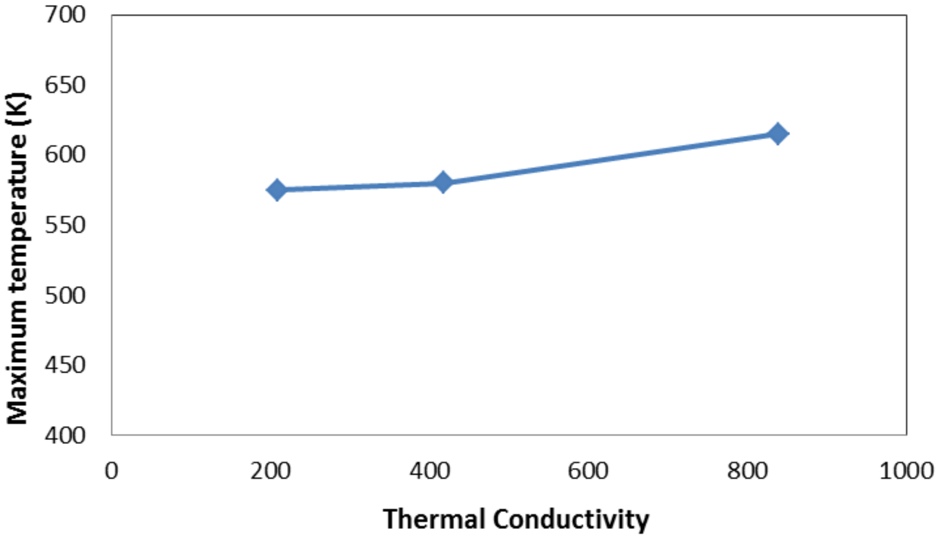

Figure 3.9- Maximum temperature of the domain by varying the thermal conductivity values of the silver.

The simulation code was run at different parameters similar to physical conditions. Based on the laser speed (1 mm/second), it takes 5 seconds for laser to move along the whole interconnect.

At t=0, laser is placed on the spot (0.005, 0.0025, 0.000327) as shown in Figure 3.8a. Then it moves with the constant speed to reach the end of interconnect at the bottom of the slanted edge. Figure 3.10 shows the temperature distribution at 1.24 W laser power for different simulation times. The maximum temperatures at t=4.7 and 4.8 seconds when the laser beam is on the flat surface and slanted edge are about 380 and 580 K, respectively (Figure 3.10a and Figure 3.10b). The significant rise in temperature is resulted from the difference in thermo-physical properties of PET and Cu.

The high transmission rate of PET (above 95% [109]) leads the laser beam to the copper substrate (with a high reflection rate) at the bottom surface of PET. This phenomenon along with the low thermal conductivity of PET seems to be responsible for the significant temperature change occurred on the slanted edge. Figure 3.11 shows maximum temperatures at different laser powers of 0.44, 1.24, and 1.7 W. Clearly, a raise in the laser power results in an elevated heat in the samples. A sharp increase in the temperature is observed after 4.8 seconds when the laser point irradiates on PET at the slanted edge. The temperature is instantly reduced to the substrate initial temperature (360 K) when the laser point passes the sample after 5 seconds due to heat convection.

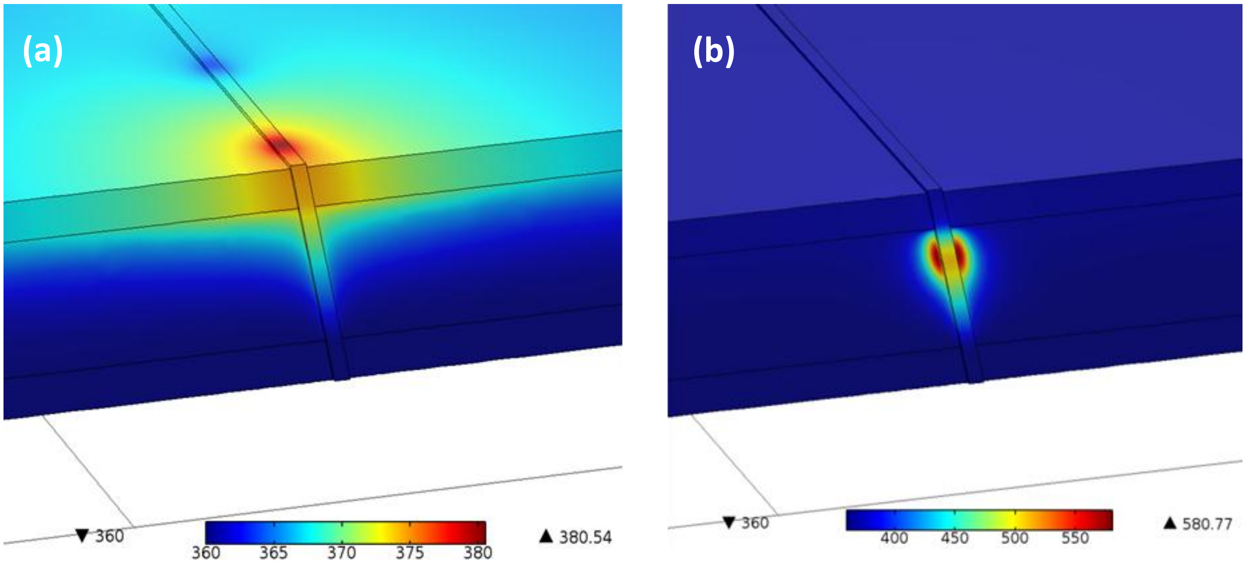

Figure 3.10. Temperature profile at a laser power of 1.24 W after a) 4.7 s, and b) 4.8 s.

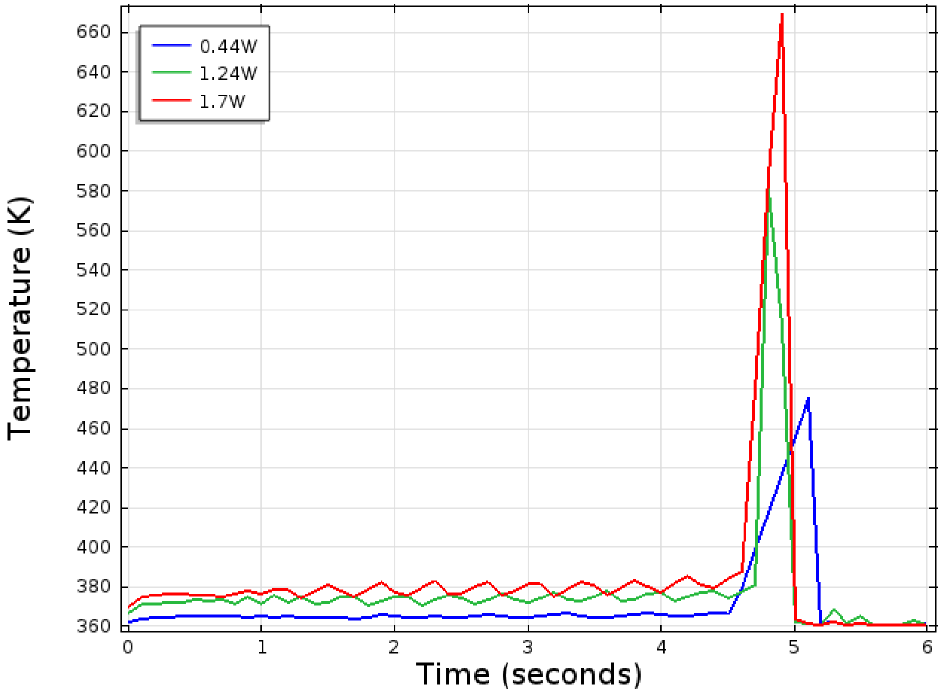

Figure 3.11. Maximum temperature plot at laser powers of 0.44, 1.24, and 1.7 W versus simulation time.

Figure 3.12 depicts von Mises stress profile at the laser power of 1.24 W at different cross sections. Figure 3.12 a shows that the maximum stress is formed at the interface of copper, PET, and the silver track on the slanted edge which is about 636 MPa at the laser power of 1.24 W. Figure 3.12 b also indicates the 2D profile of the stress on the xz-plane at y=2.48 mm where the maximum thermal stress profile is observed at the triple interface of the top copper plate, PET layer, and the silver track.

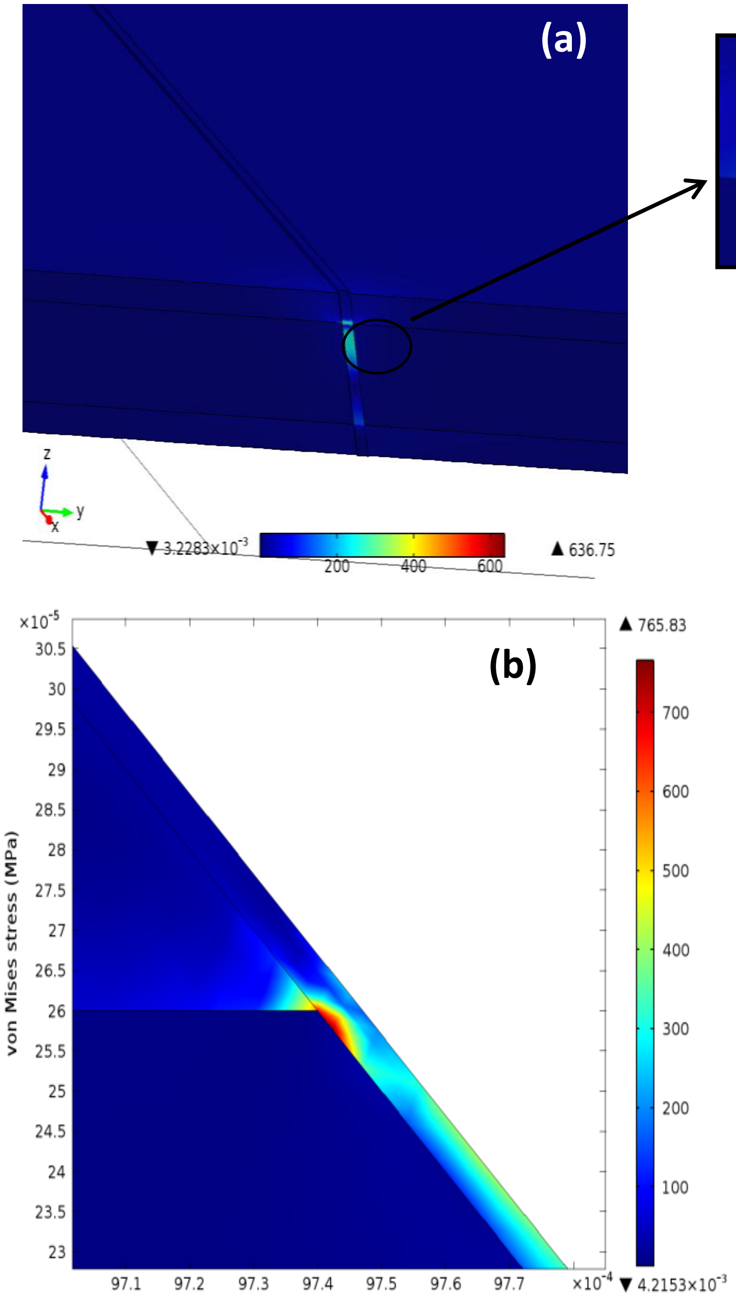

Figure 3.12. Von Mises stress profile at laser power of 1.24 W at time=4.8 s, a) inset shows that the highest stress is occurring at the interface of copper, PET, silver track, and b) xz-plane cross section at y=2.48 mm. The stress unit is in MPa.

Maximum von Misses stress in the domain throughout the simulation time is shown in Figure 3.13. The stress trend in the domain at different laser powers correlates with that of temperature indicating a higher stress when the laser point reaches the slanted edge and the triple intersection.

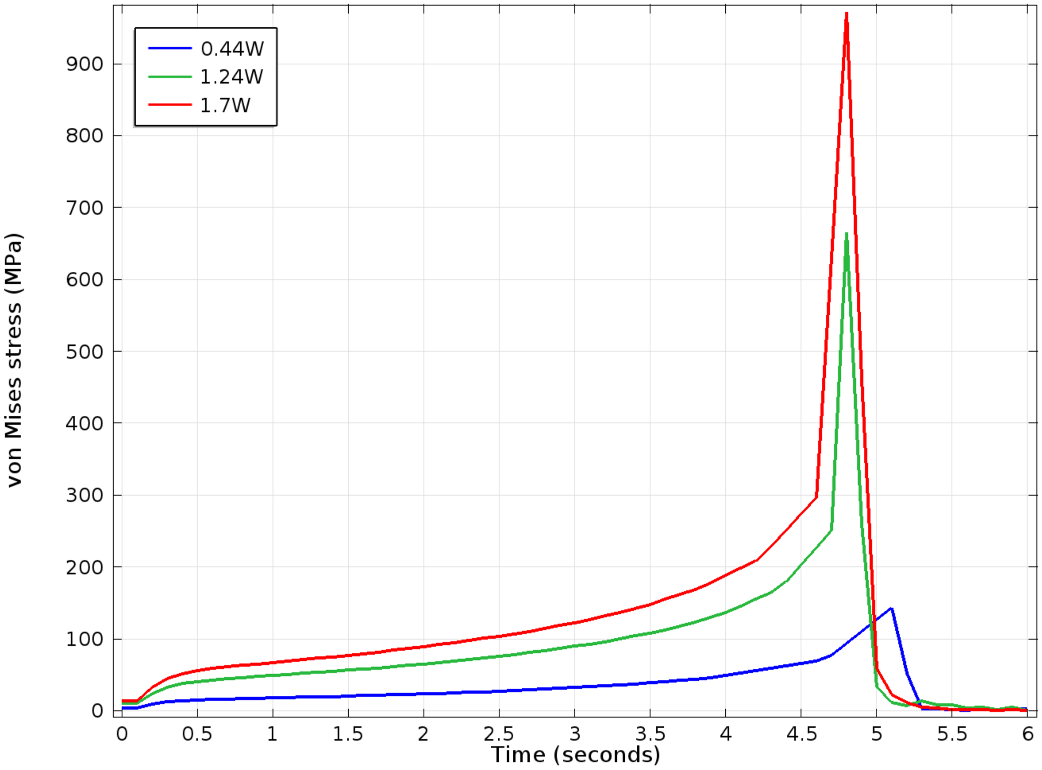

Figure 3.13. Maximum von Mises stress at laser power of 0.44, 1.24, and 1.7 W.

The enlarged non-scaled displacement in the domain is also shown in Figure 3.14. The maximum displacement occurs at the bottom copper substrate and the slanted edge deviating from 1.5 to 2 microns. Figure 3.15 displays the total displacement throughout the simulation time. Thermal expansion of the samples by the temperature rise brings about the displacement of the substrates and silver track leading to the formation of residual stress in the samples. There is a shift in the displacement curve of laser power 0.44 W (blue curve) which could be attributed to numerical errors in the simulation and mesh topology that could potentially be dominant at lower power creating singular points in the numerical solution. It will be seen in the experimental results that since the samples are small, even small displacement may result in crack formation in the silver track as discussed in the following section.

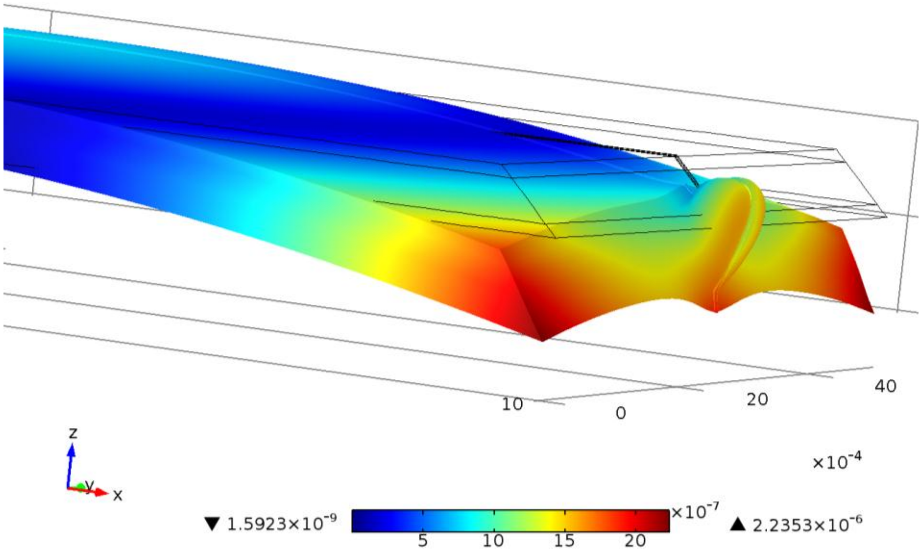

Figure 3.14. Total displacement profile at the laser power of 1.24 W after 4.8 seconds. Units are in meter.

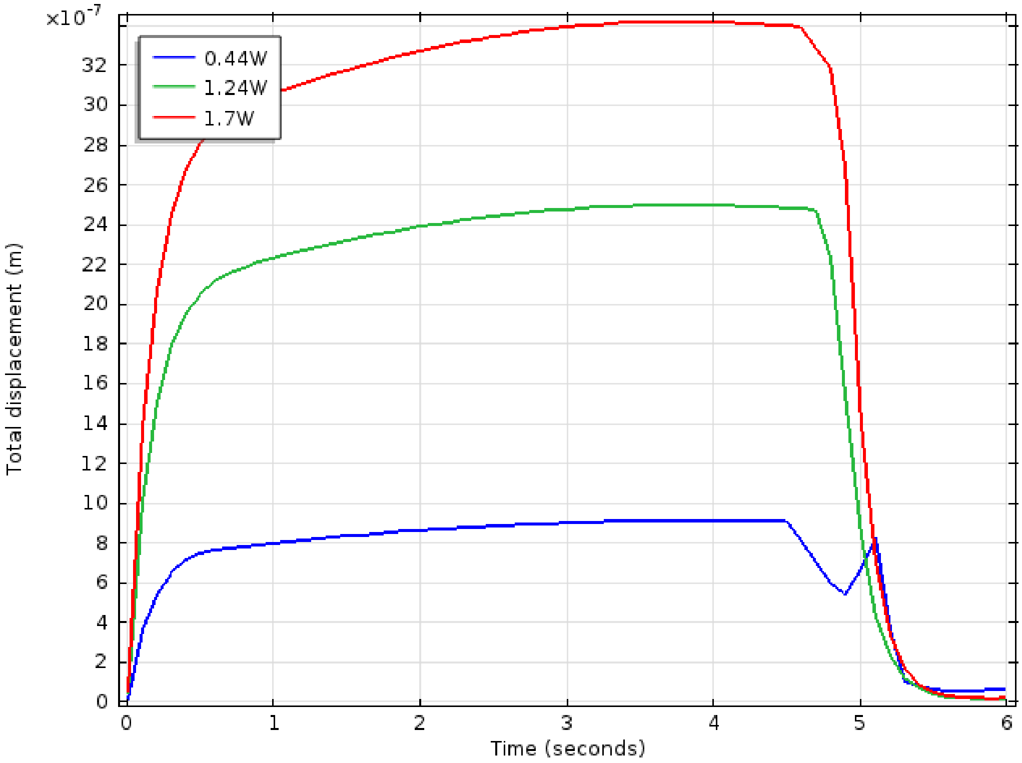

Figure 3.15. Total displacement plot at laser power of 0.44, 1.24, and 1.7 W.

The numerical study performed in this study suggests that substantial displacement/strain exists in the domain and particularly at interfaces. As shown in Figure 3.13 the highest amount of Von Mises stress is induced within the silver track at the interface of PET and top layer of copper. These results suggest that the interfaces of such samples are prone to crack formation and possible delamination. Although the displacement curves shown in Figure 3.15 indicate higher amount of displacement for laser power 1.24 W compared to 0.44 W, limited cracks are observed for the silver tracks sintered at laser power 1.24 W compared to the 0.44 W conditions. It is noteworthy that sintering of the particles in the silver track and formation of stronger bonding are not taken into account in the numerical modelling. Hence, observation of less cracks in the silver track sintered at laser power 1.24 W compared to 0.44 W shows a reasonable sintering occurred between the silver nanoparticles.

Based on the modeling results shown in Figure 3.11, maximum temperature when laser power is 1.7 W goes over decomposition temperature of PET (633 K). The maximum temperature at the low laser power, which is calculated 477 K, is not high enough to successfully sinter the nanoparticles in this short laser interaction time.

The abovementioned experimental observation support the modeling results since cracks are mainly seen in the silver tracks on or nearby the PET/Cu interfaces. However, it should be noted that 450 K temperature is high enough for the sintering of silver nanoparticles in the oven when the sintering time is 30 minutes. Since laser sintering is done fairly quickly, a higher temperature is needed for nanoparticles to stimulate diffusion among interfacing atoms to rapidly form the sinter neck.

3.3 Summary

This study presented the feasibility of LAMM for the production of conductive non-planar interconnects between the two layers of copper in a double-sided copper substrate separated by a layer of PET. Although feasible, the process is extremely sensitive to the variation of process parameters. The tests done with 1.24 W laser power in sintering step resulted in conductive samples with ~3.2 Ω resistance. Furthermore, a 3D finite element model was developed to simulate the process while being used for this application. The model includes a coupled thermal and structural multi-physics domain. The thermal-structural interaction model predicted that the maximum strain occurs around the Cu/PET interface that may cause cracks formation at this area as observed in the experimental samples. Comparing the numerical and experimental results suggest that regardless of a short laser exposure time on Ag nanoparticles during sintering, local temperature higher than 580 K may suffice for the sintering of Ag nanoparticles where this temperature is obtained at 1.24 W laser power.

Chapter 4. Micro-scale Aerosol-jet Printing of Graphene Interconnects*

Flexibility and crack formation issues in Ag NP interconnects (discussed in the previous chapter) created a keen interest to replace Ag NPs with a material which has the same or even better electrical properties, mechanical and physical properties in printing interconnects compared to nano-silver. Graphene with high electron mobility, intrinsic strength, and flexibility was a prominent contender which can come up to our expectations. This chapter addresses the deployment and characterization of a micro-scale aerosol-jet additive manufacturing technology to print graphene interconnects. As discussed in Chapter 1, the first step in printing of graphene is making highly concentrated graphene ink to attain desired properties from the tracks created by the less number of the printed layers. Chemical vapor deposition growth (CVD) [28], liquid-phase chemical exfoliation of graphite [29], and liquid-phase exfoliation of reduced graphene oxide (rGO) [30] are of the most applicable developed approaches for the production of graphene. The outcome of the low-cost liquid-phase exfoliation technique is favorable for the printing methods. However liquid-phase exfoliation technique yields dispersion with very low graphene content, i.e. less than 0.1 mg/ml. Adding a polymer such as ethyl cellulose (EC) during exfoliation process, as a stabilizer, could increase graphene concentration to around 0.2 mg/ml which was not still high enough for high quality printing purposes. Many methods have been employed to increase concentration of graphene, either in a stabilized form or others, from a solvent into another one with a lower volume such as the iterative solvent exchange [15, 110], distillation process [111], and extracting stabilized graphene powder from dispersion followed by

---

* Jabari, E., and Toyserkani, E., 2015, "Micro-Scale Aerosol-Jet Printing of Graphene Interconnects," Carbon, **91**pp. 321-329.

redispersing in the needed solvent [14]. In the present work, the latter approach was chosen that exhibited more compatibility with the aerosol printer. In this work, a highly concentrated graphene ink with viscosity of 21 cP and 3.1 mg/ml graphene flakes with the lateral size below 200 nm was developed and adopted for this process to make a reliable and repeatable graphene deposition on the treated Si/SiO_2 wafers. To this end, the influence of the most significant process parameters, including the atomizer power, the atomizer flow rate, and the number of the printed layers, on the size and properties of graphene interconnects was studied. Results show that the aerosol-jet printing process is capable of printing micro-scale graphene interconnects with variable widths in the range of 10 to 90 micron. These patterns, as the finest printed graphene patterns, with resistivity as low as 0.018 Ω.cm and sheet resistance of 1.64 kΩ/□ may ease the development of miniaturized printed electronic applications of graphene.

4.1 Experimental procedure

4.1.1 Preparation of Stabilized Graphene Powder

In the present work, chemical exfoliation of graphite in ethanol using sonication power is used to make graphene sheets. This procedure is based on Secor et al.'s work [14]. In this chemical exfoliation process, sonication has been used to separate graphite sheets in the ethanol solvent. Ethyl cellulose (EC), as an stabilizer polymer, is also added to the exfoliation solution to increase the yielded amount of graphene in ethanol and prevent reagregation of the flakes in the final high concentrated ink [110]. In the first step, 2 g of natural graphite flakes (3061 grade, Asbury Graphite Mills, Absury, USA) was added to ethyl cellulose (EC) (EC: Aldrich, viscosity 4 cP, 5% in toluene/ethanol 80:20, 48% ethoxy) solved in ethanol inside a 50 mL centrifuge tube. Then, 8 tubes were sonicated in a bath sonicator (B2500A-DTH, Ultrasonics Cleaner, VWR North American, Burlington, ON, Canada) for several hours. After sonication, the samples sited for an hour to allow all the large graphite flakes to settle in the bottom of the centrifuge tubes. Top solution was transferred to another tube and centrifuged (Sorvall™ Legend™ X1 Centrifuge Series, Thermo Scientific™) at 10,000g for 15 minutes to remove large aggregate of graphite flakes (sediment). Supernatant, which is a dispersion of graphene/EC in ethanol, was collected and transferred to another centrifuge tube. The centrifugation process was repeated for one more time to make sure that the final dispersion does not contain graphite flakes.

Although the addition of ethyl cellulose (EC) in chemical exfoliation of graphite increases yield amount of graphene, the concentration of graphene in ethanol in this step (around 0.2 mg/ml) was not high enough for printing purposes. Thus, the stabilized graphene flakes needed to be flocculated and dried as powder to be redispersed in desired solvents with desired concentration for printing. To this end, the excessive solvent and EC needed to be removed. It was accomplished by the addition of an aqueous solution of NaCl to the dispersion. For this, an aqueous solution of NaCl (99.5%, EMSUR®, Denmark) mixed with the 5 times more diluted dispersion in a 2:1 volume ratio. Adding NaCl to this dispersion resulted in flocculation of graphene/EC solid, which was easily separated using a short centrifugal process at 10,000g for 10 minutes.

The dried graphene/ EC composite sheet with high flexibility, collected from the wall of one of the centrifuge tubes, is shown in Figure 4.1.

Figure 4.1. Graphene/EC composite sheet.

Afterward the dried graphene/EC solid re-dispersed in ethanol, and flocculated again by adding NaCl solution and separated using the centrifugation process. Since the solid may contain some salt residue, it was washed with deionized water and collected using vacuum filtration (0.45 μm filter paper, Nylon, HNWP, Millipore). Finally, a fine dark grey powder obtained (Figure 4.2).

Figure 4.2. Yielded dark grey powder.

4.1.2 Graphene Content in Graphene/EC Powder

In order to quantify graphene content in the powder, Ultraviolet-Visible (UV-Vis) absorption spectroscopy (UV-2501PC, Shimadzu, Japan) was considered as a standard method by measuring optical absorbance of a dispersion of the powder. Using Beer-Lambert law, which relates the absorption factor to the graphene concentration, graphene concentration in dispersion can be obtained as follows [112]:

$$A = \propto C_G l$$

where A is measured absorbance, $\propto$ is absorption coefficient, C_G is graphene concentration, and l is path length of spectrometer. The previously measured absorption coefficient at wavelength of 660 nm ($\propto_{660} = 2460\ L/g.m$) was used in calculations [29].

Some parameters were changed to optimize the procedure of the making powder in order to obtain higher graphene content in the powder. In Table 4.1, concentration of graphene in 2 mg/ml dispersions of various powders (obtained in different conditions) in ethanol calculated by described Beer-Lambert law is listed and finally graphene content in the each powder is calculated. These measurements were done at different dilutions of each powder.

Table 4.1. Prepration conditions, graphene concentration in 2 mg/ml dispersions of the powder in ethanol, and graphene contents of different powders.

Powder	EC Added at the Exfoliating Process (% w/v)	Sonication Time (hours)	NaCl Concentration (mg/ml)	Absorbance of Graphene at 660 nm (m^{-1})	Concentration of Graphene (mg/ml)	Graphene: EC Ratio
1	2	13	40	1.03	0.04	2:98
2	2	27	40	1.58	0.06	3:97
3	0.75	27	40	2.43	0.09	4.9:95.1
4	0.75	27	80	2.58	0.10	5:95

Figure 4.3 shows absorbance of each powder as a function of the wavelength in UV-Vis absorption spectroscopy of the powders.

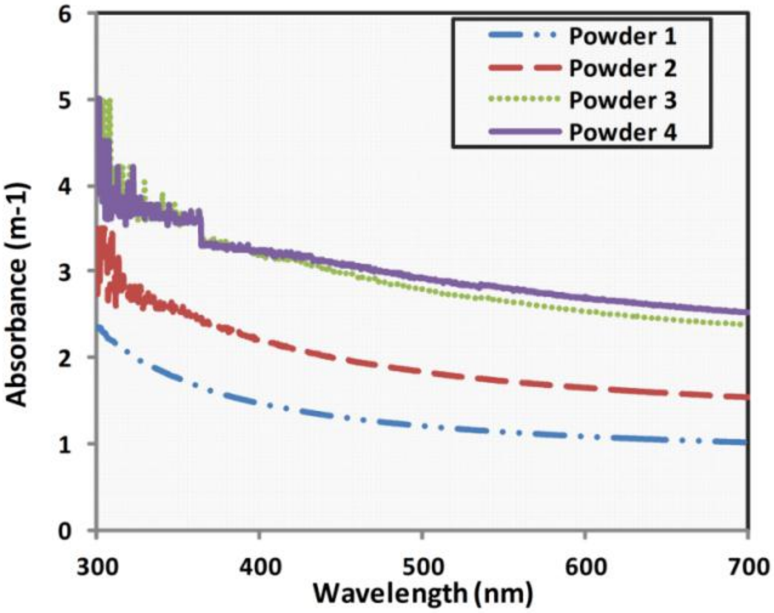

Figure 4.3. Optical absorbance characterization of different powders showing absorbance as a function of the wavelength.

As the results suggest, the graphene content of the powder has not significantly been changed by increasing the concentration of NaCl solution from powder 3 to powder 4. So, powder 3 is chosen as the final powder which is high in graphene content and low in NaCl residues.

4.1.3 Thermal Gravimetric Analysis (TGA) of Graphene/EC Powder

In order to find a proper annealing temperature of graphene/EC composite, prepared powder was analyzed using a TGA system ((Mettler Toledo TGA/SDTA851, Mississauga, Canada**)** at a heating rate of 5°C/min in air. The Mass change while temperature is increasing from 100°C to 600°C is shown in Figure 4.4.

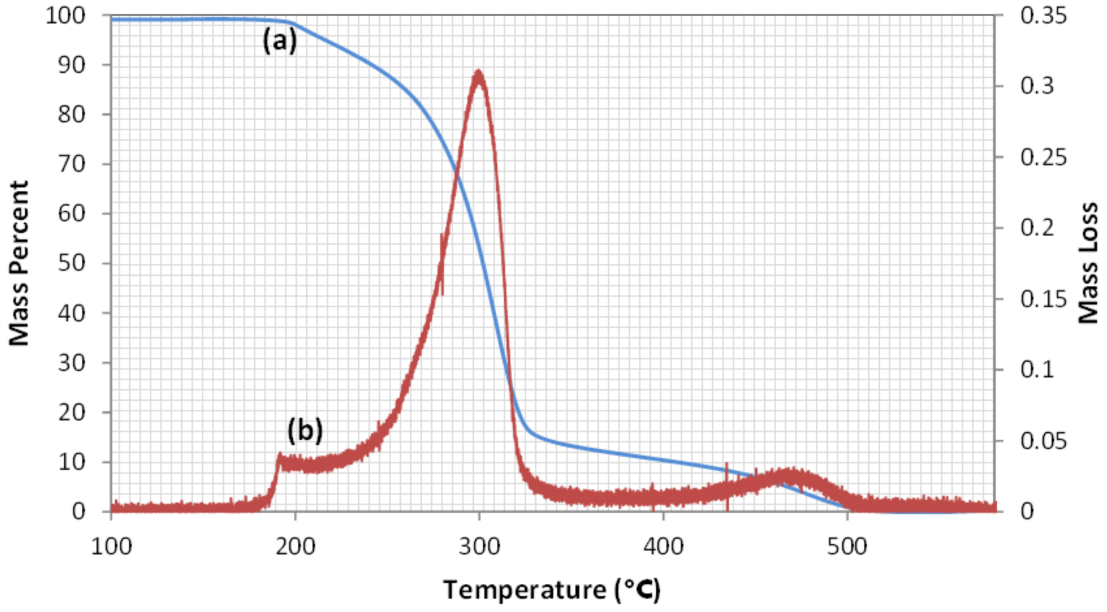

Figure 4.4. TGA results of pure EC powder and G/EC powder showing (a) mass changes versus temperature and (b) the differential mass loss.

It is concluded that the existing EC in the powder decomposes in two different steps at temperatures around 200°C and 300°C, respectively. Thus, the samples are annealed at 400°C, to completely remove EC from graphene/EC composites.

4.1.4 Characterization of the Graphene Flakes in Graphene/EC Powder

In order to determine properties of synthesized graphene powder, characterization of the powder was done using scanning electron microscopy (1550 FESEM, Zeiss, Oberkochen, Germany), atomic force microscopy (Dimension 3100 AFM, Nanoscope software, Veeco Instruments Inc., NY, USA), Raman spectroscopy (532 nm excitation laser, Bruker Raman Sentrerra, Bruker Optics Inc., USA), and X-ray photoelectron spectroscopy (XPS, Quantera II spectrometer, Physical Electronics (PHI), MN, USA).

To observe graphene flakes by SEM and characterize them by Raman Spectroscopy and XPS, a dispersion of 90 mg/mL of the powder in 70:30 terpineol/ethanol solvents prepared and drop-casted on a pre-heated Si/SiO_2 wafer to form a graphene/EC sheet on the wafers. Prepared samples baked on a hot plate at 400°C for 30 minutes to completely remove solvents and EC.

SEM photos, Raman spectroscopy, and XPS results are depicted in Figure 4.6.a, b, and c respectively.

To measure thickness of the flakes via AFM, a diluted dispersion of the graphene/EC powder in ethanol with graphene concentration of 0.003 mg/ml was drop-casted onto preheated (220°C) Si/SiO$_2$ wafers. It is found in the previous literature that preheating of the substrate to a temperature higher than the boiling point of the solvents decreases possibility of reaggregation during deposition and consequently results in the most consistent deposition of nano-sheet, as the solvents evaporate once deposited [113]. Before drop-casting, a modification was done on the surface of the silicon wafers using 3-aminopropyl triethoxysilane (APTES, Sigma-Aldrich, 99%). The wafers were left in 2.5 mM solution of APTES in 2-propanol for 30 minutes, rinsed with 2-propanol and dried under a stream of N2. The prepared 0.003 mg/ml graphene dispersion was dropcast and left onto the wafers for 10 minutes, dried with N$_2$ and rinsed with 2-propanol [14]. To completely remove ethyl cellulose and clearly observe graphene flakes, the samples were annealed at 400°C on a hot plate for 30 minutes. A Dimension 3100 AFM system in tapping mode with Nanoscope Analysis software was used for the characterization of the flakes. To measure thickness of the flakes, the severely aggregated flakes, those were recognizable from phase contrast images, were skipped. Results are given in Figure 4.7.

4.1.5 Preparing Graphene Ink

In order to prepare a highly concentrated graphene ink compatible with the aerosol printing in terms of particle size and viscosity, cyclohexanone was chosen as the solvent for synthesized powder. It can dissolve a high concentration of graphene and has a well-matched surface tension with aerosol-jet printing process [112, 114]. Dispersing 60 mg/mL of the powder in cyclohexanone yielded viscosity around 9 cP (measured by LDVD-I prime, BROOKFIELD viscometer, USA). Although this ink was injectable with the aerosol setup, the printed patterns suffered from coffee-ring effects. To overcome the coffee-ring effect, terpineol as the second solvent was added to cyclohexanone. Terpineol was chosen firstly due to its viscosity (~ 67 cP at 20ºC), which is significantly high to overcome coffee ring effect. It has been also demonstrated to be capable of dispersing high concentration of graphene [110]. Furthermore, terpineol-based inks are of the main efficient inks in ink-based printing technologies because of high viscosity and boiling temperature of terpineol [14, 111].

Eventually, a solution consists of 92.5:7.5 cyclohexanone/terpineol was chosen as the solvent. The resultant dispersion was passed through a 0.2 μm filter (0.2 μm PTFE Membrane, Acrodisc® CR 25 mm syringe filter, Pall) to limit the flake size to smaller than 200 nm. The flakes with this size range are atomize-able by the aerosol-jet printing system. This resulted in an ink, shown in Figure 4.5, with concentration around 3.1 mg/ml and viscosity of 21 cP which was fairly compatible with aerosol-jet printing system and brought about printing patterns with no coffee-ring and defined edges.

Figure 4.5. Highly concentarted prepared graphene ink.

4.1.6 Treatment of Thermally Oxidized Silicon Wafers as the Substrate

For easier observation and more precise characterization of the printed patterns, Si/SiO_2 wafers with 300 nm silicon dioxide were chosen as the substrates. However, intrinsic doping level of graphene and hysteretic behavior of graphene on Si/SiO_2 substrate with a hydrophilic surface necessitate treatment of the substrate. As reported by other researchers, electronic properties of graphene strongly depend on these two factors as well as morphology and deficiencies of the substrate and contamination of graphene surface during process [115, 116]. Some procedures have been employed so far to diminish intrinsic doping and hysteretic behavior of graphene. They include heating the sample under vacuum condition to over 140 ˚C [117] and chemical hydrophobization of surface of the substrate [115]. Some studies show that graphene goes back to its initial state (in terms of doping) [115] or even gets worse [33] once it exposes back to the air. The problems with doping and hysteretic behavior are under the ambient condition.

Nevertheless, chemical hydrophobization of the substrate suggests more efficient way to have low doping level and weak hysteretic behavior [115]. For this, surface modification of Si/SiO_2 wafers was done using hexamethyldisilazane (HMDS, Aldrich, >99%).

First, Si/SiO_2 wafers with 300 nm silicon dioxide (4" 3000A Thermal Oxide, ANY TYPE, wrs Material, USA) were cleaned by bath sonication in ethanol for 20 minutes. An O_2 plasma treatment (Plasma Cleaner, Reactive Ion Etching (RIE), Trion technologies, Florida, USA) were then employed for 5 minutes to remove all the organic residues. Afterward, to hydrophobize surface of the wafers, they were left in a dish of 1:1 HMDS/acetone for 20 hours. The wafers were then rinsed with 2-propanol and dried under a stream of inert Argon gas. Formed HMDS film made silicon surface hydrophobe [14, 115].

4.1.7 Microdeposition process and Characterization of the Printed Patterns

The prepared graphene ink was placed in the ultrasonic actuator of the aerosol-jet printer ($M^3D^®$Aerosol Jet technology, $Optomec^®$ Inc., Albuquerque, USA) to print interconnects. Printed patterns were simply annealed on a hot plate at different temperatures to remove solvents and stabilizer polymer respectively. To see properties of deposited graphene patterns such as, graphene structure, the number of layers, and the amount of lattice defects, Raman spectroscopy was done by a Bruker Raman Sentrerra (532 nm excitation laser). To closely observe quality and microstructure of the patterns scanning electron microscopy and atomic force microscopy were employed. Sheet resistance of the printed graphene sheet was measured using a 4-probe system and afterward Van der Pauw method was employed to calculate resistivity of the printed graphene.

4.2 Results and Discussion

4.2.1 Characterization of the Graphene Flakes in Graphene/EC Powder

SEM image of the graphene flakes in the prepared powder (Figure 4.6 a) shows a high density of the flakes with nano lateral size which is necessary for the printing process to effectively atomize the ink by ultrasonic atomizer and convey it by the gas flow toward the nozzle. The Raman measurement of drop-casted sample on Si/SiO_2 wafers was performed at room temperature using a green laser beam (532 nm) at an excitation rate with 20 mW incident power (Figure 4.6). The G band at around 1580 cm^{-1} and 2D band at around 2700 cm^{-1}, which are the two most distinct bands for all the graphite and graphene samples, are observed in Raman graph. D band is also observed around 1350 cm^{-1} whose intensity is related to the number of lattice defects. The ratio of D band intensity to G band, which is considered as estimation for number of the defects, is around 31%. This value seems to be in low range of those in all reported surfactant exfoliated graphene solutions and reduced graphene oxide [29, 118]. The bonding structure was also investigated using XPS with an Al K_α X-ray (1486.7 eV) source (Figure 4.6 c). As shown in Figure 4.6 c, peaks at 284.3, 284.8, 285.3, and 286.3 eV are fitted with sp^2 carbon bond [119-121], sp^3 carbon bond [120, 121], C-OH [119, 122], and C-O [119-121], respectively. The total amount of sp^2, sp^3, C-OH, and C-O bonds, determined by an area ratio method [121], is around73%, 12.5%, 13%, and 2%, respectively. The results reveal that only a few percent of carbon is oxygenated. The ratio of sp^3/ sp^2 is calculated 0.17 which is in good agreement with the ratio of I_D/I_G obtained from Raman spectrum. The C/O ratio, determined by atomic composition of the sample [123], is around 6. This amount of oxygen can be due to the adsorption of oxygen, either from immediate environment or from decomposition of EC, on the surface of graphene. It is concluded that exfoliation, flocculation and drying processes result in obtaining the graphene structure with low amount of defects and oxidization.

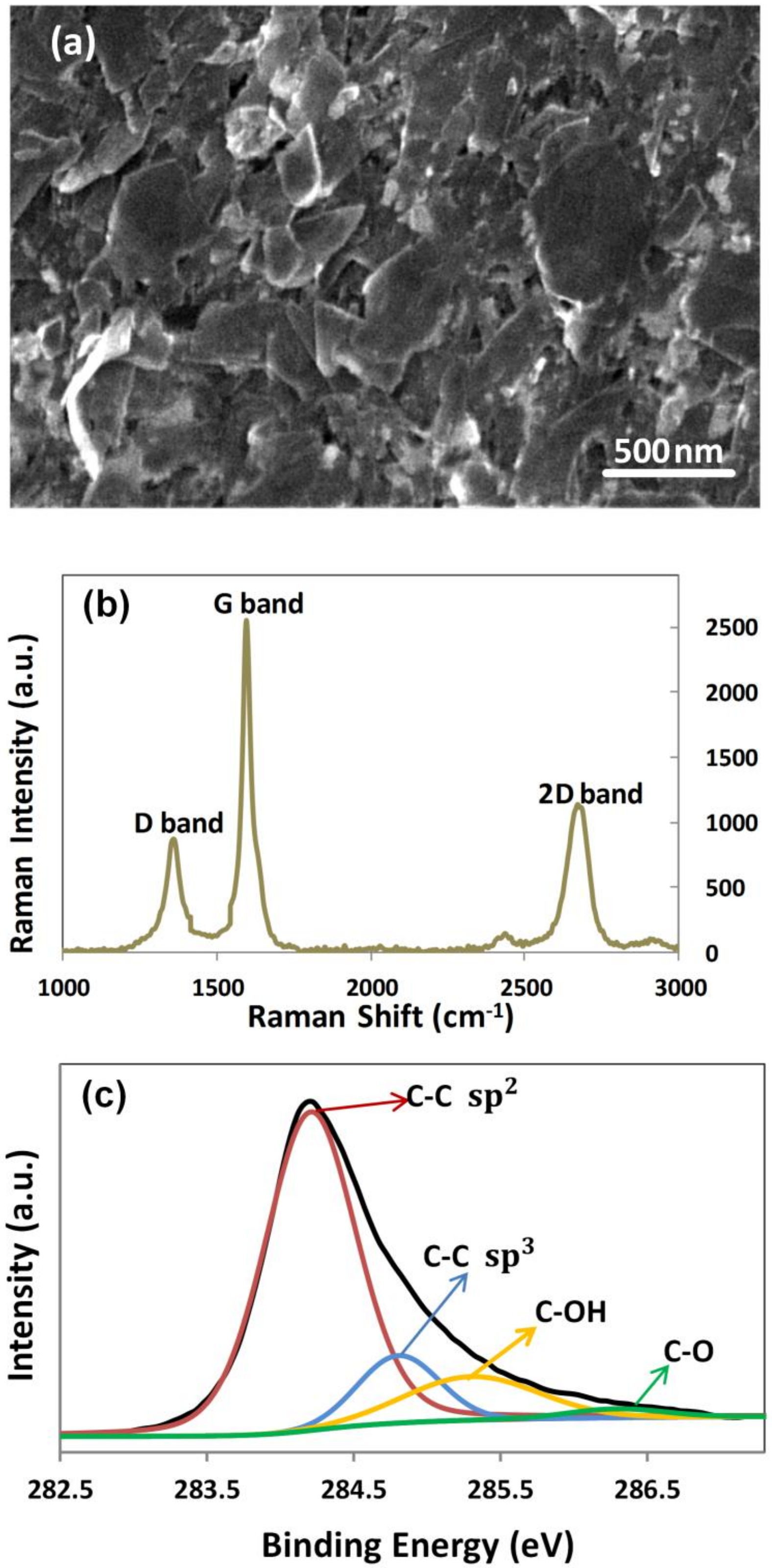

Figure 4.6. a) SEM image, b) Raman, and c) XPS spectra of graphene flakes in a drop-casted and fully annealed highly concentrated dispersion of the stabilized graphene powder on Si/SiO$_2$ wafers.

In Figure 4.7 a, an AFM image of graphene flakes on Si/SiO$_2$ wafer is shown. Flake thickness is measured for 140 flakes (not severely reaggregated ones [113]) and the results are reported in Figure 4.7 b as a flake size histogram. The mean flake thickness of 2.11 nm states that the powder mostly consists of multi-layer graphene flakes. Considering an effective thickness of 0.34 nm for single layer graphene [124] and mean thickness of 2.11 nm for the exfoliated graphene flakes, it can be concluded that each exfoliated graphene flake has approximately 6 layers.

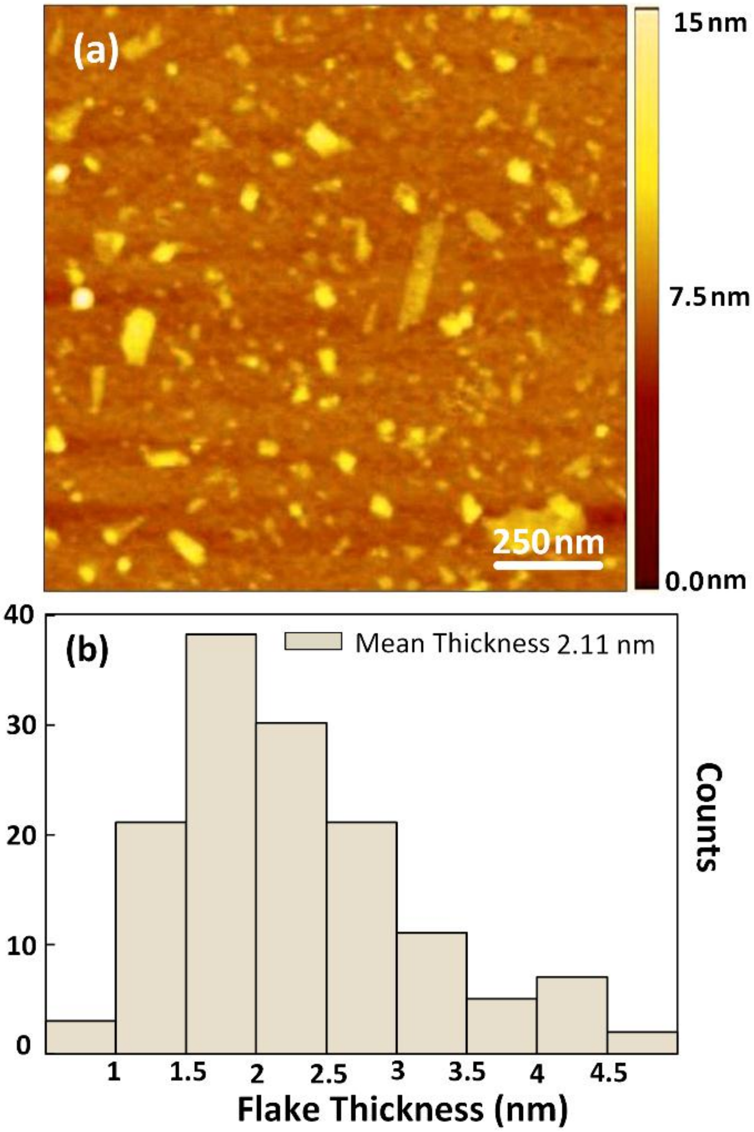

Figure 4.7. a) AFM image collected with 0.5 Hz scan rate from 1.4 µm×1.4 µm scan area, b) AFM height histogram for 140 graphene flakes in a drop-casted and fully annealed diluted dispersion of the stabilized graphene powder on Si/SiO$_2$ wafers.

4.2.2 Microdeposition Process and Characterization of the Printed Patterns

In the microdepostion step, process parameters should precisely be optimized to arrive at high quality patterns/interconnects. The values of the main parameters including, atomizer power, sheath gas and atomizer flow rate, deposition velocity, and temperature of the substrate, strongly depend on the properties of the ink, surface quality of the substrate, and needed pattern size. So based on the utilized substrate and the desired pattern size, different parameters of the aerosol-jet process were chosen. After the deposition process, the patterns consist of all the components of the ink including graphene, EC, cyclohexanone, and terpineol. To achieve the pure graphene patterns, solvents and even EC should be burned off during the post heat treatment. At temperature above 220 ºC (higher than boiling temperature of both solvents), both solvents evaporate. Based on TGA results, ethyl cellulose also decomposes in various steps at different temperatures. In the present study, the samples were annealed at 250ºC and 400ºC to compare the properties of graphene/EC and pure graphene patterns, respectively. A hot plate was simply used to anneal the samples. It has to be noted that temperature of the substrate during the deposition process was kept at 100˚C which results in printing more uniform patterns due to improving surface energy and promoting adhesion.

Deposition was done on Si/SiO_2 wafers with 300 nm silicon dioxide with treated surface as explained before. It is concluded that the aerosol-jet set up is capable of printing patterns with defined edges and controllable width ranging from 10 to 90 (µm). These patterns are the finest printed graphene patterns reported to date. Table 4.2 depicts some of the aerosol-jet printing parameters during the deposition on silicon wafers and the mean width of the patterns (measured for 10 printed patterns) after annealing at 400˚C. The width of the as-printed patterns is almost the same as annealed patterns and is also independent of annealing temperature. It is due to surface energy of the heated and treated Si/SiO_2 wafers during printing process.

Table 4.2. Some various conditions of the aerosol-jet printer in the printing process of graphene ink on treated Si/SiO$_2$ wafers and the mean width of their resultant patterns (measured for 10 printed patterns) after annealing at 400°C. Sheath gas flow rate and deposition velocity are 50 ccm and 0.2 mm/sec, respectively in all the conditions.

Pattern Number	Atomizer Flow Rate ±1 (ccm)	Ultrasonic Atomizer Power (V)	Mean Width of the printed Pattern ±1 (μm)
1	50	50	90
2	48	50	65
3	38	50	52
4	30	50	32
5	25	50	13
6	48	48	45
7	38	48	36
8	30	48	20
9	25	48	10

The patterns, listed in Table 4.2, with 6 printed layers and annealed at 400˚C, are captured using SEM and shown in Figure 4.8. The sheath gas of the printing system mostly affects the quality of the patterns rather than the width of the patterns. Hence in all the mentioned conditions in Table 4.2, sheath gas flow rate was kept constant (around 50 ccm) to print patterns with different widths to present the capability of the system. It is concluded that increasing either the atomizer flow rate or the atomizer power results in the wider patterns. Figure 4.8 c illustrates the trend of the changes in the size by increasing the atomizer flow rate and the atomizer power.

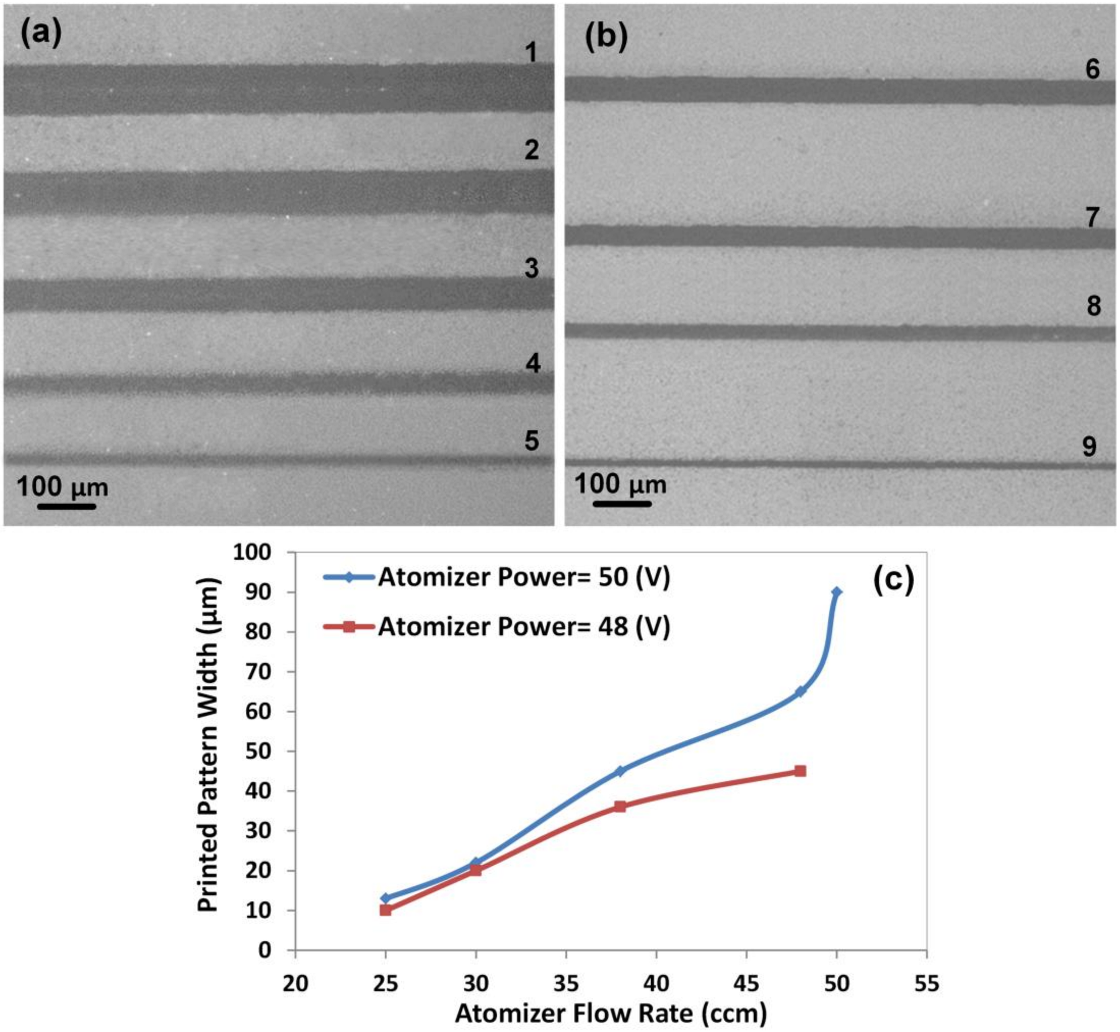

Figure 4.8. SEM images of 6-layer graphene patterns on treated Si/SiO$_2$ wafers printed with different atomizer flow rate listed in Table 4.2 with atomizer power of a) 50 (V) and b) 48 (V). c) The width of the graphene patterns versus atomizer flow rate in different atomizer power.

Figure 4.9 shows atomic force microscopy of pattern 9, and its section analysis along the line. The figure indicates that the process results in printing patterns with defined edges and free of coffee-ring effect.

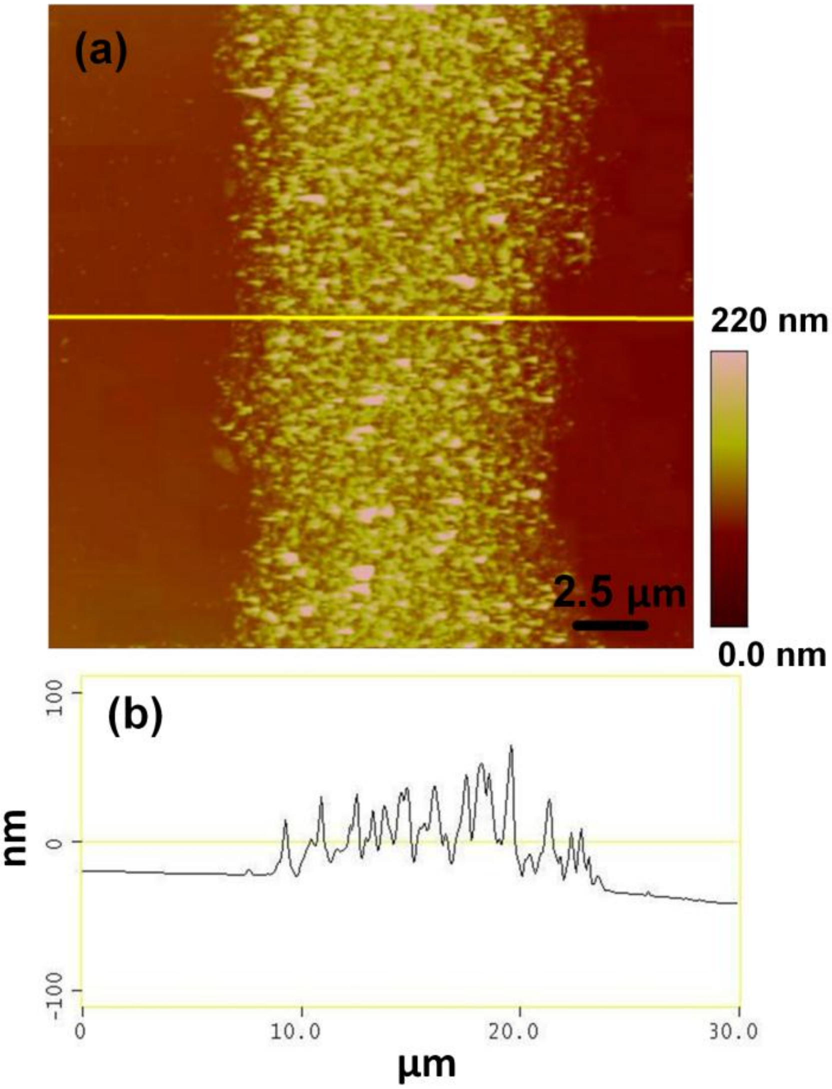

Figure 4.9. a) AFM of pattern 9 introduced in Table 4.2 and shown in Figure 4.8, b) Section analysis on defined line.

SEM images of microstructure and Raman Spectra for the as-printed patterns and patterns annealed at two different temperatures are shown in Figure 4.10. The SEM images show high density of connected graphene flakes even after annealing at 400°C. The SEM images also show that the edges of the flakes are more creased compared to the flakes of the ink before printing, which is shown in Figure 4.6 a. It can be an indication of some degree of wrinkling in the graphene flakes in the printed graphene features. Since crumpling of the graphene sheets leads to improve performance of graphene-based devices [22-26], due to high resistivity of wrinkled graphene sheet to re-aggregation, these printed patterns seems to be desirable in electronic and energy-storage devices.

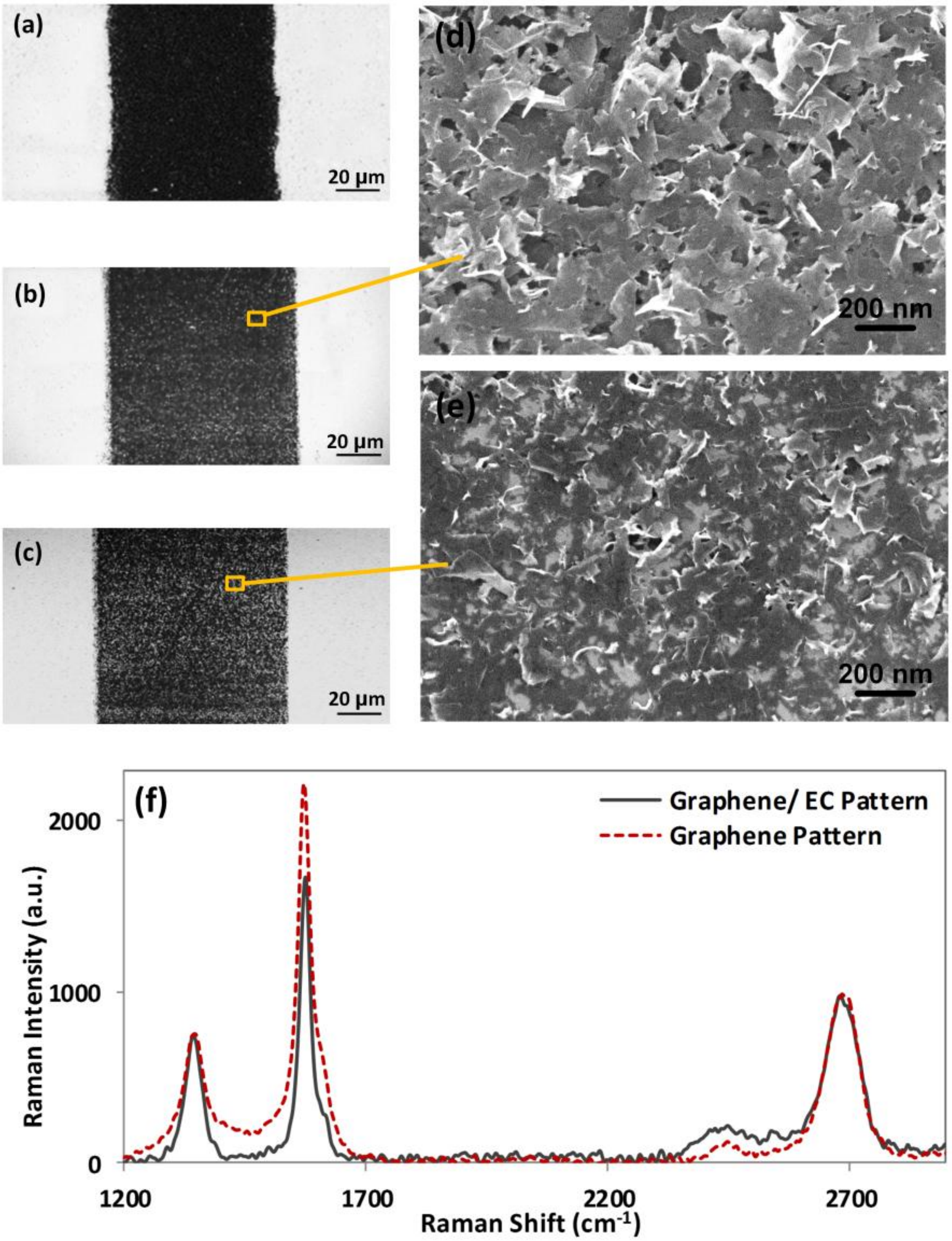

Figure 4.10. SEM image of a) 6-layer as-printed graphene/EC pattern. b and d) 6-layer graphene/EC pattern annealed at 250°C. c and e) 6-layer graphene pattern annealed at 400°C. f) Raman spectra of the printed patterns anealed at 250°C (graphene/EC pattern) and 400°C (graphene pattern). Deposition of the patterns was done with velocity of 0.2 mm/s at 50 ccm sheath gas flow, 49 ccm atomizer flow, and 50 V atomizer power.

The ratio of D band to G band in Raman spectra of the samples annealed at 250˚C and 400˚C are 41% and 33%, respectively. It is concluded that printing and annealing processes do not significantly change the level of the defects in graphene and graphene-based patterns. Decreasing the ratio of D band to G band by increasing the annealing temperature to 400˚C can be related to totally removing EC and consequently decreasing the number of the edges which easily affect this ratio as an active defect.

To check the capability of the process in printing graphene patterns with different sizes, the deposition was firstly done onto glass slides (VWR Micro Slides) with different injection parameters at substrate temperature of 80˚C during printing. It was concluded that the aerosol-jet set up is capable of printing fine patterns with the width of 8 to 45 (µm) which are the finest printed graphene interconnects. After the deposition process, to achieve the pure graphene patterns, the samples were annealed at 250ºC and 400ºC to compare the properties of graphene/EC and pure graphene patterns, respectively. A hot plate was simply used to anneal the samples. All the aerosol parameters ranges and the corresponding width of the resultant one layer printed patterns before and after annealing on glass substrate are listed in Table 4.3 and some of the patterns are shown in Figure 4.11. It is concluded that either higher atomizer power or atomizer flow rate can result in wider printed patterns. It is also indicated that the width of the patterns, printed on glass slide, increases up to 100% after the annealing process. It is probably due to evaporation of the solvents which causes a small displacement in the structure of patterns on glass slide and consequently a significant change in the size. It also shows that the width after annealing at both temperature levels (i.e., 250˚C and 400˚C) is the same for the most samples. So, pattern size at temperatures higher than boiling temperatures of both solvents (220˚C) is probably constant and independent from temperature.

Table 4.3. Various parameters of the aerosol-jet printer in printing process of graphene ink on glass slide with deposition velocity of 0.5 mm/sec and the width of their resultant patterns before and after annealing.

Sample Number	Sheath Gas Flow rate (ccm)	Atomizer Flow Rate (ccm)	Ultrasonic Atomizer Power (V)	Width of Printed Pattern (µm)	Width after Annealing at 250˚C (µm)	Width after Annealing at 400˚C (µm)
1	35	15	50	17	20	18
2	35	17	50	17	21	21
3	35	20	48	8	14	14

4	35	20	50	30	35	35
5	45	17	50	15	16	16
6	45	20	48	8	10	10
7	45	20	50	21	24	24
8	55	15	48	23	34	34
9	55	15	50	27	50	50
10	55	17	48	30	53	53
11	55	17	50	45	70	70
12	55	20	45	8	18	18

Optical microscopy images of some of these patterns with different widths after annealing at different temperatures are shown in Figure 4.11.

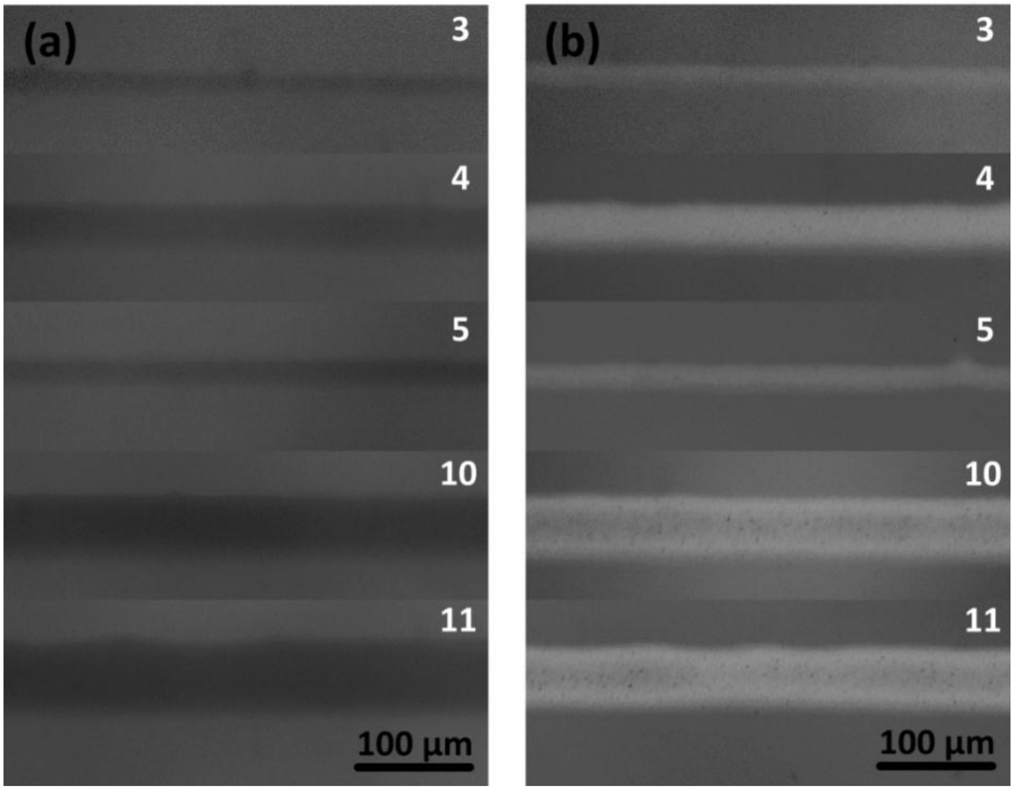

Figure 4.11. Optical microscopy images of some of the 6-layer printed graphene patterns on glass slide in different condition of aerosol-jet printing system and annealed at a) 250°C b) 400°C. Names of the samples define their printed condition listed in Table 4.3.

The comparison of the results from printing on glass slide and Si/SiO$_2$ wafers shows that surface of the substrate can significantly affect the parameters of the printing process and the resultant width of the printed patterns.

In order to measure electrical properties of the printed patterns to define their capability as interconnects, 4 points probe technique was used. Some sheets of graphene/EC with different number of the layers were printed on treated Si/SiO_2 wafers with velocity of 0.2 mm/s, 50 ccm sheath gas flow, 48 ccm atomizer flow, and 50 V atomizer power. The deposition process was followed by an annealing process on the hot plate with temperature of 250°C and 400°C to obtain graphene/EC sheets and graphene sheets, respectively. Afterwards, thickness and resistance of the sheets were measured in different parts of the sheets using AFM and 4 points probe techniques, respectively (Figure 4.12 a and b). Eventually the resistivity of the printed patterns was calculated using Van der Pauw method (Figure 4.12 c). As seen in these figures, by increasing the number of printed layers up to 15 layers, sheet resistance and resistivity of the printed structure decrease due to the higher density of connected flakes. After 15 layers printing, increasing number of the layers may not significantly affect electrical properties of printed interconnect. It indicates that saturation of the connected flakes occurs by 15 layers printing. So 15 layers is considered as the optimum number of the layers which can result in minimum sheet resistance (0.93 kΩ/□ for graphene/EC and 1.64 kΩ/□ for pure graphene) and resistivity (0.012 Ω.cm for graphene/EC and 0.018 Ω.cm for pure graphene) after annealing (at 250°C and 400°C, respectively). It seems that the existence of decomposed EC in the graphene/EC printed patterns, which are annealed at 250°C, can increase connection between graphene flakes and consequently decrease resistivity of the patterns compare to pure graphene patterns those are annealed at 400 °C. Although the minimum achieved resistivity is more than those reported in Secor et al.'s work [14] and Su et al.'s work [125], significant improvement in resistivity and sheet resistance is achieved compared to the previous reported printed graphene-based patterns [15, 126-128]. Obtained sheet resistance and resistivity shows high ability of the aerosol-jet printing process to create graphene interconnects or sheets to use in different kinds of electronic devices such as micro-supercapacitors, thin film transistors, and transparent conductive thin films [15]. The adaption of the introduced printing procedure of graphene in the mentioned devices is under study.

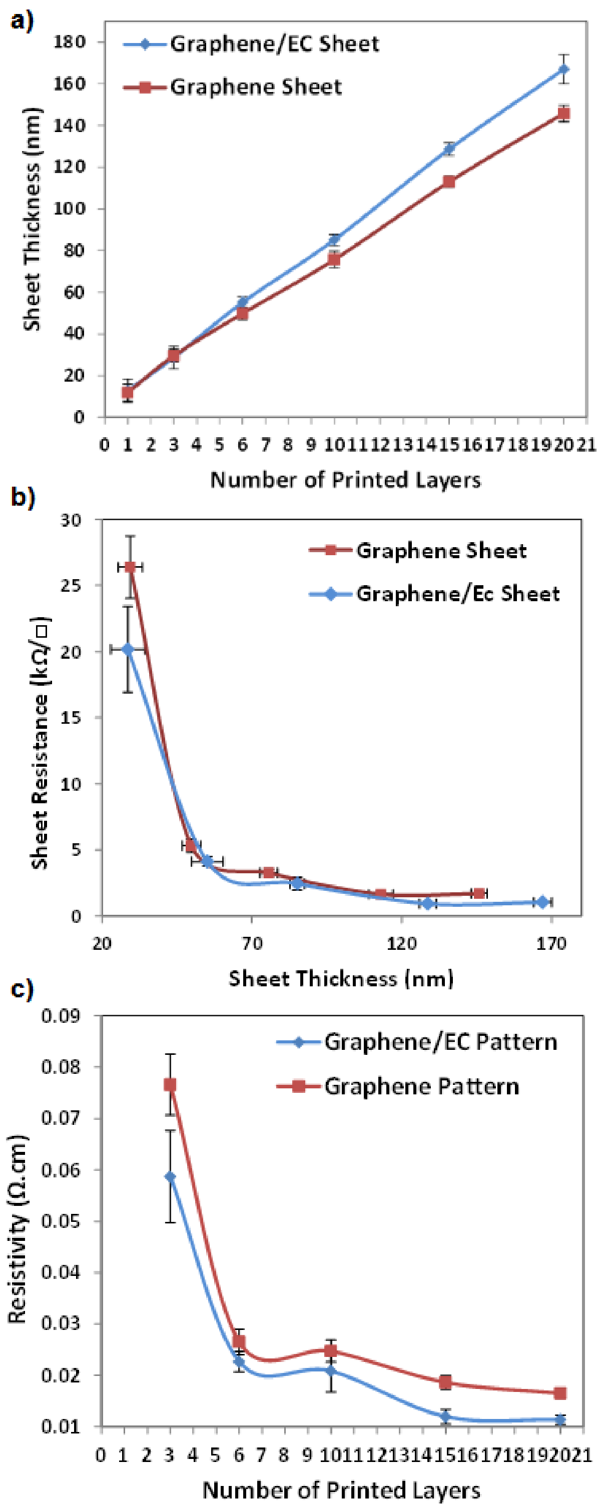

Figure 4.12. Electrical and geometrical characteristics of the graphene and graphene/EC printed interconnects; a) sheet thickness versus number of the printed layers, b) sheets resistance versus the thickness, and c) calculated resistivity of the printed sheets versus their number of the printed layers.

4.3 Summary

We have characterized an aerosol-jet printing process to produce micro-scale and conductive pure graphene patterns. A highly concentered graphene ink was prepared for this study, which contains 3.1 mg/ml exfoliated graphene flakes with lateral size below 200 nm and low degree of defects and agglomeration. Adoption of the high concentration graphene ink to the aerosol-jet printing process led to the printing of graphene patterns with controllable widths as small as 10 micron. The printed pure graphene patterns compose of fairly connected graphene flakes, and as a consequence, exhibit sheet resistance and resistivity as low as 1.64 kΩ/□ and 0.018 Ω.cm, respectively. These relatively highly conductive printed graphene patterns are the smallest printed graphene patterns to date that may provide a new printing opportunity for the development of miniaturized printed electronic applications of graphene.

Chapter 5. Laser Heat Treatment of Aerosol-Jet Additive Manufactured Graphene Interconnects[*]

In this chapter of the present thesis, a laser processing protocol for heat treatment of micro-scale printed graphene patterns is developed, and the results are compared with the counterpart results obtained by the conventional heat treatment process carried out in a furnace. A continuous-wave Erbium fiber laser is used to enhance electrical properties of the aerosol-jet printed graphene patterns through removing solvents and a stabilizer polymer. The laser power and the process speed are optimized to effectively treat the printed patterns without compromising the quality of the graphene flakes. Furthermore, a heat transfer model is developed and its results are utilized to develop the laser treatment process. It is found that the laser heat treatment process with a laser speed of 0.03 mm/s, a laser beam diameter ~50 µm, and a laser power of 10 W results in pure graphene patterns with no excessive components. The ratio of D band to G band (I_D/I_G) in Raman graph of the laser treated pure graphene, which is an indicator of the level of the active defects in graphene structure, is around 0.52. The laser treated pure graphene structure also has a *C/O* ratio, achieved from XPS results, and an electrical resistivity of ~4.5 and 0.022 Ω.cm, respectively. These values are fairly comparable with the results of samples treated in a furnace. The results suggest that the laser processing has the capability of removing stabilizer polymers and solvents through a localized moving heat source, which is preferable for flexible electronics with low working temperature substrates.

---

[*] Jabari, E., and Toyserkani, E., 2015, "Laser Heat Treatment of Aerosol-Jet Additive Manufactured Graphene Patterns," Journal of Physics D: Applied Physics, **48**(37) pp. 375503.

5.1 Experimental Procedure

5.1.1 Additive Manufacturing (Multi-layer Printing) Process

The AM process of graphene patterns by aerosol-jet printing system is explained in the previous chapter. It is also concluded from the results of the previous chapter that proper heat treatment temperature of graphene/EC composite for obtaining a graphene/EC conductive composite and pure graphene is 250°C and 400°C, respectively.

The temperature of the substrate during the deposition and laser heat treatment processes was kept around 150 °C, which resulted in printing uniform and repeatable patterns with higher quality due to improving surface energy and adhesion. Table 5.1 lists the aerosol-jet printing parameters during the deposition of the patterns with 20 layers on silicon wafers.

Table 5.1. Various parameters of the aerosol-jet printer in the printing process of graphene ink on treated Si/SiO$_2$ wafers

Microdeposition Parameters	Value
Sheath Gas Flow Rate (ccm)	50
Atomizer Flow Rate (ccm)	40 ±1
Ultrasonic Atomizer Power (V)	48
Deposition speed (mm/s)	0.1
Width of the Printed Pattern (μm)	45± 5

5.1.2 Laser Post Processing

In order to find the corresponding laser power and speed for producing the proper heat treatment condition, a heat transfer model is developed and explained in Section 5.1.2.1 and its results are used in the development of the heat treatment process as explained in Section 5.1.2.2.

5.1.2.1 Analytical Heat Transfer Modeling

Assuming one-dimensional heat flow, no convection and no exothermal process, the heat transfer behavior (from Fourier's second law) is described by the following equation [129]:

$$T_{z,t} - T_0 = \frac{2P_l\beta}{A} \left\{(\alpha t)^{1/2} ierfc\left[\frac{z}{2(\alpha t)^{1/2}}\right]\right\} \tag{5.1}$$

where T_0 is the ambient temperature, P_l laser power, β absorptivity, A the spot size area on the substrate , α thermal diffusivity, t time, z depth of heat affected zone, and the $ierfc$ is "integral of the complimentary error function".

Since the absorption of ethyl cellulose as a polymer in the infrared region is negligible [130], and the opacity of graphene is relatively adequate to absorb a reasonably good amount of light, the absorptivity of graphene is considered to govern the total absorptivity(β). Light absorption of a monolayer graphene flakes is 2.3% and its reflectance (0.1%) is negligible [131-133]. It is noted that its absorption spectra exhibits wavelength independency at wavelength higher than 800 nm [131-133]. Graphene opacity is found to increase with the number of graphene layers multiplied by a 2.3% coefficient [131-136]. In this study, a mean thickness of 2.11 nm for exfoliated graphene flakes indicates that these flakes consist of approximately 6 layers [32]. Therefore, each graphene flake (GF) has absorptivity around 0.13 ($\beta_{GF} = 0.13$).

After 20 layers printing of the graphene ink and removing all other components (i.e., solvents and ethyl cellulose) by heat treatment at 400°C on a hot plate, the thickness of remaining graphene pattern was measured by AFM. Thickness of around 140 nm shows accumulation of ~66 graphene flakes on top of each other, as:

$$Number\ of\ Graphene\ Flakes(NGF) = \frac{Mean\,Thickness\ of\ Graphene\ Pattern(TGP)}{Mean\,Thkckness\ of\ Flakes(TGF)} \tag{5.2}$$

Therefore total absorptivity of the printed pattern(β) is calculated by:

$$\beta = \beta_{GF} + \beta_{GF}(1-\beta_{GF}) + \beta_{GF}(1-\beta_{GF})(1-\beta_{GF}) + \cdots \tag{5.3}$$

Then

$$\beta = \beta_{GF} + \beta_{GF}(1-\beta_{GF}) + \beta_{GF}(1-\beta_{GF})^2 + \cdots \beta_{GF}(1-\beta_{GF})^{65}$$

$$\beta = \beta_{GF}\sum_{n=0}^{65}(1-\beta_{GF})^n$$

$$\beta = 0.99 \tag{5.4}$$

As noted, with this number of graphene flakes, the entire laser energy is absorbed. Thermal diffusivity of the printed pattern is calculated as [137]:

$$\alpha = \emptyset_G \alpha_G + \emptyset_{EC} \alpha_{EC} \qquad (5.5)$$

where $\emptyset_G$ is volume fraction of graphene, α_G thermal diffusivity of graphene, $\emptyset_{EC}$ volume fraction of EC, and α_{EC} thermal diffusivity of EC.

Knowing the composition of the prepared stabilized graphene powder which is $\sim(5\ \text{wt\%}\ \text{Graphene} + 95\ \text{wt\%}\ \text{EC})$, volume fraction of graphene is determined around 0.027. The thermal conductivity (K) of graphene strongly depends on the number of graphene layers and its contact with the substrate [138-140]. For an exfoliated single layer of graphene on SiO_2/Si, an in-plane thermal conductivity of ~600 $W\,m^{-1}K^{-1}$ is reported at room temperature. This reduced value for K compared to those of suspended graphene seems to be related to phonons leaking and scattering across the graphene–substrate interface [138]. It is also reported that the room-temperature thermal conductivity of few-layer graphene decreases by increasing the number of graphene layers [140-142]. Assuming a reduction factor of n for thermal conductivity of an n-layer graphene flake, thermal conductivity of ~100 $W\,mK^{-1}$ is considered for thermal conductivity for the GF of this study. Assuming graphite-like density and specific heat [143], calculated thermal diffusivity of 6-layer graphene flakes supported by SiO_2/Si substrate is $\sim 1.1 \times 10^{-4} m^2 s^{-1}$.

Using density, specific heat and thermal conductivity of ethyl cellulose, its thermal diffusivity is $\sim 1.4 \times 10^{-7} m^2 s^{-1}$. Therefore, using Equation (5.5) and estimated values for volume fractions and thermal diffusivities of graphene and ethyl cellulose, thermal diffusivity of the printed graphene and ethyl cellulose pattern is $\sim 3.1 \times 10^{-6} m^2 s^{-1}$.

Since the samples are on a hot plate with the temperature of 150 °C during the laser heat treatment, T_0 is considered 150°C in Equation (5.1).

Figure 5.1 shows the temperature of the printed patterns versus the laser speed with a 50 μm beam diameter at different laser powers.

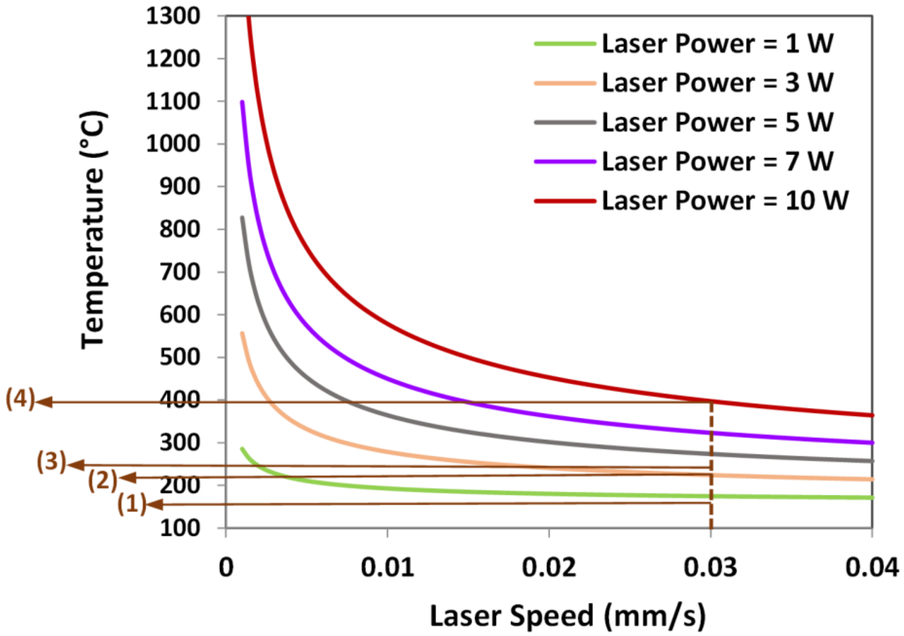

Figure 5.1. Modeling results for temperature versus laser speed during laser heat treatment with 50 µm beam diameter and different laser power. Temperatures 1, 2, 3, and 4 indicate the corresponding evaporation temperature of cyclohexanone, terpineol, first-step decomposition of EC, and removal of EC, respectively.

Given the modeling results presented in Figure 5.1, a laser speed of 0.03 mm/s is chosen for the experiments done at different laser powers to investigate the decomposition nature by increasing laser power from 1 to 10 W. Using the developed model, the temperature of the printed patterns during heat treatment with different laser powers is predicted (Figure 5.1) and listed in Table 5.2. It is expected that all solvents and stabilizer are removed at 10 W power.

Table 5.2. Temperature of the printed graphene patterns during heat treatment with different laser power and speed of 0.03 mm/s, predicted by the developed model.

Laser Power (W)	Temperature (°C)
1	175
3	225
5	273
7	322
10	396

5.1.2.2 Laser Post Processing Procedure

In LAMM setup, an aerosol-jet printing system is integrated with a 1550 nm CW fiber laser. Different parts of the system are shown in Figure 5.2. The samples were mounted under the laser beam focusing lens and moved using a moveable stage. Laser heat treatment was done using 5 different laser powers (listed in Table 5.2) and laser speed of 0.03 mm/s. The working distance of the laser beam was adjusted to ensure that the laser beam diameter was set to around 50 µm on the substrate. .

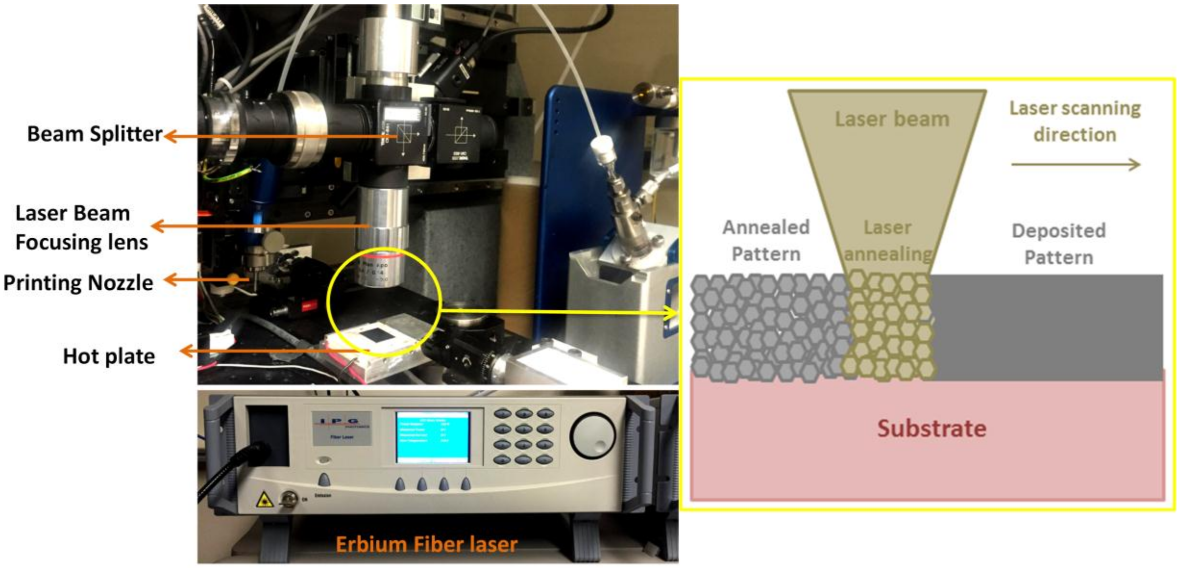

Figure 5.2. Different components of aerosol-jet AM system equipped with an Erbium laser.

5.1.3 Characterization Methods

For optical imaging of the printed patterns before and after laser heat treatment, a vision camera (EO-3112, Edmund Optics, Barrington, NJ, USA) with a zoom imaging lens (Techspec® VZM 1000I, Barrington, New Jersey, USA) was used. To closely examine the microstructure of the patterns, scanning electron microscopy (1550 FESEM, Zeiss, Oberkochen, Germany) was used. Raman spectroscopy (532 nm excitation laser, Bruker Raman Sentrerra, Bruker Optics Inc., USA) and X-ray photoelectron spectroscopy (XPS, Quantera II spectrometer, Physical Electronics (PHI), MN, USA) are also used to study the properties of heat treated graphene patterns. Atomic force microscopy (Dimension 3100 AFM, Nanoscope software, Veeco Instruments Inc., NY, USA) is also used to measure thickness of the heat treated patterns. Resistivity of the heat treated patterns was measured using a 2-point probe station (M150, Cascade Microtech®, Oregon, USA). The results of laser heat treatment method are compared with results obtained through regular heat treatment methods such as using a furnace or hot plate. To this end, a new set of patterns were printed with the same printing conditions listed in Table 5.1, and then heat treated in the furnace (1100 Box Furnace, Lindberg/Blue M, Asheville, USA) with temperatures listed in Table 5.2 and characterized using the abovementioned techniques.

5.2 Results and Discussion

The laser heat treated graphene patterns were investigated using optical microscopy and SEM. In Figure 5.3a, optical images of the printed graphene pattern with relatively uniform width of ~48 µm is shown. Figure 5.3b, c, d, and e show the graphene flakes of the laser heat treated graphene patterns with the laser powers of 1, 3, 5, and 7 W. The graphene flakes cannot be clearly observed in these figures as the laser powers were not high enough to completely remove all the solvents and EC. However, in Figure 5.3f, graphene flakes with sharp edges are easily distinguished as the extra components have been removed during the laser heat treatment with laser power of 10 W.

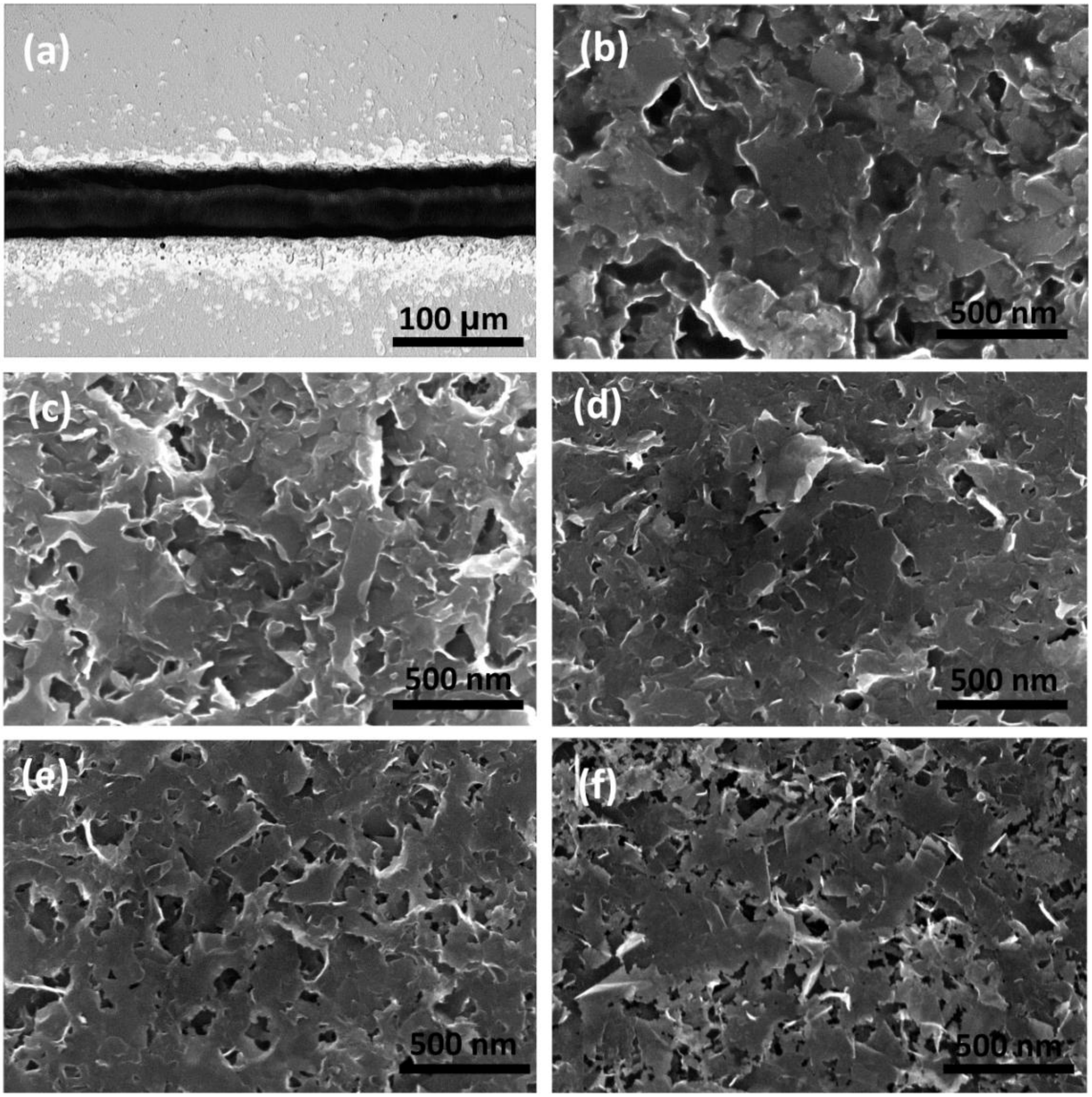

Figure 5.3. a) Optical image of as-printed graphene pattern. SEM images of laser heat-treated graphene patterns with laser power of b) 1 W, c) 3W, d) 5 W, e) 7 W, and f) 10 W.

The Raman measurements of the laser heat treated patterns with different laser powers were performed using a green laser beam (532 nm) at room temperature at an excitation rate with 20 mW incident power (Figure 5.4a). The ratio of D band intensity to G band ($\frac{I_D}{I_G}$), which is an estimation of the amount of defects in graphene structure, decreases with increasing the laser power. It can be understood as an indication of removing excess components of graphene patterns including solvents and EC polymer, which can act as an active defect and simply affect the ratio of D band to G band. It can also be due to recovery of the exfoliated and printed graphene at higher temperatures generated by the higher laser power [81]. Moreover, it is noticed that the intensity of D′ peak, which appears at ~1620 cm^{-1} and is due to the presence of the defects and the edges in graphene structure, significantly decreases with increasing the laser power. It further confirms the recovery of graphene structure and removing excess components at higher laser power. It is also observed in Figure 5.4 a that all the peaks are blue-shifted as laser power increases. Increasing the power from 1 to 10 W resulted in shifting D, G, and 2D bands to higher frequencies by 9, 2, and 8 cm^{-1}, respectively. It may be related to the thermal densification of SiO_2 [144] at higher laser power which applies a compressive stress on the relatively thin graphene patterns [81]. Increasing laser power also results in broadening D band which again shows introducing new defects in the system. In Figure 5.4b, the Raman spectrum of a fully treated pattern by laser with 10 W power is compared with the spectrum of a fully treated pattern in the furnace at a temperature of 400°C. The ratio of D to G band increased from 34% for the furnace treated sample to 52% for the laser treated one. It shows that heat treatment with laser introduces more defects into graphene structure compared to the conventional method. Furthermore, a small blue-shift of all the peaks in the laser heat treated sample compared with the furnace treated one suggests an excessive compressive stress on the graphene in the laser treated sample.

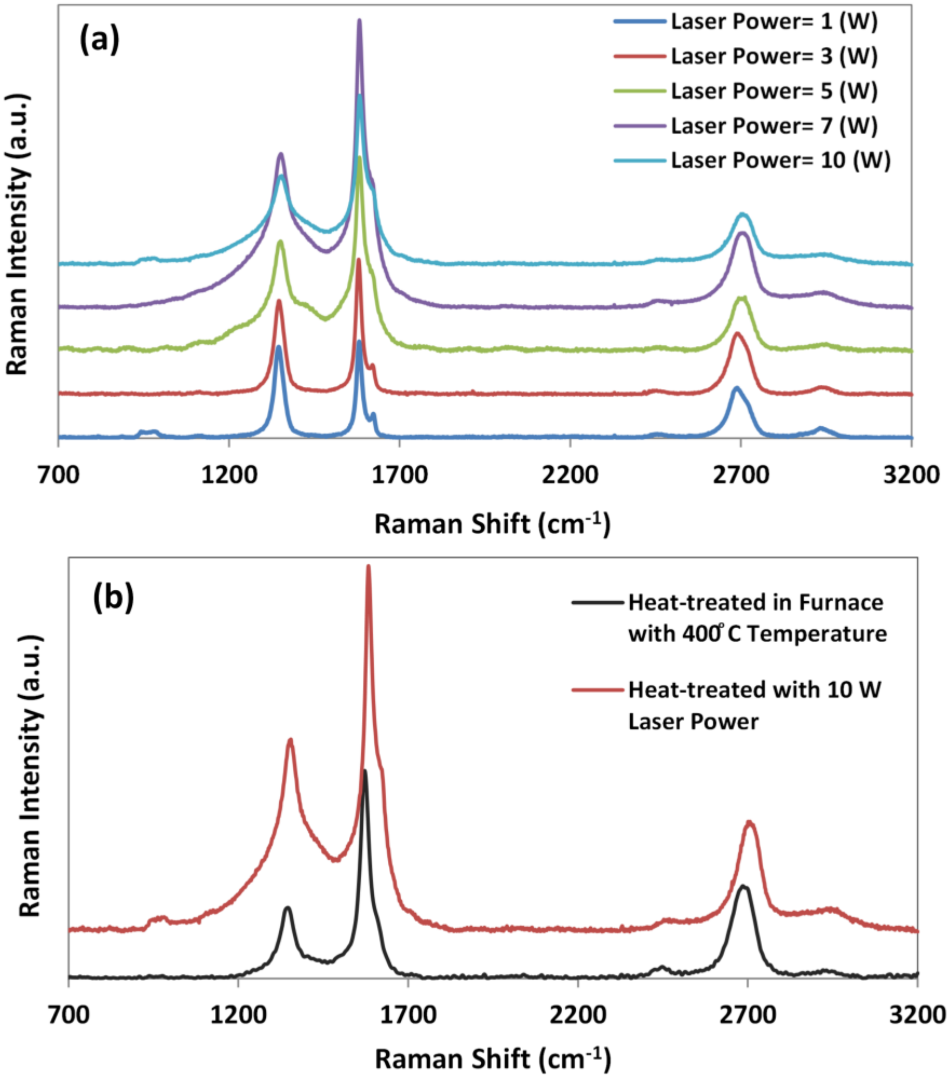

Figure 5.4. Raman spectra of a) laser heat-treated graphene patterns at different laser powers b) laser and furnace treated graphene patterns with laser power of 10 W and temperature of 400°C, respectively.

The bonding structure of fully treated pattern by 10 W laser power was also analyzed using XPS with an Al K_α X-ray (1486.7 eV) source. The XPS peaks, as marked in Figure 5.5, are attributed with sp^2 carbon bond, sp^3 carbon bond, C-OH, and C-O [32, 119-122]. Data manipulation was performed using PHI MultiPak software. The sp^2, sp^3, C-OH, and C-O bonds, are around 68%, 17%, 9%, and 6% of all the bonds, respectively. The ratio of sp^3/ sp^2 is determined to be around 0.25. This small rise in the ratio of sp^3/ sp^2 compared to that of 0.17 for the hot-plate treated graphene patterns previously reported by the authors [32], reveals that the use of the laser slightly increases the level of the defects in graphene structure compared to the conventional heat treatment processes. However, relatively high C/O ratio, around 4.5, shows that only a few percent of carbon is oxygenated. It is concluded that the laser heat treatment process results in a graphene structure with an acceptable amount of defects and oxidization.

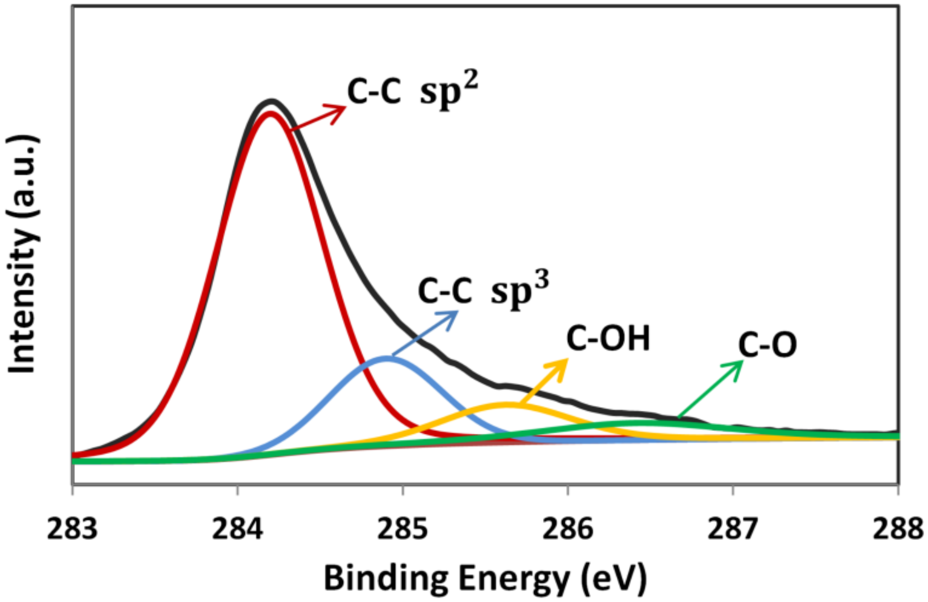

Figure 5.5. XPS spectrum of laser heat-treated graphene patterns with laser power of 10 W.

Atomic force microscopy (AFM) was done on all the laser and furnace treated patterns to measure and compare their thicknesses. All the measured thicknesses are shown in Figure 5.6 versus laser power for the laser treated patterns and the furnace temperature for the associated treated patterns. Given the standard deviation, the thicknesses of the laser treated patterns are very much matched with the value and trend of the patterns treated in the furnace with the predicted temperature calculated by the model developed in Section 5.1.2.1.

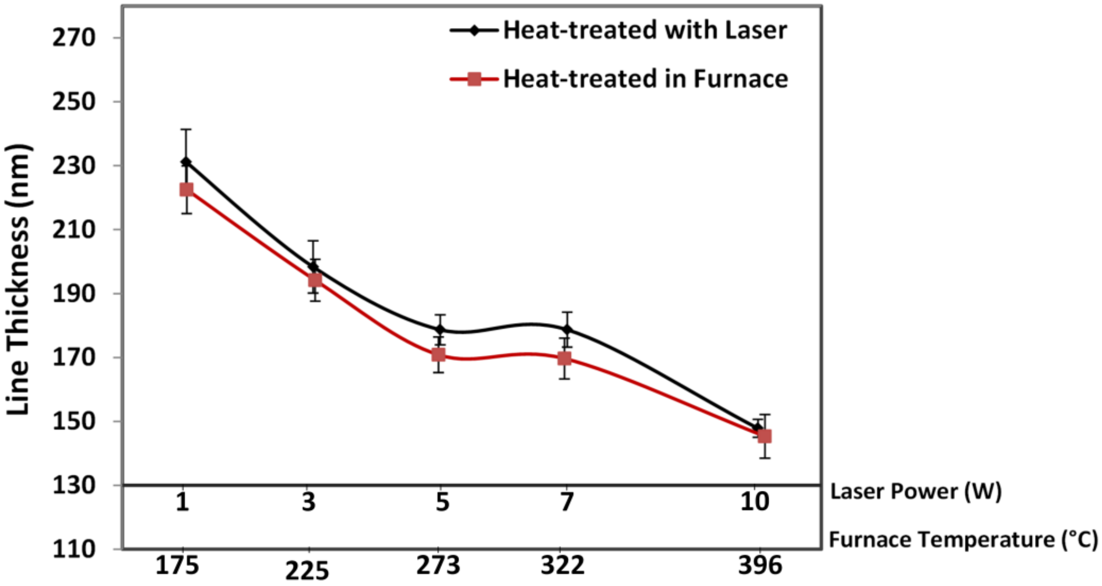

Figure 5.6. Line thickness of laser and furnace heat-treated graphene patterns versus laser power and furnace temperature, respectively.

In order to investigate the resistivity of the printed and laser treated patterns as interconnects, the resistance of the patterns was measured using 2-point probe technique. Knowing the thickness of the patterns measured by AFM, their resistivity was calculated and reported versus laser power for the laser treated patterns and also the furnace temperature for the furnace treated patterns (Figure 5.7). The graph of the resistivity of the laser treated patterns has the same trend as the graph for the patterns treated in the furnace with the predicted temperature by the developed model. The resistivity for pure graphene patterns treated with 10 W laser power is ~0.022 Ω.cm. It is fairly comparable with the resistivity of furnace treated samples (as shown in Figure 5.7) and hot plate treated patterns [32] at 400°C. The graphs also indicate that either laser treatment with laser with a power of 5 W or furnace treatment with temperature around 270°C results in even lower resistivity (around 0.015 Ω.cm) than treating with 10 W laser power or 400°C furnace temperature in the pure graphene patterns. The lower resistance is attributed to the presence of aromatic species due to the partial decomposition of EC at 250°C which can improve its electrical properties [14, 145]. The negligible increase in the resistivity of the laser treated patterns compared to the furnace treated ones is attributed to the higher level of defects and compression stress in the graphene structure which may adverse the electrical properties.

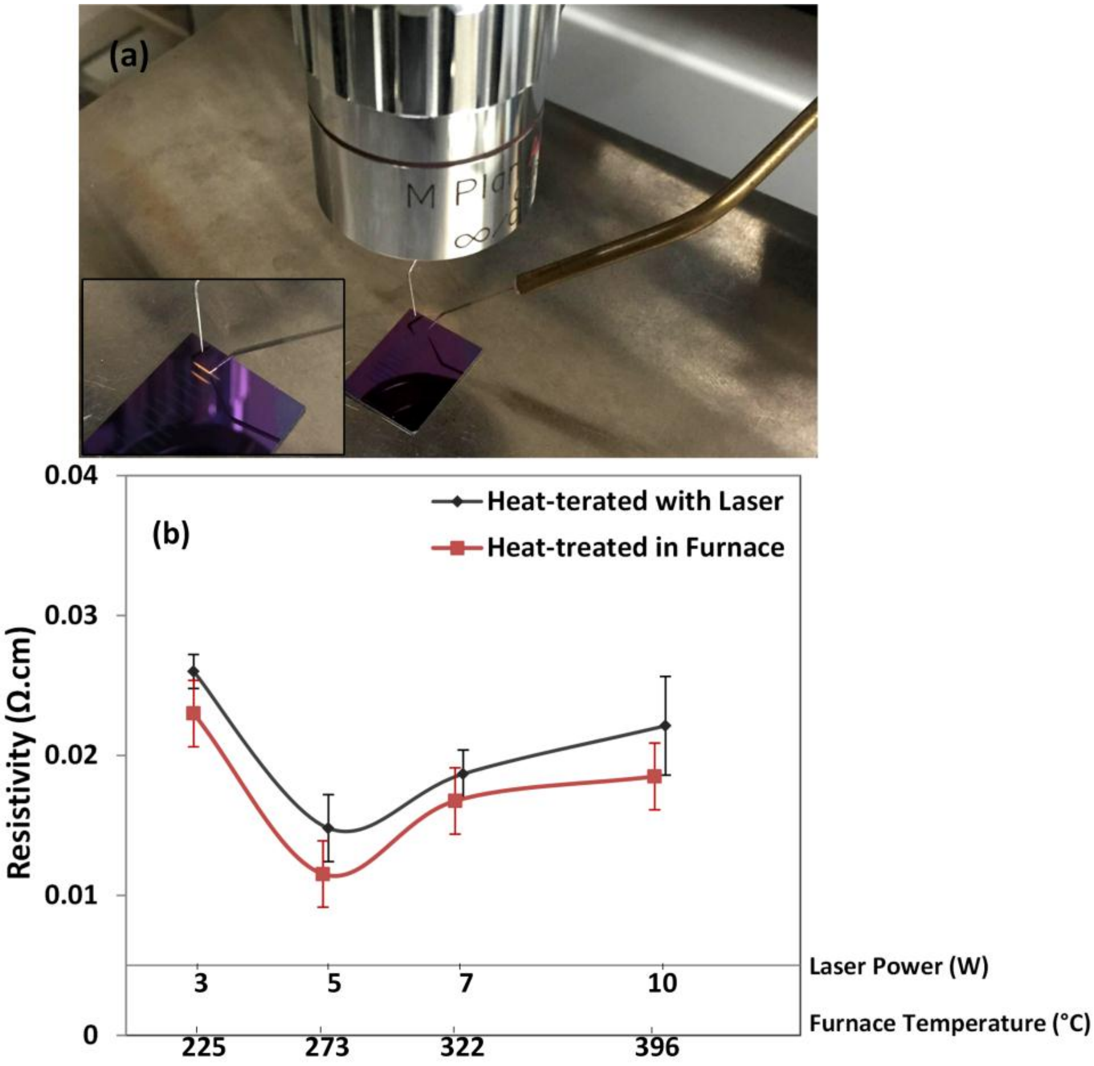

Figure 5.7. a) Resistance measurement of heat-treated patterns using 2-point probe system b) Resistivity of laser and furnace heat-treated graphene patterns versus laser power and furnace temperature, respectively.

The achieved resistivity for the laser treated graphene patterns shows the ability of the laser post processing to properly heat treat printed graphene interconnects as a localized heat treatment option.

5.3 Summary

A laser heat treatment process was characterized to efficiently treat the micro-scale aerosol-jet based additive manufactured (multi-layer printed) graphene patterns. A CW Erbium fiber laser irradiation was used as a heat source to remove the solvents and stabilizer polymer from the graphene patterns. To optimize the speed and power of the laser, a heat transfer model was developed. It was found that at the laser speed of 0.03 mm/s and a laser beam diameter of ~50 µm, the laser power of 10 W results in pure graphene patterns with no extra components. The treated graphene structure exhibits I_D/I_G and *C/O* ratios and resistivity of ~0.52, 4.5, and 0.022 Ω.cm, respectively. These values are comparable with the results obtained from the conventional heat treatment process. The laser processing can be considered as an efficient and localized process to properly heat treat printed graphene patterns.

Chapter 6. Aerosol-Jet Printing of Highly Flexible and Conductive Graphene/Silver Patterns[*]

As discussed in the previous chapters, for developing interconnecting patterns in flexible devices such as flexible touch screens [146], sensors [147], and light-emitting diodes [147], the high degree of flexibility and conductivity of graphene have made it an ideal material for use over metallic interconnects, which are subject to rigidity and crack formation [19]. The recent introduction of the use of printed graphene for this type of electronics [14, 148] has attracted industry because of the superior advantages of the associated additive manufacturing (AM) methods compared to conventional fabrication techniques: they enable the fabrication of complex designs at lower costs, greater flexibility, and a reduction in wasted material [149]. Of the AM techniques available for the fabrication of graphene electronic components, ink-based printing systems are of particular interest because of their ability to print at the microscale and their compatibility with a wide range of substrates and inks. To date, ink-jet [14, 15, 125, 127] and aerosol-jet [32] printed graphene patterns have shown promising results with respect to conductivity. Despite the potential benefits of printing graphene patterns, some challenges limit the electrical conductivity of printed graphene pattern as discussed in Chapter 1. First, despite numerous attempts to increase it, the concentration of graphene in printing inks is still quite low, primarily due to the low solubility of graphene in most solvents and the possibility of the reaggregation of the graphene flakes in highly concentrated inks. This relatively low

---

[*] Jabari, E., and Toyserkani, E., "Aerosol-Jet Printing of Highly Flexible and Conductive Graphene/Silver Patterns" Journal of Materials Letters, Submitted in November, 2015.

concentration in the inks necessitates additional printing passes to ensure the connection of the flakes in the printed patterns, thus causing the printing process to be slow and less precise. The second factor is the necessity of keeping the lateral sizes of the graphene flakes in the inks small so that they can be printed and to prevent clogging of the nozzles. This requirement results in an increased number of flake edges and random joints in the printed patterns that normally results in an increased resistivity. Printing flexible graphene interconnects whose electrical conductivity is comparable to that of metallic interconnects therefore seems to remain a challenge. It opens an avenue for the printing of a combination of graphene and conventional conductive metals that can offer the advantages of both materials. This chapter addresses the deployment of a graphene/silver nanoparticle (Ag NP) ink in an aerosol-jet additive manufacturing system in order to print highly conductive and flexible graphene/Ag patterns for flexible printed electronics. A graphene/Ag NP ink was developed using stabilized graphene powder, viscose Ag NP ink, and solvents compatible with the printing system. Printing with this ink produced a uniform microstructure and crack-free printed interconnects. With a mean resistivity of 1.07×10^{-4} Ω.cm, these interconnects are about 100 times more conductive than graphene and three times more conductive than Ag NP interconnects printed with the same printing system. Bending test results also demonstrated that the resistivity of graphene/Ag printed patterns remains consistent over up to 1000 bending cycles with a 5.5 mm radius of curvature. With their high degree of conductivity and a level of flexibility identical to that of graphene printed interconnects, graphene/Ag aerosol-jet printed interconnects may therefore be considered as an efficient candidate compared to either graphene or Ag NP printed interconnects for flexible electronics.

6.1 Experimental methods

6.1.1 Preparation and Printing of the Stable Graphene/Ag NP Ink

Producing stable inks with graphene sheets requires the graphene sheets stabilization to prevent agglomeration. The process of making stabilized graphene powder was explored in detail in Chapter 4. To print graphene patterns, a solution of 92.5 cyclohexanone: 7.5 terpineol is usually employed so that the graphene ink becomes tailored with the aerosol-jet printing process. The proper annealing temperature and time for obtaining the optimal conductivity for graphene printed patterns, as discussed in Chapter 4, are 250°C and 30 min, respectively, after which the EC is partially decomposed [32].

Printing graphene/Ag NPs requires an Ag NP solution and a concentrated solution of graphene that is compatible with the printing system. To this end, 40 mg/mL of the graphene/EC powder were dissolved in a 97.5 ethanol: 2.5 terpineol solution. The resultant dispersion was filtered using a 0.2 μm filter (0.2 μm PTFE membrane, Acrodisc® CR 25 mm syringe filter, Pall, USA) and mixed with a Cabot Ag NP solution (Cabot Superior Micro Powders, Albuquerque, USA) in a volume ratio of 1:3. The Cabot Ag NP solution contains 45 wt% to 55 wt% Ag NPs with an average particle size of 60 nm in ethylene glycol ($C_2H_4(OH)_2$) and other compatible alcohols. Based on consideration the 250°C annealing temperature required for graphene and the 180°C sintering temperature needed for Ag NPs, 250°C was chosen for annealing the graphene/Ag NP printed interconnects.

For printing Ag NP patterns, as discussed in Chapter 3, the Cabot Ag NP solution is usually diluted with deionized water in a volume ratio of 1:3. The printed patterns are sintered at 180°C for 30 min so that sinter necks are formed between the nanoparticles in order to make the patterns conductive.

Each prepared ink (graphene, graphene/Ag NPs, and Ag NPs) was placed in an aerosol-jet printing system and printed according to the individual conditions specified for each ink, as listed in Table 6.1. Six layers of each ink were additively manufactured on silicon wafers at a velocity of 0.2 mm/sec.

Table 6.1. Properties of the aerosol-jet printing system during the printing of a variety of inks on Si/SiO_2 wafers with a deposition velocity of 0.2 mm/sec.

Microdeposition Parameters	**Inks**		
	Graphene	**Ag NPs**	**Graphene/Ag NPs**
Sheath Gas Flow Rate (ccm)	50	50	50
Atomizer Flow Rate (ccm)	40 ±1	13 ±1	20 ±1
Ultrasonic Atomizer Power (V)	48	50	42
Width of the Printed Pattern (μm)	45 ±5	45 ±2	40 ±5

The printed graphene, graphene/Ag NP, and Ag NP patterns were left in the oven (1100 Box Furnace, Lindberg/Blue M, Asheville, USA) at temperatures of 250°C, 250°C, and 180°C, respectively, for 30 min in order to remove all solvents, decompose the EC, and sinter the Ag NPs.

6.1.2 Characterization of the Printed Graphene/Ag NP Interconnects

A vision camera (EO-3112, Edmund Optics, Barrington, NJ, USA) with a zoom imaging lens (Techspec® VZM 1000I, Edmund Optics, Barrington, New Jersey, USA) was utilized for imaging the patterns printed on the Si/SiO_2 wafers. For the close observation of the patterns, their microstructure was captured using a scanning electron microscope (SEM) (1550 FESEM, Zeiss, Germany). The resistance of the patterns was measured by means of a two-point probe station (M150 Measurement Platform, Cascade Microtech®, Beaverton, USA). The calculation and comparison of the resistivity of the patterns required the measurement of their thickness, which was achieved with the use of atomic force microscopy (AFM) (Dimension 3100 AFM, Nanoscope Software, Veeco Instruments Inc., Plainview, NY, USA). To assess the flexibility characteristics of the flexible printed patterns, a polyimide (Kapton, DuPont, USA) substrate was chosen. Prior to printing, the Kapton substrate was cleaned by sonication in ethanol for 20 min [14]. Five graphene and five graphene/Ag NP lines each 30 mm long were then printed using the Table 1 printing parameters. The printing process was followed by annealing in the oven at 250°C. Based on consideration of the failure rate of Ag printed patterns, which increases even further over bending cycles, these patterns were not subjected to flexibility testing. For this reason, the flexibility of the graphene/Ag NP lines was compared only to the flexibility of the graphene lines.

6.2 Results and Discussion

Figure 6.1 shows optical and SEM images of the patterns printed with the different inks: Ag NPs, graphene, and graphene/Ag NPs. The optical images of the Ag NP printed pattern show micro-cracks in the structure (Figure 6.1 (a) and 1 (b)). Closer observation of the patterns provided by the SEM image reveals agglomerated nanoparticles in the Ag NP pattern, which are most likely the source of the micro-cracks (Figure 6.1 (c)). These can lead to larger cracks and disconnections in the printed patterns, resulting in nonconductive patterns. Such patterns, which are extremely prone to cracks, are obviously unreliable candidates for flexible electronics.

In contrast, the pattern printed with graphene shows no structural cracks (Figure 6.1 (d) and 1 (e)). It also has a fairly uniform microstructure consisting of graphene flakes and partially decomposed EC (Figure 6.1 (f)). While such uniform and crack-free interconnects are ideal candidates for flexible electronics, challenges remain with respect to producing levels of conductivity as high as those obtained with printed silver interconnects [32].

The images of the graphene/Ag NP printed pattern also indicate a crack-free and uniform microstructure (Figure 6.1 (g) to 1 (i)). The source of the nonuniformity and crack formation, namely, the agglomeration of the Ag NPs, seems to be prevented by the graphene flakes. The sintered Ag NPs are evenly connected through sinter necks and are supported by the graphene flakes, which can be expected to enhance the flexibility of the pattern. To verify the accuracy of this hypothesis, further characterizations were conducted, as explained in the following paragraphs.

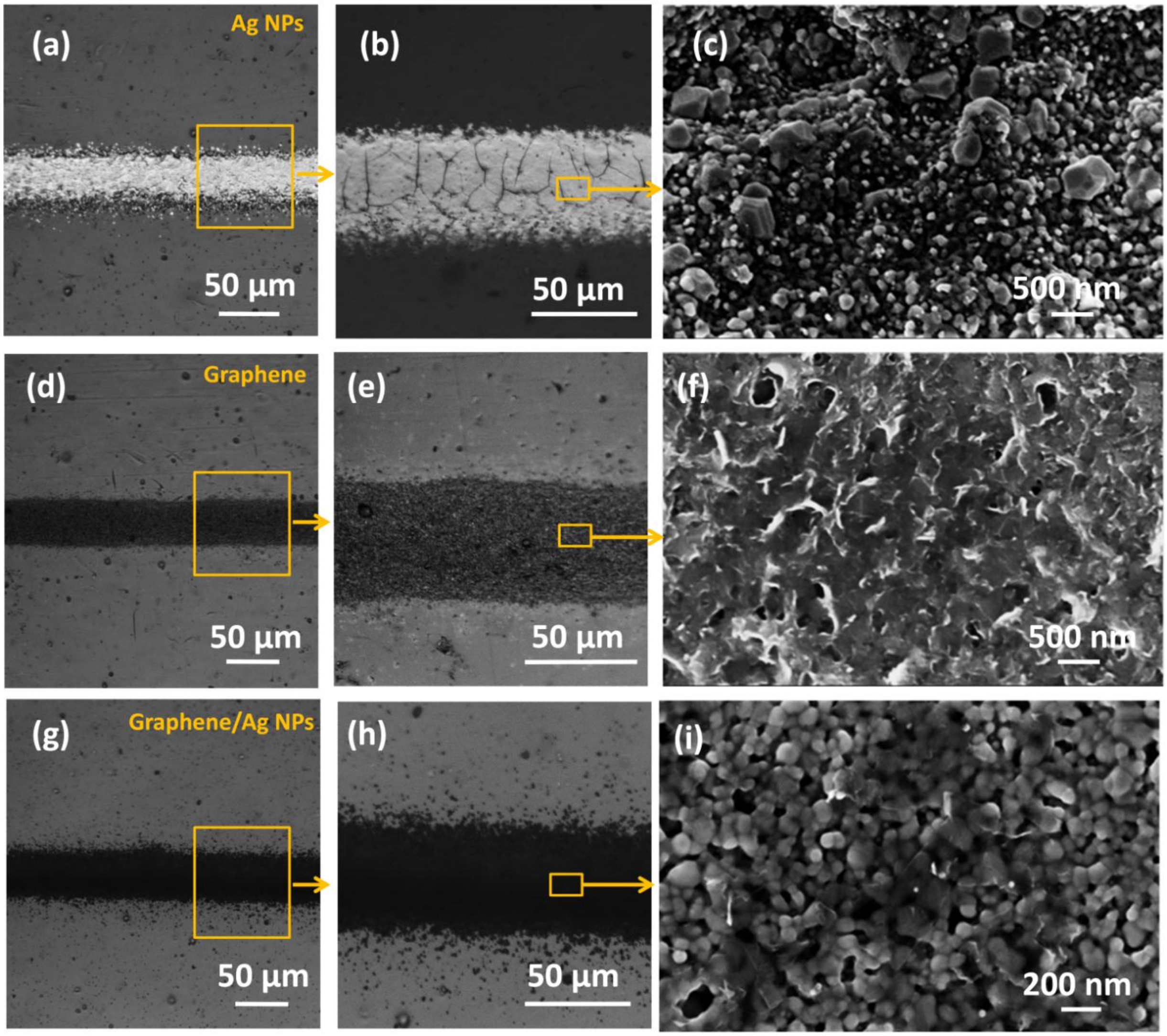

Figure 6.1. Optical images of the printed patterns: (a) and (b) Ag NPs; (d) and (e) graphene; and (g) and (h) graphene/Ag NPs. SEM images of the microstructure of the printed patterns: (c) Ag NPs; (f) graphene; and (i) graphene/Ag NPs.

To compare the resistivity of the three printed materials, five lines of each material, were printed on Si/SiO$_2$ wafers. Each line was 5 mm long, with six deposition layers. The resistance was measured using a two-point probe system with a 0.5 mm probe distance. The measurements were taken 50 times for each category in order to detect cracks that resulted in disconnections in the patterns. The rate of failure due to crack formation during the printing, sintering, or cooling processes was calculated using the number of nonconductive measurements that resulted from the 50 measurements. Resistivity was also calculated using the measured resistance and thickness of the lines. The results of all of the calculations are listed in Table 6.2.

Table 6.2. Electrical properties of graphene, graphene/Ag NP, and Ag NP printed patterns with six layers deposited on Si/SiO$_2$ wafers according to the aerosol-jet parameters listed in Table 6.1.

	Failure Rate (%)	**Mean Resistivity (Ω.cm)**
Ag NP printed interconnects	10	$(2.93 \pm 0.21) \times 10^{-4}$
Graphene printed interconnects	0	$(2.25 \pm 0.23) \times 10^{-2}$
Graphene/Ag NP printed interconnects	0	$(1.07 \pm 0.12) \times 10^{-4}$

The results suggest that the failure rate of the graphene/Ag NP printed interconnects was superior to that of the Ag NP printed interconnects. The fact that the graphene/Ag NP printed interconnects exhibited no failure rate as the graphene interconnects reveals that the mechanical properties of the patterns was enhanced by the presence of the graphene flakes in the microstructure of the graphene/Ag NP patterns. In addition, the calculated resistivity of the combination patterns is not only 100 times less than the resistivity of the graphene patterns, but also about three times less than that of the Ag NP printed patterns. The graphene sheets seem to act as a bridge between the Ag NPs that facilitates the movement of the electrons [41]. The Ag NPs also bridge the graphene flakes and reduce their contact resistivity, thus decreasing the resistivity of the printed pattern [150].

To assess the flexibility of the graphene/Ag NP printed lines, a flexibility test was conducted on the lines printed on the polyimide substrate. The printed interconnects were subjected to bending over a tube, with a 5.5 mm radius of curvature and up to 1000 bending cycles. The normalized resistance (the resistance of the patterns after bending over their initial resistance) is calculated and results are illustrated in Figure 6.2.

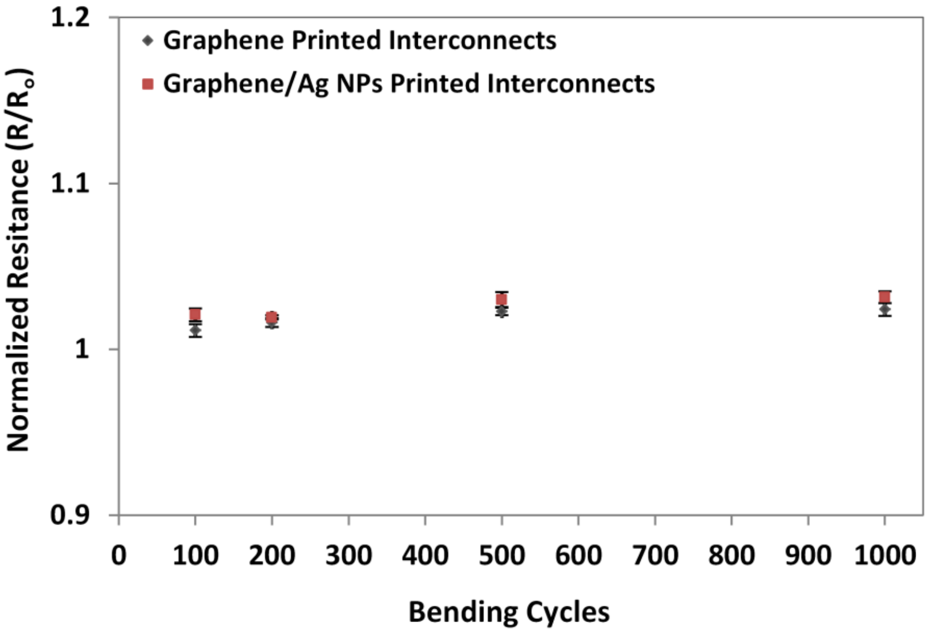

Figure 6.2. Changes in the resistance of the 30 mm printed patterns on Kapton as a function of the number of bending cycles with a 5.5 mm radius of curvature.

Figure 6.2 demonstrates that the resistance of the graphene and graphene/Ag NP printed patterns remains relatively constant over the bending cycles. It can be concluded that the addition of intrinsically robust graphene sheets to Ag NPs forms a three-dimensional network that can enhance the mechanical robustness of the printed patterns [39, 40, 150]. It was also concluded from the SEM images (Figure 6.1) that the graphene flakes also act as a kind of stabilizer for the Ag NPs and prevent the agglomeration of the nanoparticles. Crack formation resulting from agglomerated particles is therefore less likely to occur, and the tracks consequently exhibit a decreased failure rate (Table 6.2) as well as increased flexibility (Figure 6.2).

6.3 Summary

In conclusion, we have successfully printed highly conductive and fairly flexible graphene/Ag NP interconnects using an aerosol-jet printing system. Adding graphene flakes to the Ag NP ink resulted in a uniform microstructure and crack-free printed patterns. With a mean resistivity of 1.07×10^{-4} Ω.cm, these interconnects are about 100 times more conductive than graphene interconnects and three times more conductive than Ag NP interconnects printed with the same printing system. The mechanical tests also revealed that graphene/Ag NP printed interconnects have the same degree of flexibility as graphene printed interconnects. The high levels of conductivity and flexibility that characterize graphene/Ag NP printed interconnects therefore make them more efficient candidates than graphene or Ag NP printed interconnects for advancing the quest to enhance flexible electronics.

Chapter 7. Conclusions and Future Work

7.1 Summary

The focus of this dissertation was on the development of micro-scale additively manufactured highly flexible patterns. Rigidity and crack formation issues in Ag NP additively manufactured interconnect raised an interest to replace Ag NPs with an electrically conductive material with better mechanical properties. To this end, graphene was chosen and a micro-scale aerosol-jet additive manufacturing technology was deployed and characterized to print conductive and flexible graphene-based interconnects. A highly concentrated graphene ink was developed and adopted for the aerosol-jet printing process to make a reliable and repeatable graphene deposition. A laser processing protocol as a localized heat treatment process for the printed graphene patterns, which is preferable for flexible electronics with low working temperature substrates, was also developed. For this purpose, a continuous-wave Erbium fiber laser was used to enhance electrical properties of the aerosol-jet printed graphene patterns through removing solvents and a stabilizer polymer. The laser power and the process speed were optimized to effectively treat the printed patterns without compromising the quality of the graphene flakes. This thesis also addressed the development and deployment of a graphene/silver nanoparticle ink in the aerosol-jet additive manufacturing system in order to print highly conductive and flexible graphene/Ag patterns for flexible printed electronics. The specific conclusions of the present thesis are given in the following section.

7.2 Thesis Conclusions

The following conclusions can be drawn from this thesis:

1. The aerosol-jet AM system can effectively be deployed to print non-planar interconnects between the two layers of copper in a double-sided copper substrate separated by a layer of PET. Although feasible, the process was extremely sensitive to the variation of process parameters.
2. Laser sintering of the non-planar aerosol-jet printed Ag NP interconnects with 1.24 W laser power resulted in conductive interconnects with ~3.2 Ω resistance. A 3D thermal-structural interaction finite element model was developed to simulate the sintering process. The numerical and experimental results suggested that the local temperature around 580 K, which is obtained at 1.24 W laser power, may suffice for the sintering of Ag nanoparticles. The model also predicted that the maximum strain occurs around the Cu/PET interface that may cause cracks formation at this area as observed in the experimental samples.
3. To print graphene interconnects, as the more flexible interconnects compared to Ag NP interconnects, and to attain desired properties from the printed patterns created by the less number of the printed layers, a highly concentrated graphene ink was developed that includes cyclohexanone and terpineol as solvents. This ink contained 3.1 mg/ml exfoliated graphene flakes with lateral size below 200 nm and low degree of defects and agglomeration.
4. The adoption of the high concentration graphene ink to the aerosol-jet printing process led to the printing of graphene patterns with controllable widths as small as 10 micron. The printed pure graphene patterns were composed of fairly connected graphene flakes, and as a consequence, exhibited sheet resistance and resistivity as low as 1.64 kΩ/□ and 0.018 Ω.cm, respectively. These relatively highly conductive printed graphene patterns were the smallest printed graphene patterns to date that may provide a new printing opportunity for the development of miniaturized printed electronic applications of graphene.
5. A laser heat treatment process was established to locally treat the micro-scale aerosol-jet printed graphene patterns. A CW Erbium fiber laser irradiation was used as a heat source

to remove the solvents and stabilizer polymer from the graphene patterns. To optimize the speed and power of the laser, a heat transfer model was developed. The numerical and experimental results showed that at the laser speed of 0.03 mm/s and a laser beam diameter of ~50 µm, the laser power of 10 W resulted in pure graphene patterns with properties comparable with the counterpart results obtained by the conventional heat treatment process. It was concluded that the laser processing can be considered as an efficient and localized process to properly heat treat printed graphene patterns without negatively affect the graphene flakes and the flexible substrate.

6. A graphene/Ag NP ink was developed using stabilized graphene powder, viscose Ag NP ink, and solvents compatible with the printing process. The deployment of the graphene/Ag NP ink in the aerosol-jet printing process resulted in printing highly conductive and fairly flexible graphene/Ag NP interconnects. The high levels of conductivity and flexibility of the graphene/Ag NP printed interconnects made them more efficient candidates than graphene or Ag NP printed interconnects for use in flexible electronics.

7.3 Recommendations and Future Work

The investigations described in this dissertation are intended to establish the framework for the fabrication of highly conductive and flexible graphene-based patterns using a micro-scale additive manufacturing system. Further investigation should be performed to enhance the properties of the final parts, speed up the entire of the process, and broaden the range of the applications. The following recommendations for future work can further help to achieve the mentioned goals. These recommendations are categorized in three different groups as followings.

7.3.1 Materials Development

The following future work can be done to improve the properties of the developed materials and their development procedures:

1. The first recommendation is about developing more suitable graphene composite powder for flexible electronic applications. In the process of making the highly concentrated graphene ink, explored in details in Chapter 4, EC was used as a stabilizer polymer to prevent agglomeration of the graphene flakes in the ink. A graphene/EC composite

powder was prepared and dissolved in the solvents to make the printing ink. As the TGA results show, first step decomposition temperature of EC is around 250 and complete decomposition occurs at temperatures above 400°C. These elevated temperatures may not be suitable for flexible substrates and may also introduce some defects into graphene flakes and consequently affect electrical properties of printed graphene. So, replacing EC by a stabilizer polymer which has less decomposition temperature may be helpful to use printed graphene in printed electronics.

2. Increasing the graphene content in the composite powder is also recommended to reduce required printing passes for specific properties. Higher graphene content in the powder will increase concentration of the ink and decrease the required printing layers and consequently result in more precise printing process. For this purpose, the step of removing excess EC during preparing the powder should be improved to be able to remove all the excess EC and increase the graphene content in the powder.
3. The development of more suitable graphene composite powder for realizing 3D structure of the printed graphene patterns is also recommended. For this purpose, it is necessary to increase graphene content in the composite powder by the way described above.

7.3.2 Additive Manufacturing Process

As described in details in the previous chapters, graphene inks suffer from low concentration due to the low solubility of graphene in most solvents and the possibility of the reaggregation of the graphene flakes in highly concentrated inks. Using the stabilized graphene flakes has solved this problem to some extent. But the stabilizer polymer increases the viscosity of the highly concentrated graphene inks which are necessary for realization of 3D printed structures. So, extrusion-based additive manufacturing processes can be more efficient in printing 3D structures of graphene. Therefore, the development of a kind of micro-scale extrusion-based additive manufacturing process is recommended to fabricate micro-scale 3D structures of printed graphene.

7.3.3 Post Heat Treatment Process

As described in Chapter 5, localized and fast laser-based heat treatment processes are preferred as the necessary heat treatment processes after printing step. In Chapter 5, a thermal model was developed. The development of a comprehensive thermal-structural model for printing graphene patterns on flexible substrate is recommended. It can anticipate the exact laser power and laser speed to achieve require electrical and mechanical properties of the printed graphene without negatively affect the graphene flakes and the flexible substrate.

References

[1] Ivanova, O. S., Williams, C. B., and Campbell, T. A., 2011, "Additive Manufacturing (AM) and Nanotechnology: Promises and Challenges," The 22nd International SFF Symposium—An Additive Manufacturing Conference, Anonymous pp. 8-10.

[2] Kim, R., Bae, M., Kim, D. G., 2011, "Stretchable, Transparent Graphene Interconnects for Arrays of Microscale Inorganic Light Emitting Diodes on Rubber Substrates," Nano Letters, **11**(9) pp. 3881-3886.

[3] Goosey, M., 2012, "A Short Introduction to Graphene and its Potential Interconnect Applications," Circuit World, **38**(2) pp. 83-86.

[4] Park, S., Yun, J. M., Maiti, U. N., 2014, "Device-Oriented Graphene Nanopatterning by Mussel-Inspired Directed Block Copolymer Self-Assembly," Nanotechnology, **25**(1) pp. 014008.

[5] Zhang, K., Fu, Q., Pan, N., 2012, "Direct Writing of Electronic Devices on Graphene Oxide by Catalytic Scanning Probe Lithography," Nature Communications, **3**pp. 1194.

[6] Zhang, W., Zhang, Q., Zhao, M., 2013, "Direct Writing on Graphene ‘paper’by Manipulating Electrons as ‘invisible Ink’," Nanotechnology, **24**(27) pp. 275301.

[7] Vaezi, M., Seitz, H., and Yang, S., 2012, "A Review on 3D Micro-Additive Manufacturing Technologies," The International Journal of Advanced Manufacturing Technology, pp. 1-34.

[8] Le, L., Ervin, M., Qiu, H., 2011, "Inkjet-printed graphene for flexible micro-supercapacitors," Nanotechnology (IEEE-NANO), 2011 11th IEEE Conference on, Anonymous IEEE, pp. 67-71.

[9] Forrest, S. R., 2004, "The Path to Ubiquitous and Low-Cost Organic Electronic Appliances on Plastic," Nature, **428**(6986) pp. 911-918.

[10] Dua, V., Surwade, S. P., Ammu, S., 2010, "All-Organic Vapor Sensor using Inkjet-Printed Reduced Graphene Oxide," Angewandte Chemie International Edition, **49**(12) pp. 2154-2157.

[11] Le, T., Lakafosis, V., Lin, Z., 2012, "Inkjet-printed graphene-based wireless gas sensor modules," Electronic Components and Technology Conference (ECTC), 2012 IEEE 62nd, Anonymous IEEE, pp. 1003-1008.

[12] Kong, D., Le, L. T., Li, Y., 2012, "Temperature-Dependent Electrical Properties of Graphene Inkjet-Printed on Flexible Materials," Langmuir, **28**(37) pp. 13467-13472.

[13] Singh, M., Haverinen, H. M., Dhagat, P., 2010, "Inkjet Printing—process and its Applications," Advanced Materials, **22**(6) pp. 673-685.

[14] Secor, E. B., Prabhumirashi, P. L., Puntambekar, K., 2013, "Inkjet Printing of High Conductivity, Flexible Graphene Patterns," The Journal of Physical Chemistry Letters, **4**(8) pp. 1347-1351.

[15] Li, J., Ye, F., Vaziri, S., 2013, "Efficient Inkjet Printing of Graphene," Advanced Materials, **25**(29) pp. 3985-3992.

[16] Li, S., Park, J. G., Wang, S., 2014, "Working Mechanisms of Strain Sensors Utilizing Aligned Carbon Nanotube Network and Aerosol Jet Printed Electrodes," Carbon, **73**pp. 303-309.

[17] Rajan, R., and Pandit, A., 2001, "Correlations to Predict Droplet Size in Ultrasonic Atomisation," Ultrasonics, **39**(4) pp. 235-255.

[18] Bruce E. Kahn, 2007, "The M3D Aerosol Jet System, an Alternative to Inkjet Printing for Printed Electronics," Organic and Printed Electronics, **1**(2) .

[19] Jabari, E., Tong, S., Azhari, A., 2014, "Non-Planar Interconnects in Double-Sided Flexible Cu-PET Substrates using a Laser-Assisted Maskless Microdeposition Process: 3D Finite Element Modeling and Experimental Analysis," Optics and Lasers in Engineering, **54**pp. 117-127.

[20] Mir, J. M., 1980, "Cavitation-induced Capillary Waves in Ultrasonic Atomization," The Journal of the Acoustical Society of America, **67**pp. 201.

[21] Alemohammad, H., Aminfar, O., and Toyserkani, E., 2008, "Morphology and Microstructure Analysis of Nano-Silver Thin Films Deposited by Laser-Assisted Maskless Microdeposition," Journal of Micromechanics and Microengineering, **18**(11) pp. 115015.

[22] Luo, J., Jang, H. D., Sun, T., 2011, "Compression and Aggregation-Resistant Particles of Crumpled Soft Sheets," Acs Nano, **5**(11) pp. 8943-8949.

[23] Kim, S. K., Chang, H., Choi, J., 2014, "Aerosol Processing of Graphene and its Application to Oil Absorbent and Glucose Biosensor," KONA Powder and Particle Journal, **31**(0) pp. 111-125.

[24] Zang, J., Ryu, S., Pugno, N., 2013, "Multifunctionality and Control of the Crumpling and Unfolding of Large-Area Graphene," Nature Materials, **12**(4) pp. 321-325.

[25] Luo, J., Jang, H. D., and Huang, J., 2013, "Effect of Sheet Morphology on the Scalability of Graphene-Based Ultracapacitors," ACS Nano, **7**(2) pp. 1464-1471.

[26] Yan, J., Wei, T., Shao, B., 2010, "Electrochemical Properties of Graphene Nanosheet/Carbon Black Composites as Electrodes for Supercapacitors," Carbon, **48**(6) pp. 1731-1737.

[27] Wan, W., Zhao, Z., Hu, H., 2014, "Folding of Graphene into Elastic Nanobelts," Carbon, .

[28] Li, X., Cai, W., An, J., 2009, "Large-Area Synthesis of High-Quality and Uniform Graphene Films on Copper Foils," Science, **324**(5932) pp. 1312-1314.

[29] Hernandez, Y., Nicolosi, V., Lotya, M., 2008, "High-Yield Production of Graphene by Liquid-Phase Exfoliation of Graphite," Nature Nanotechnology, **3**(9) pp. 563-568.

[30] Eda, G., Fanchini, G., and Chhowalla, M., 2008, "Large-Area Ultrathin Films of Reduced Graphene Oxide as a Transparent and Flexible Electronic Material," Nature Nanotechnology, **3**(5) pp. 270-274.

[31] Lim, S., Kang, B., Kwak, D., 2012, "Inkjet-Printed Reduced Graphene Oxide/Poly (Vinyl Alcohol) Composite Electrodes for Flexible Transparent Organic Field-Effect Transistors," The Journal of Physical Chemistry C, **116**(13) pp. 7520-7525.

[32] Jabari, E., and Toyserkani, E., 2015, "Micro-Scale Aerosol-Jet Printing of Graphene Interconnects," Carbon, **91**pp. 321-329.

[33] Ni, Z. H., Wang, H. M., Luo, Z. Q., 2010, "The Effect of Vacuum Annealing on Graphene," Journal of Raman Spectroscopy, **41**(5) pp. 479-483.

[34] Ahmad, H. A., Nayak, D., and Panda, S., 2013, "Temperature Sensitivities of Doped Polyaniline Nanoscale Films on Flexible Substrates," Journal of Applied Polymer Science, **129**(1) pp. 230-237.

[35] Jabari, E., and Toyserkani, E., 2014, "Laser Post Processing of Graphene Interconnects," 33rd international Congress on Applications of Lasers & Electro-Optics (ICALEO®), Anonymous .

[36] Ma, R., Suh, D., Kim, J., 2011, "A Drastic Reduction in Silver Concentration of Metallic Ink by the use of Single-Walled Carbon Nanotubes Decorated with Silver Nanoparticles," Journal of Materials Chemistry, **21**(20) pp. 7070-7073.

[37] Oh, Y., Suh, D., Kim, Y., 2008, "Silver-Plated Carbon Nanotubes for Silver/Conducting Polymer Composites," Nanotechnology, **19**(49) pp. 495602.

[38] Ma, P. C., Tang, B. Z., and Kim, J., 2008, "Effect of CNT Decoration with Silver Nanoparticles on Electrical Conductivity of CNT-Polymer Composites," Carbon, **46**(11) pp. 1497-1505.

[39] Li, Y., Chen, Y., and Tai, N., 2013, "Fast Process to Decorate Silver Nanoparticles on Carbon Nanomaterials for Preparing High-Performance Flexible Transparent Conductive Films," Langmuir, **29**(26) pp. 8433-8439.

[40] Xu, L., Yang, G., Jing, H., 2014, "Ag–graphene Hybrid Conductive Ink for Writing Electronics," Nanotechnology, **25**(5) pp. 055201.

[41] Chen, J., Bi, H., Sun, S., 2013, "Highly Conductive and Flexible Paper of 1D Silver-Nanowire-Doped Graphene," ACS Applied Materials & Interfaces, **5**(4) pp. 1408-1413.

[42] Novoselov, K., Geim, A. K., Morozov, S., 2005, "Two-Dimensional Gas of Massless Dirac Fermions in Graphene," Nature, **438**(7065) pp. 197-200.

[43] Neto, A. C., Guinea, F., Peres, N., 2009, "The Electronic Properties of Graphene," Reviews of Modern Physics, **81**(1) pp. 109.

[44] Geim, A. K., and Novoselov, K. S., 2007, "The Rise of Graphene," Nature Materials, **6**(3) pp. 183-191.

[45] Varchon, F., Mallet, P., Magaud, L., 2008, "Rotational Disorder in Few-Layer Graphene Films on 6H-SiC (000-1): A Scanning Tunneling Microscopy Study," Physical Review B, **77**(16) pp. 165415.

[46] Charlier, J., Gonze, X., and Michenaud, J., 1994, "First-Principles Study of the Stacking Effect on the Electronic Properties of Graphite (s)," Carbon, **32**(2) pp. 289-299.

[47] Warner, J. H., Mukai, M., and Kirkland, A. I., 2012, "Atomic Structure of ABC Rhombohedral Stacked Trilayer Graphene," ACS Nano, **6**(6) pp. 5680-5686.

[48] Andrei, E. Y., Li, G., and Du, X., 2012, "Electronic Properties of Graphene: A Perspective from Scanning Tunneling Microscopy and Magneto-Transport," arXiv Preprint arXiv:1204.4532, .

[49] Choi, W., Lahiri, I., Seelaboyina, R., 2010, "Synthesis of Graphene and its Applications: A Review," Critical Reviews in Solid State and Materials Sciences, **35**(1) pp. 52-71.

[50] Barone, V., Hod, O., and Scuseria, G. E., 2006, "Electronic Structure and Stability of Semiconducting Graphene Nanoribbons," Nano Letters, **6**(12) pp. 2748-2754.

[51] Chen, S., Brown, L., Levendorf, M., 2011, "Oxidation Resistance of Graphene-Coated Cu and Cu/Ni Alloy," Acs Nano, **5**(2) pp. 1321-1327.

[52] Elias, D., Nair, R., Mohiuddin, T., 2009, "Control of Graphene's Properties by Reversible Hydrogenation: Evidence for Graphane," Science, **323**(5914) pp. 610-613.

[53] Wu, J., Pisula, W., and Müllen, K., 2007, "Graphenes as Potential Material for Electronics," Chemical Reviews, **107**(3) pp. 718-747.

[54] Boukhvalov, D., and Katsnelson, M., 2008, "Chemical Functionalization of Graphene with Defects," Nano Letters, **8**(12) pp. 4373-4379.

[55] Boukhvalov, D. W., and Katsnelson, M. I., 2009, "Enhancement of Chemical Activity in Corrugated Graphene," The Journal of Physical Chemistry C, **113**(32) pp. 14176-14178.

[56] Liu, H., Ryu, S., Chen, Z., 2009, "Photochemical Reactivity of Graphene," Journal of the American Chemical Society, **131**(47) pp. 17099-17101.

[57] Bekyarova, E., Sarkar, S., Niyogi, S., 2012, "Advances in the Chemical Modification of Epitaxial Graphene," Journal of Physics D: Applied Physics, **45**(15) pp. 154009.

[58] Zhao, Q., Nardelli, M. B., and Bernholc, J., 2002, "Ultimate Strength of Carbon Nanotubes: A Theoretical Study," Physical Review B, **65**(14) pp. 144105.

[59] Zhao, H., Min, K., and Aluru, N., 2009, "Size and Chirality Dependent Elastic Properties of Graphene Nanoribbons Under Uniaxial Tension," Nano Letters, **9**(8) pp. 3012-3015.

[60] Han, T., He, P., and Zheng, B., "DEPENDENCE OF THE TENSILE BEHAVIOR OF SINGLE GRAPHENE SHEET ON TEMPERATURE AND STRAIN RATE," .

[61] Ansari, R., Motevalli, B., Montazeri, A., 2011, "Fracture Analysis of Monolayer Graphene Sheets with Double Vacancy Defects Via MD Simulation," Solid State Communications, **151**(17) pp. 1141-1146.

[62] Pop, E., Varshney, V., and Roy, A. K., 2013, "Thermal Properties of Graphene: Fundamentals and Applications," arXiv Preprint arXiv:1301.6181, .

[63] Wei, N., Xu, L., Wang, H., 2011, "Strain Engineering of Thermal Conductivity in Graphene Sheets and Nanoribbons: A Demonstration of Magic Flexibility," Nanotechnology, **22**(10) pp. 105705.

[64] Bagri, A., Kim, S., Ruoff, R. S., 2011, "Thermal Transport Across Twin Grain Boundaries in Polycrystalline Graphene from Nonequilibrium Molecular Dynamics Simulations," Nano Letters, **11**(9) pp. 3917-3921.

[65] Geim, A. K., 2009, "Graphene: Status and Prospects," Science, **324**(5934) pp. 1530-1534.

[66] Green, A. A., and Hersam, M. C., 2009, "Emerging Methods for Producing Monodisperse Graphene Dispersions," The Journal of Physical Chemistry Letters, **1**(2) pp. 544-549.

[67] Novoselov, K. S., Geim, A. K., Morozov, S., 2004, "Electric Field Effect in Atomically Thin Carbon Films," Science, **306**(5696) pp. 666-669.

[68] Lu, X., Yu, M., Huang, H., 1999, "Tailoring Graphite with the Goal of Achieving Single Sheets," Nanotechnology, **10**(3) pp. 269.

[69] Choi, J. S., Kim, J., Byun, I., 2011, "Friction Anisotropy–driven Domain Imaging on Exfoliated Monolayer Graphene," Science, **333**(6042) pp. 607-610.

[70] Niyogi, S., Bekyarova, E., Itkis, M. E., 2006, "Solution Properties of Graphite and Graphene," Journal of the American Chemical Society, **128**(24) pp. 7720-7721.

[71] He, H., Klinowski, J., Forster, M., 1998, "A New Structural Model for Graphite Oxide," Chemical Physics Letters, **287**(1) pp. 53-56.

[72] Paredes, J., Villar-Rodil, S., Martinez-Alonso, A., 2008, "Graphene Oxide Dispersions in Organic Solvents," Langmuir, **24**(19) pp. 10560-10564.

[73] Buchsteiner, A., Lerf, A., and Pieper, J., 2006, "Water Dynamics in Graphite Oxide Investigated with Neutron Scattering," The Journal of Physical Chemistry B, **110**(45) pp. 22328-22338.

[74] Stankovich, S., Piner, R. D., Chen, X., 2006, "Stable Aqueous Dispersions of Graphitic Nanoplatelets Via the Reduction of Exfoliated Graphite Oxide in the Presence of Poly (Sodium 4-Styrenesulfonate)," Journal of Materials Chemistry, **16**(2) pp. 155-158.

[75] Li, D., Mueller, M. B., Gilje, S., 2008, "Processable Aqueous Dispersions of Graphene Nanosheets," Nature Nanotechnology, **3**(2) pp. 101-105.

[76] McAllister, M. J., Li, J., Adamson, D. H., 2007, "Single Sheet Functionalized Graphene by Oxidation and Thermal Expansion of Graphite," Chemistry of Materials, **19**(18) pp. 4396-4404.

[77] Roddaro, S., Pingue, P., Piazza, V., 2007, "The Optical Visibility of Graphene: Interference Colors of Ultrathin Graphite on SiO2," Nano Letters, **7**(9) pp. 2707-2710.

[78] Ni, Z., Wang, H., Kasim, J., 2007, "Graphene Thickness Determination using Reflection and Contrast Spectroscopy," Nano Letters, **7**(9) pp. 2758-2763.

[79] Tuinstra, F., and Koenig, J. L., 1970, "Raman Spectrum of Graphite," The Journal of Chemical Physics, **53**pp. 1126.

[80] Ferrari, A., Meyer, J., Scardaci, V., 2006, "Raman Spectrum of Graphene and Graphene Layers," Physical Review Letters, **97**(18) pp. 187401.

[81] Ni, Z., Wang, Y., Yu, T., 2008, "Raman Spectroscopy and Imaging of Graphene," Nano Research, **1**(4) pp. 273-291.

[82] Ferrari, A. C., and Basko, D. M., 2013, "Raman Spectroscopy as a Versatile Tool for Studying the Properties of Graphene," Nature Nanotechnology, **8**(4) pp. 235-246.

[83] Li, X., Magnuson, C. W., Venugopal, A., 2010, "Graphene Films with Large Domain Size by a Two-Step Chemical Vapor Deposition Process," Nano Letters, **10**(11) pp. 4328-4334.

[84] Weatherup, R. S., Bayer, B. C., Blume, R., 2011, "In Situ Characterization of Alloy Catalysts for Low-Temperature Graphene Growth," Nano Letters, **11**(10) pp. 4154-4160.

[85] Vlassiouk, I., Regmi, M., Fulvio, P., 2011, "Role of Hydrogen in Chemical Vapor Deposition Growth of Large Single-Crystal Graphene," ACS Nano, **5**(7) pp. 6069-6076.

[86] Reina, A., Jia, X., Ho, J., 2008, "Large Area, Few-Layer Graphene Films on Arbitrary Substrates by Chemical Vapor Deposition," Nano Letters, **9**(1) pp. 30-35.

[87] Meyer, J. C., Girit, C. O., Crommie, M., 2008, "Imaging and Dynamics of Light Atoms and Molecules on Graphene," Nature, **454**(7202) pp. 319-322.

[88] Lee, G., Wang, C., Yoon, E., 2010, "Reconstruction and Evaporation at Graphene Nanoribbon Edges," Physical Review B, **81**(19) pp. 195419.

[89] Huang, J. Y., Ding, F., Yakobson, B. I., 2009, "In Situ Observation of Graphene Sublimation and Multi-Layer Edge Reconstructions," Proceedings of the National Academy of Sciences, **106**(25) pp. 10103-10108.

[90] Geringer, V., Liebmann, M., Echtermeyer, T., 2009, "Intrinsic and Extrinsic Corrugation of Monolayer Graphene Deposited on SiO_ {2}," Physical Review Letters, **102**(7) pp. 076102.

[91] Shen, J., Hu, Y., Shi, M., 2009, "Fast and Facile Preparation of Graphene Oxide and Reduced Graphene Oxide Nanoplatelets," Chemistry of Materials, **21**(15) pp. 3514-3520.

[92] Lindvall, N., Kalabukhov, A., and Yurgens, A., 2012, "Cleaning Graphene using Atomic Force Microscope," Journal of Applied Physics, **111**(6) pp. 064904-064904-4.

[93] Giesbers, A., Zeitler, U., Neubeck, S., 2008, "Nanolithography and Manipulation of Graphene using an Atomic Force Microscope," Solid State Communications, **147**(9) pp. 366-369.

[94] Rakheja, S., Kumar, V., and Naeemi, A., 2013, "Evaluation of the Potential Performance of Graphene Nanoribbons as on-Chip Interconnects," Proceedings of the IEEE, **101**(7) .

[95] Sadeghi, H., Redouté, J., Lai, D. T., 2011, "A review on carbon-based materials as on-chip interconnects," Proceedings of SPIE, Anonymous **8204,** pp. 82042O.

[96] Xu, C., Li, H., and Banerjee, K., 2009, "Modeling, Analysis, and Design of Graphene Nano-Ribbon Interconnects," Electron Devices, IEEE Transactions On, **56**(8) pp. 1567-1578.

[97] Naeemi, A., and Meindl, J. D., 2009, "Compact Physics-Based Circuit Models for Graphene Nanoribbon Interconnects," Electron Devices, IEEE Transactions On, **56**(9) pp. 1822-1833.

[98] Sutter, P., Hybertsen, M., Sadowski, J., 2009, "Electronic Structure of Few-Layer Epitaxial Graphene on Ru (0001)," Nano Letters, **9**(7) pp. 2654-2660.

[99] Oostinga, J. B., Heersche, H. B., Liu, X., 2007, "Gate-Induced Insulating State in Bilayer Graphene Devices," Nature Materials, **7**(2) pp. 151-157.

[100] Gibson, I., Rosen, D.W., and Stucker, B., 2010, "Additive manufacturing technologies: rapid prototyping to direct digital manufacturing," Springer, .

[101] Swinnen, B., 2009, "3D technologies: Requiring more than 3 dimensions from concept to product," Interconnect Technology Conference, 2009. IITC 2009. IEEE International, Anonymous IEEE, pp. 59-62.

[102] O'Reilly, M., and Leal, J., 2010, "Jetting Your Way to Fine-Pitch 3D Interconnects," Chip Scale Review, **14**(5) pp. 18-21.

[103] King, B., and Renn, M., 2008, "Aerosol Jet® Direct Write Printing for Mil-Aero Electronic Applications," 2009-03-31)[2011-11-28].Http://Www.Pdfport.Com/View/63426-Aerosol-Jet-Direct-Write-Printingfor-Mil-Aero-Electronic.Html, .

[104] Lewis, J. A., and Gratson, G. M., 2004, "Direct Writing in Three Dimensions," Materials Today, **7**(7) pp. 32-39.

[105] Hedges, M., and Marin, A. B., 2012, "3D Aerosol Jet® Printing-Adding Electronics Functionality to RP/RM," DDMC 2012 Conference, Anonymous pp. 14-15.

[106] Greer, J. R., and Street, R. A., 2007, "Thermal Cure Effects on Electrical Performance of Nanoparticle Silver Inks," Acta Materialia, **55**(18) pp. 6345-6349.

[107] Font, J., Muntasell, J., and Cesari, E., 1999, "Poly (Butylene Terephthalate) Poly (Ethylene Terephthalate) Mixtures Formed by Ball Milling," Materials Research Bulletin, **34**(1) pp. 157-165.

[108] Zhang, X., Alemohammad, H., and Toyserkani, E., 2013, "Sensitivity Alteration of Fiber Bragg Grating Sensors with Additive Micro-Scale Bi-Material Coatings," Measurement Science and Technology, **24**(2) pp. 025106.

[109] Font, J., Muntasell, J., and Cesari, E., 1999, "Poly (Butylene Terephthalate) Poly (Ethylene Terephthalate) Mixtures Formed by Ball Milling," Materials Research Bulletin, **34**(1) pp. 157-165.

[110] Liang, Y. T., and Hersam, M. C., 2010, "Highly Concentrated Graphene Solutions Via Polymer Enhanced Solvent Exfoliation and Iterative Solvent Exchange," Journal of the American Chemical Society, **132**(50) pp. 17661-17663.

[111] Li, J., Ye, F., Vaziri, S., 2012, "A Simple Route Towards High-Concentration Surfactant-Free Graphene Dispersions," Carbon, **50**(8) pp. 3113-3116.

[112] Hernandez, Y., Lotya, M., Rickard, D., 2009, "Measurement of Multicomponent Solubility Parameters for Graphene Facilitates Solvent Discovery," Langmuir, **26**(5) pp. 3208-3213.

[113] Paton, K. R., Varrla, E., Backes, C., 2014, "Scalable Production of Large Quantities of Defect-Free Few-Layer Graphene by Shear Exfoliation in Liquids," Nature Materials, **13**(6) pp. 624-630.

[114] Yi, M., Shen, Z., Zhang, X., 2012, "Vessel Diameter and Liquid Height Dependent Sonication-Assisted Production of Few-Layer Graphene," Journal of Materials Science, **47**(23) pp. 8234-8244.

[115] Lafkioti, M., Krauss, B., Lohmann, T., 2010, "Graphene on a Hydrophobic Substrate: Doping Reduction and Hysteresis Suppression Under Ambient Conditions," Nano Letters, **10**(4) pp. 1149-1153.

[116] Joshi, P., Romero, H., Neal, A., 2010, "Intrinsic Doping and Gate Hysteresis in Graphene Field Effect Devices Fabricated on SiO2 Substrates," Journal of Physics: Condensed Matter, **22**(33) pp. 334214.

[117] Lohmann, T., von Klitzing, K., and Smet, J. H., 2009, "Four-Terminal Magneto-Transport in Graphene Pn Junctions Created by Spatially Selective Doping," Nano Letters, **9**(5) pp. 1973-1979.

[118] Gao, W., Alemany, L. B., Ci, L., 2009, "New Insights into the Structure and Reduction of Graphite Oxide," Nature Chemistry, **1**(5) pp. 403-408.

[119] Compagnini, G., Russo, P., Tomarchio, F., 2012, "Laser Assisted Green Synthesis of Free Standing Reduced Graphene Oxides at the Water–air Interface," Nanotechnology, **23**(50) pp. 505601.

[120] Webb, M. J., Palmgren, P., Pal, P., 2011, "A Simple Method to Produce almost Perfect Graphene on Highly Oriented Pyrolytic Graphite," Carbon, **49**(10) pp. 3242-3249.

[121] Dwivedi, N., Rismani-Yazdi, E., Yeo, R. J., 2014, "Probing the Role of an Atomically Thin SiNx Interlayer on the Structure of Ultrathin Carbon Films," Scientific Reports, **4**.

[122] Pukha, V., Zubarev, E., Drozdov, A., 2012, "Growth of Nanocomposite Films from Accelerated C60 Ions," Journal of Physics D: Applied Physics, **45**(33) pp. 335302.

[123] Kim, H., Lim, H., Kim, S., 2013, "Scalable Functionalized Graphene Nano-Platelets as Tunable Cathodes for High-Performance Lithium Rechargeable Batteries," Scientific Reports, **3**.

[124] Lee, C., Wei, X., Kysar, J. W., 2008, "Measurement of the Elastic Properties and Intrinsic Strength of Monolayer Graphene," Science (New York, N.Y.), **321**(5887) pp. 385-388.

[125] Su, Y., Du, J., Sun, D., 2013, "Reduced Graphene Oxide with a Highly Restored Π-Conjugated Structure for Inkjet Printing and its use in all-Carbon Transistors," Nano Research, **6**(11) pp. 842-852.

[126] Xu, Y., Hennig, I., Freyberg, D., 2014, "Inkjet-Printed Energy Storage Device using Graphene/Polyaniline Inks," Journal of Power Sources, **248**pp. 483-488.

[127] Finn, D. J., Lotya, M., Cunningham, G., 2014, "Inkjet Deposition of Liquid-Exfoliated Graphene and MoS 2 Nanosheets for Printed Device Applications," Journal of Materials Chemistry C, **2**(5) pp. 925-932.

[128] Shin, K., Hong, J., and Jang, J., 2011, "Flexible and Transparent Graphene Films as Acoustic Actuator Electrodes using Inkjet Printing," Chem.Commun., **47**(30) pp. 8527-8529.

[129] Steen, W.M., Mazumder, J., and Watkins, K.G., 2003, "Laser material processing," Springer, .

[130] Wells, A., 1940, "The Infra-Red Transmission of Thin Films of various Organic Materials," Journal of Applied Physics, **11**(2) pp. 137-140.

[131] Sun, Z., Yan, Z., Yao, J., 2010, "Growth of Graphene from Solid Carbon Sources," Nature, **468**(7323) pp. 549-552.

[132] Obeng, Y., De Gendt, S., SRinivasan, P., 2009, "Graphene and Emerging Materials for Post-CMOS Applications," Anonymous Electrochemical Society, .

[133] Nair, R. R., Blake, P., Grigorenko, A. N., 2008, "Fine Structure Constant Defines Visual Transparency of Graphene," Science (New York, N.Y.), **320**(5881) pp. 1308.

[134] Lee, S., Lee, K., Liu, C., 2012, "Homogeneous Bilayer Graphene Film Based Flexible Transparent Conductor," Nanoscale, **4**(2) pp. 639-644.

[135] Li, X., Zhu, Y., Cai, W., 2009, "Transfer of Large-Area Graphene Films for High-Performance Transparent Conductive Electrodes," Nano Letters, **9**(12) pp. 4359-4363.

[136] Kim, K. S., Zhao, Y., Jang, H., 2009, "Large-Scale Pattern Growth of Graphene Films for Stretchable Transparent Electrodes," Nature, **457**(7230) pp. 706-710.

[137] Progelhof, R., Throne, J., and Ruetsch, R., 1976, "Methods for Predicting the Thermal Conductivity of Composite Systems: A Review," Polymer Engineering & Science, **16**(9) pp. 615-625.

[138] Seol, J. H., Jo, I., Moore, A. L., 2010, "Two-Dimensional Phonon Transport in Supported Graphene," Science (New York, N.Y.), **328**(5975) pp. 213-216.

[139] Balandin, A. A., 2011, "Thermal Properties of Graphene and Nanostructured Carbon Materials," Nature Materials, **10**(8) pp. 569-581.

[140] Ghosh, S., Bao, W., Nika, D. L., 2010, "Dimensional Crossover of Thermal Transport in Few-Layer Graphene," Nature Materials, **9**(7) pp. 555-558.

[141] Zhong, W., Zhang, M., Ai, B., 2011, "Chirality and Thickness-Dependent Thermal Conductivity of Few-Layer Graphene: A Molecular Dynamics Study," Applied Physics Letters, **98**(11) pp. 113107.

[142] Lin, H., Xu, S., Wang, X., 2013, "Significantly Reduced Thermal Diffusivity of Free-Standing Two-Layer Graphene in Graphene Foam," Nanotechnology, **24**(41) pp. 415706.

[143] Pop, E., Varshney, V., and Roy, A. K., 2012, "Thermal Properties of Graphene: Fundamentals and Applications," MRS Bulletin, **37**(12) pp. 1273-1281.

[144] Campostrini, R., Carturan, G., Ferrari, M., 1992, "Luminescence of Eu3 Ions during Thermal Densification of SiO2 Gel," Journal of Materials Research, **7**(03) pp. 745-753.

[145] Pastorova, I., Botto, R. E., Arisz, P. W., 1994, "Cellulose Char Structure: A Combined Analytical Py-GC-MS, FTIR, and NMR Study," Carbohydrate Research, **262**(1) pp. 27-47.

[146] Zhou, L., Wanga, A., Wu, S., 2006, "All-Organic Active Matrix Flexible Display," Applied Physics Letters, **88**(8) pp. 3502.

[147] Sekitani, T., Yokota, T., Zschieschang, U., 2009, "Organic Nonvolatile Memory Transistors for Flexible Sensor Arrays," Science (New York, N.Y.), **326**(5959) pp. 1516-1519.

[148] Huang, L., Huang, Y., Liang, J., 2011, "Graphene-Based Conducting Inks for Direct Inkjet Printing of Flexible Conductive Patterns and their Applications in Electric Circuits and Chemical Sensors," Nano Research, **4**(7) pp. 675-684.

[149] Jabari, E., and Toyserkani, E., 2015, "Laser Heat Treatment of Aerosol-Jet Additive Manufactured Graphene Patterns," Journal of Physics D: Applied Physics, **48**(37) pp. 375503.

[150] Wang, G., Wang, Z., Liu, Z., 2015, "Annealed Graphene Sheets Decorated with Silver Nanoparticles for Inkjet Printing," Chemical Engineering Journal, **260**pp. 582-589.

APPENDICES

Appendix A

In the preparation of the graphene powder in Chapter 4, all the reported results are based on the exfoliation of graphite using long-time bath sonication. The multi-scale additive manufacturing laboratory became equipped with a probe sonicator (Fisher Scientific Sonic Dismembrator, Model 505, 500 W, 13 mm tip) on May 2014. All the parameters of the powder preparation procedure using this probe sonicator needed to be optimized to obtain maximum graphene content in the powder. These parameters include pulse on, pulse off, duration of the sonication, and concentration of graphite and EC in ethanol. In Table A.1 all the parameters and their resultant graphene content in the powder are listed.

Table A.1. Process parameters of the graphene powder preparation using probe sonicator.

Powder	**1**	**2**	**3**	**4**	**5**	**6**
Pulse On (s)	10	8	8	8	8	8
Pulse Off (s)	1	2	2	2	2	2
Sonication (h)	1.5	1.5	1.5	3	3	6
Ethanol (mL)	240	200	200	200	200	200
Grphite (g)	12	10	10	10	10	10
EC (g)	2.4	2	4	2	4	2
G in powder (%)	1.75	1.5	1	3	2.8	4

The parameters related to the powder 6 resulted in the highest amount of graphene in final powder and considered as the standard parameters for preparation of graphene powder using probe sonicator.

Appendix B

Matlab code for the developed model in Chapter 5 to correlate the temperature of the graphene patterns with the laser power:

```
function Temp( v ,P,D)

z=3*10^-4;
A=pi*D/4;
alpha=5.6;
beta=0.999;

T=zeros(size(P,2),size(v,2));
for j=1:size(P,2)
    for i=1:size(v,2)
        x1=z/(2*((alpha*(D/v(i)))^0.5));
        x=ierfc(x1);
        T(j,i)=150+(2*P(j)*beta/A)*(((alpha*(D/v(i)))^0.5)*x);
    end
end

    plot(v,T(1,:),v,T(2,:),v,T(3,:),v,T(4,:),v,T(5,:));
    jj=1;
end

function y = ierfc( u )


y=exp(-(u^2))/pi^1/2 -u*(1-erf(u));
end

function y=erf(u)


fun = @(x) exp(-x.^2);
y=(2/pi^0.5)*integral(fun,0,u);

end
```

Appendix C

Copyright Permissions

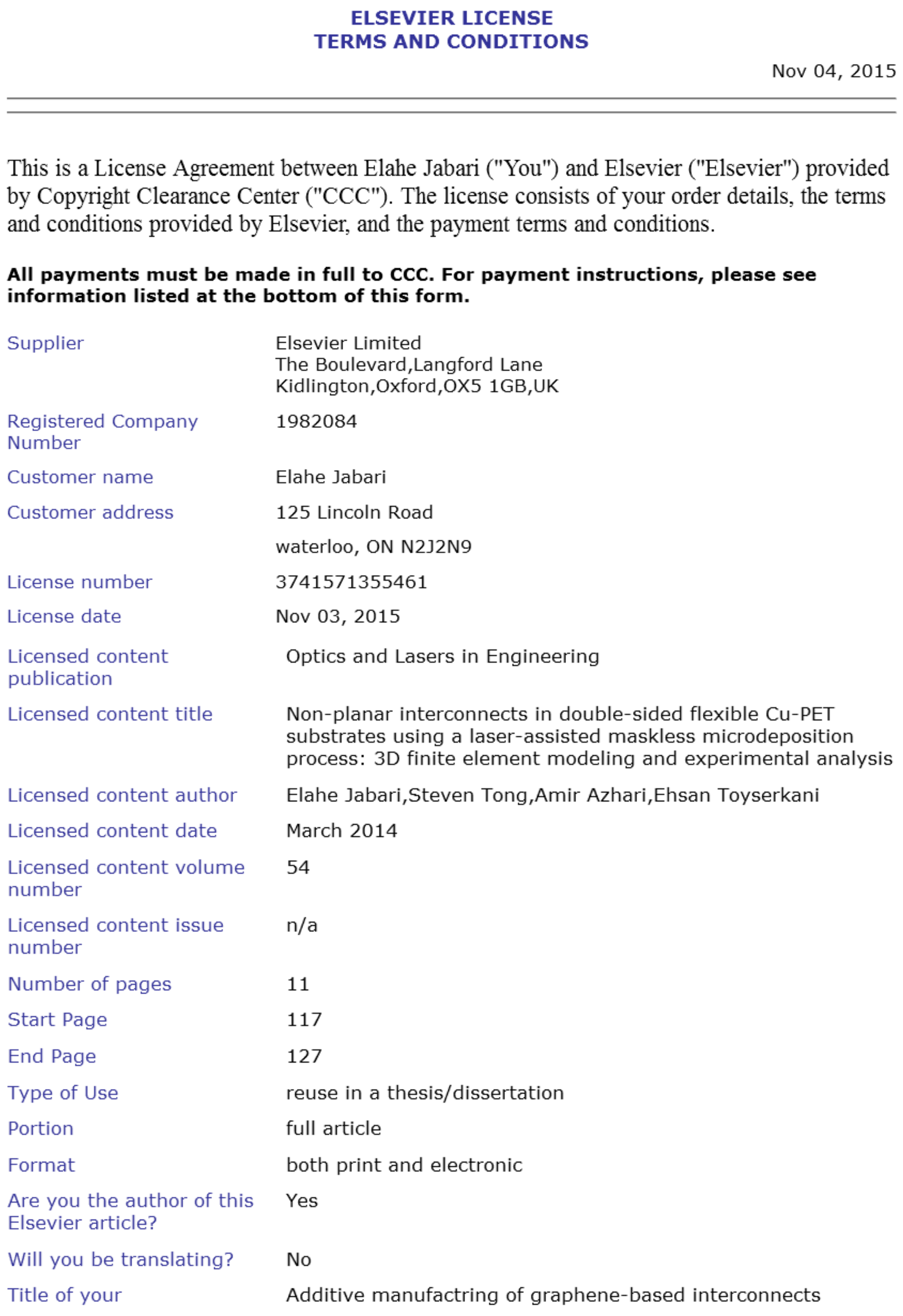

ELSEVIER LICENSE
TERMS AND CONDITIONS

Nov 04, 2015

This is a License Agreement between Elahe Jabari ("You") and Elsevier ("Elsevier") provided by Copyright Clearance Center ("CCC"). The license consists of your order details, the terms and conditions provided by Elsevier, and the payment terms and conditions.

All payments must be made in full to CCC. For payment instructions, please see information listed at the bottom of this form.

Supplier	Elsevier Limited The Boulevard,Langford Lane Kidlington,Oxford,OX5 1GB,UK
Registered Company Number	1982084
Customer name	Elahe Jabari
Customer address	125 Lincoln Road waterloo, ON N2J2N9
License number	3741571355461
License date	Nov 03, 2015
Licensed content publication	Optics and Lasers in Engineering
Licensed content title	Non-planar interconnects in double-sided flexible Cu-PET substrates using a laser-assisted maskless microdeposition process: 3D finite element modeling and experimental analysis
Licensed content author	Elahe Jabari,Steven Tong,Amir Azhari,Ehsan Toyserkani
Licensed content date	March 2014
Licensed content volume number	54
Licensed content issue number	n/a
Number of pages	11
Start Page	117
End Page	127
Type of Use	reuse in a thesis/dissertation
Portion	full article
Format	both print and electronic
Are you the author of this Elsevier article?	Yes
Will you be translating?	No
Title of your	Additive manufactring of graphene-based interconnects

Figure C.1

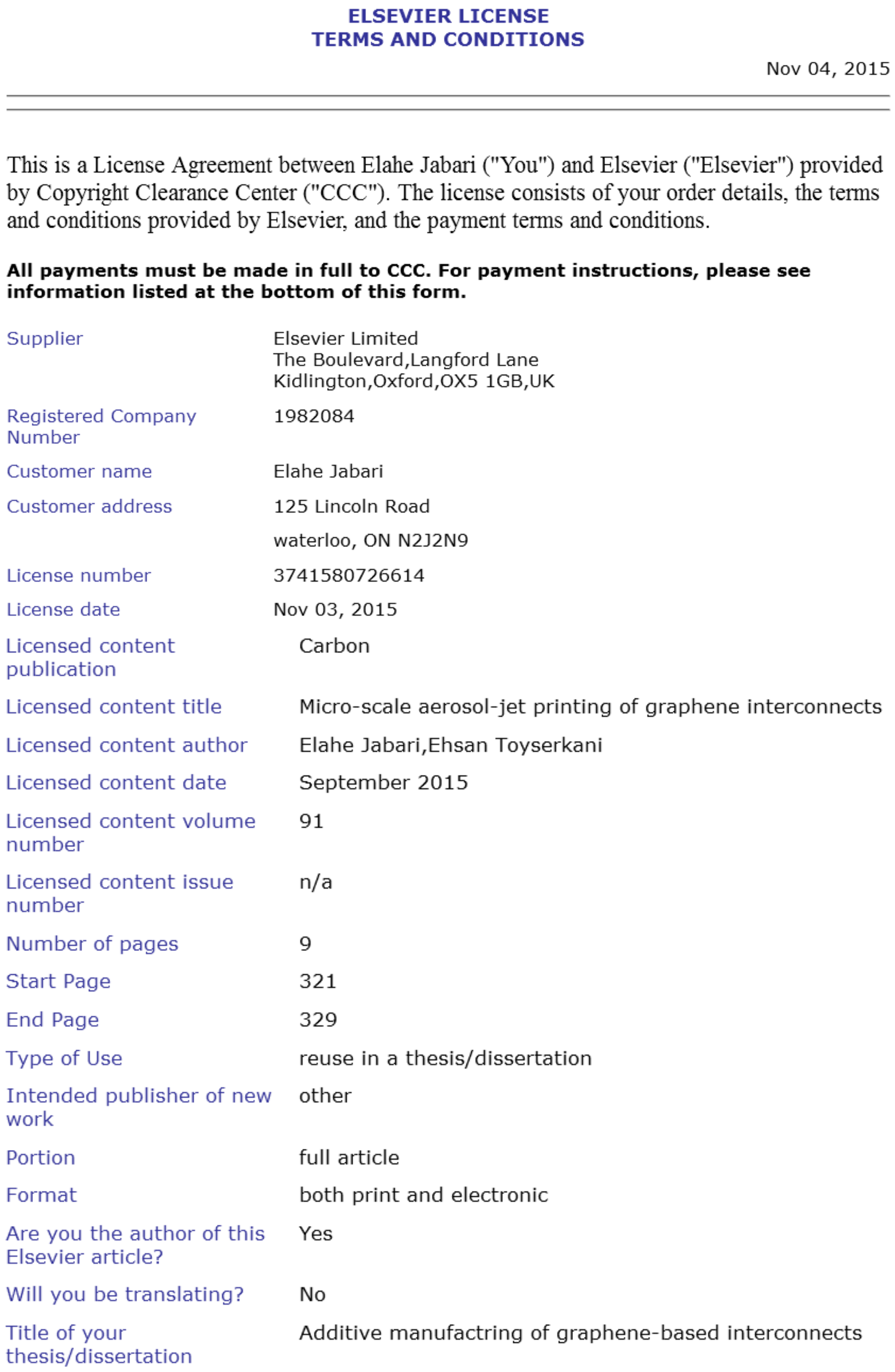

ELSEVIER LICENSE
TERMS AND CONDITIONS

Nov 04, 2015

This is a License Agreement between Elahe Jabari ("You") and Elsevier ("Elsevier") provided by Copyright Clearance Center ("CCC"). The license consists of your order details, the terms and conditions provided by Elsevier, and the payment terms and conditions.

All payments must be made in full to CCC. For payment instructions, please see information listed at the bottom of this form.

Supplier	Elsevier Limited The Boulevard,Langford Lane Kidlington,Oxford,OX5 1GB,UK
Registered Company Number	1982084
Customer name	Elahe Jabari
Customer address	125 Lincoln Road waterloo, ON N2J2N9
License number	3741580726614
License date	Nov 03, 2015
Licensed content publication	Carbon
Licensed content title	Micro-scale aerosol-jet printing of graphene interconnects
Licensed content author	Elahe Jabari,Ehsan Toyserkani
Licensed content date	September 2015
Licensed content volume number	91
Licensed content issue number	n/a
Number of pages	9
Start Page	321
End Page	329
Type of Use	reuse in a thesis/dissertation
Intended publisher of new work	other
Portion	full article
Format	both print and electronic
Are you the author of this Elsevier article?	Yes
Will you be translating?	No
Title of your thesis/dissertation	Additive manufactring of graphene-based interconnects

Figure C.2

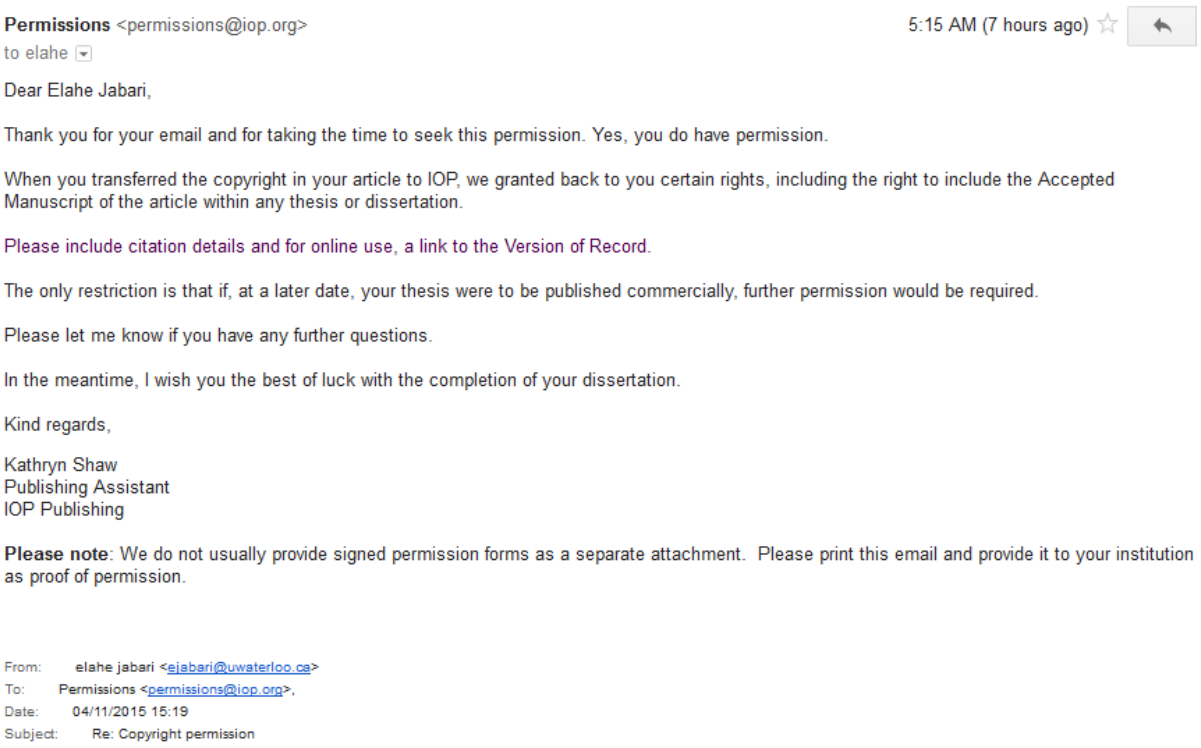
Permissions <permissions@iop.org>
to elahe

5:15 AM (7 hours ago)

Dear Elahe Jabari,

Thank you for your email and for taking the time to seek this permission. Yes, you do have permission.

When you transferred the copyright in your article to IOP, we granted back to you certain rights, including the right to include the Accepted Manuscript of the article within any thesis or dissertation.

Please include citation details and for online use, a link to the Version of Record.

The only restriction is that if, at a later date, your thesis were to be published commercially, further permission would be required.

Please let me know if you have any further questions.

In the meantime, I wish you the best of luck with the completion of your dissertation.

Kind regards,

Kathryn Shaw
Publishing Assistant
IOP Publishing

Please note: We do not usually provide signed permission forms as a separate attachment. Please print this email and provide it to your institution as proof of permission.

From: elahe jabari <ejabari@uwaterloo.ca>
To: Permissions <permissions@iop.org>,
Date: 04/11/2015 15:19
Subject: Re: Copyright permission

Figure C.3

Title: Synthesis of Graphene and Its Applications: A Review
Author: Wonbong Choi, Indranil Lahiri, Raghunandan Seelaboyina, et al
Publication: Critical Reviews in Solid State and Materials Sciences
Publisher: Taylor & Francis
Date: Feb 11, 2010
Copyright © 2010 Taylor & Francis

Logged in as:
Elahe Jabari
Account #:
3000894211

Thesis/Dissertation Reuse Request

Taylor & Francis is pleased to offer reuses of its content for a thesis or dissertation free of charge contingent on resubmission of permission request if work is published.

Copyright © 2015 Copyright Clearance Center, Inc. All Rights Reserved. Privacy statement. Terms and Conditions.
Comments? We would like to hear from you. E-mail us at customercare@copyright.com

Figure C.4

Requesting permission to reuse content from an IEEE publication

Title: Modeling, Analysis, and Design of Graphene Nano-Ribbon Interconnects

Author: Chuan Xu; Hong Li; Banerjee, K.

Publication: Electron Devices, IEEE Transactions on

Publisher: IEEE

Date: Aug. 2009

Copyright © 2009, IEEE

Logged in as:
Elahe Jabari
Account #:
3000894211

Thesis / Dissertation Reuse

The IEEE does not require individuals working on a thesis to obtain a formal reuse license, however, you may print out this statement to be used as a permission grant:

Requirements to be followed when using any portion (e.g., figure, graph, table, or textual material) of an IEEE copyrighted paper in a thesis:

1) In the case of textual material (e.g., using short quotes or referring to the work within these papers) users must give full credit to the original source (author, paper, publication) followed by the IEEE copyright line © 2011 IEEE.
2) In the case of illustrations or tabular material, we require that the copyright line © [Year of original publication] IEEE appear prominently with each reprinted figure and/or table.
3) If a substantial portion of the original paper is to be used, and if you are not the senior author, also obtain the senior author's approval.

Requirements to be followed when using an entire IEEE copyrighted paper in a thesis:

1) The following IEEE copyright/ credit notice should be placed prominently in the references: © [year of original publication] IEEE. Reprinted, with permission, from [author names, paper title, IEEE publication title, and month/year of publication]
2) Only the accepted version of an IEEE copyrighted paper can be used when posting the paper or your thesis on-line.
3) In placing the thesis on the author's university website, please display the following message in a prominent place on the website: In reference to IEEE copyrighted material which is used with permission in this thesis, the IEEE does not endorse any of [university/educational entity's name goes here]'s products or services. Internal or personal use of this material is permitted. If interested in reprinting/republishing IEEE copyrighted material for advertising or promotional purposes or for creating new collective works for resale or redistribution, please go to http://www.ieee.org/publications_standards/publications/rights/rights_link.html to learn how to obtain a License from RightsLink.

Figure C.5

Title: Graphene Thickness Determination Using Reflection and Contrast Spectroscopy

Author: Z. H. Ni, H. M. Wang, J. Kasim, et al

Publication: Nano Letters

Publisher: American Chemical Society

Date: Sep 1, 2007

Copyright © 2007, American Chemical Society

Logged in as:
Elahe Jabari
Account #:
3000894211

PERMISSION/LICENSE IS GRANTED FOR YOUR ORDER AT NO CHARGE

This type of permission/license, instead of the standard Terms & Conditions, is sent to you because no fee is being charged for your order. Please note the following:

- Permission is granted for your request in both print and electronic formats, and translations.
- If figures and/or tables were requested, they may be adapted or used in part.
- Please print this page for your records and send a copy of it to your publisher/graduate school.
- Appropriate credit for the requested material should be given as follows: "Reprinted (adapted) with permission from (COMPLETE REFERENCE CITATION). Copyright (YEAR) American Chemical Society." Insert appropriate information in place of the capitalized words.
- One-time permission is granted only for the use specified in your request. No additional uses are granted (such as derivative works or other editions). For any other uses, please submit a new request.

If credit is given to another source for the material you requested, permission must be obtained from that source.

Figure C.6

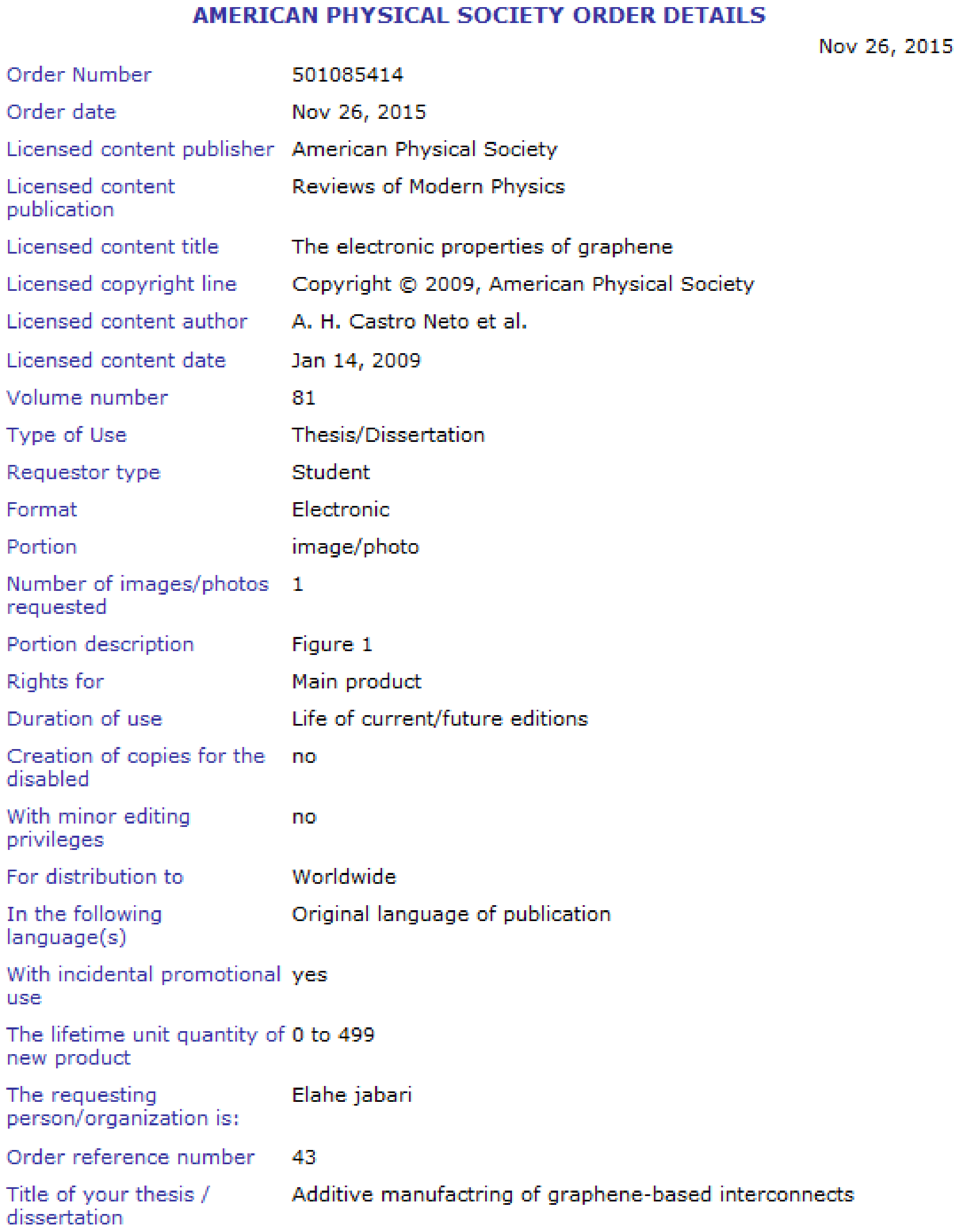

AMERICAN PHYSICAL SOCIETY ORDER DETAILS

Nov 26, 2015

Order Number	501085414
Order date	Nov 26, 2015
Licensed content publisher	American Physical Society
Licensed content publication	Reviews of Modern Physics
Licensed content title	The electronic properties of graphene
Licensed copyright line	Copyright © 2009, American Physical Society
Licensed content author	A. H. Castro Neto et al.
Licensed content date	Jan 14, 2009
Volume number	81
Type of Use	Thesis/Dissertation
Requestor type	Student
Format	Electronic
Portion	image/photo
Number of images/photos requested	1
Portion description	Figure 1
Rights for	Main product
Duration of use	Life of current/future editions
Creation of copies for the disabled	no
With minor editing privileges	no
For distribution to	Worldwide
In the following language(s)	Original language of publication
With incidental promotional use	yes
The lifetime unit quantity of new product	0 to 499
The requesting person/organization is:	Elahe jabari
Order reference number	43
Title of your thesis / dissertation	Additive manufactring of graphene-based interconnects

Figure C.7

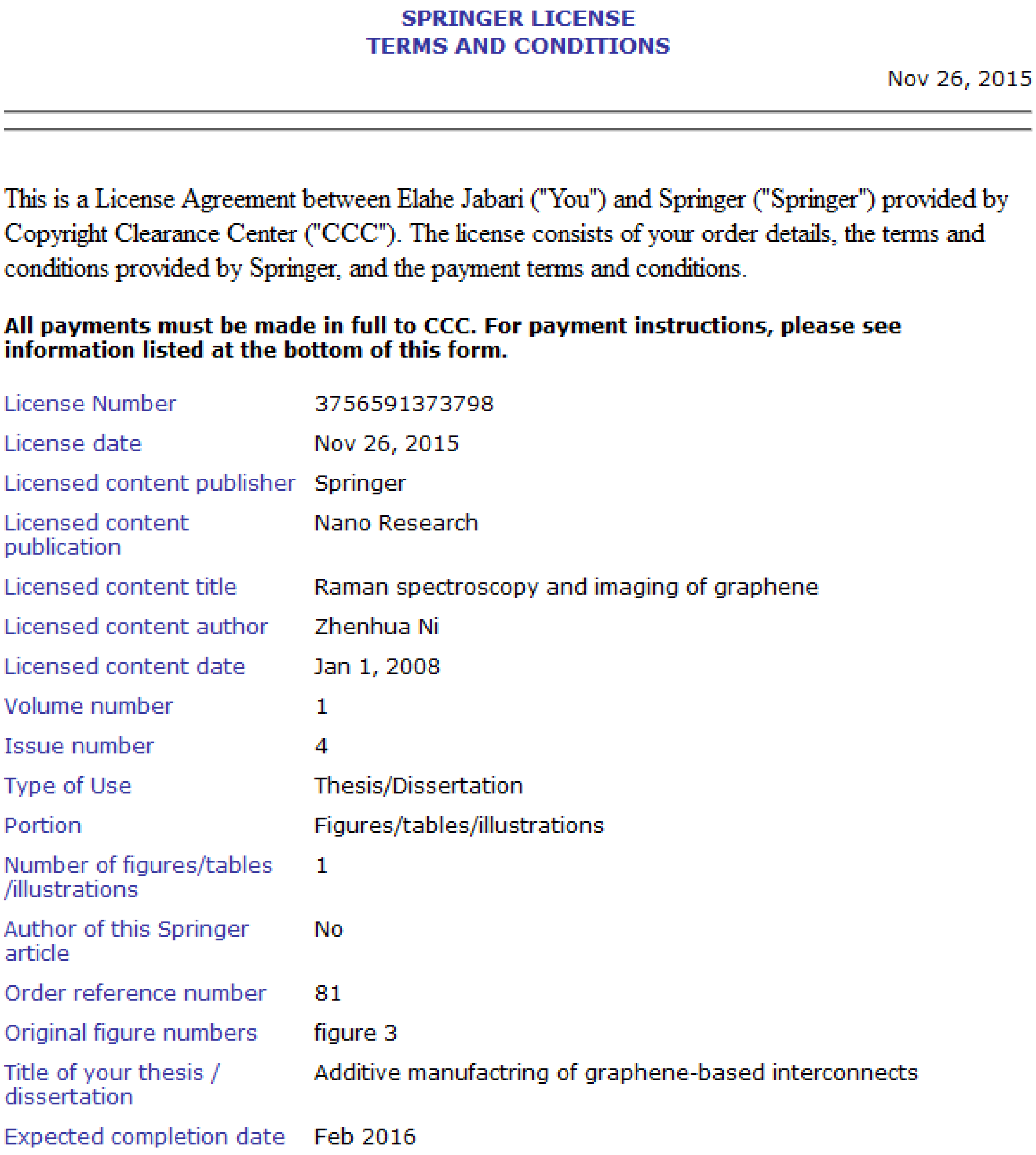

SPRINGER LICENSE
TERMS AND CONDITIONS

Nov 26, 2015

This is a License Agreement between Elahe Jabari ("You") and Springer ("Springer") provided by Copyright Clearance Center ("CCC"). The license consists of your order details, the terms and conditions provided by Springer, and the payment terms and conditions.

All payments must be made in full to CCC. For payment instructions, please see information listed at the bottom of this form.

License Number	3756591373798
License date	Nov 26, 2015
Licensed content publisher	Springer
Licensed content publication	Nano Research
Licensed content title	Raman spectroscopy and imaging of graphene
Licensed content author	Zhenhua Ni
Licensed content date	Jan 1, 2008
Volume number	1
Issue number	4
Type of Use	Thesis/Dissertation
Portion	Figures/tables/illustrations
Number of figures/tables /illustrations	1
Author of this Springer article	No
Order reference number	81
Original figure numbers	figure 3
Title of your thesis / dissertation	Additive manufactring of graphene-based interconnects
Expected completion date	Feb 2016

Figure C.8

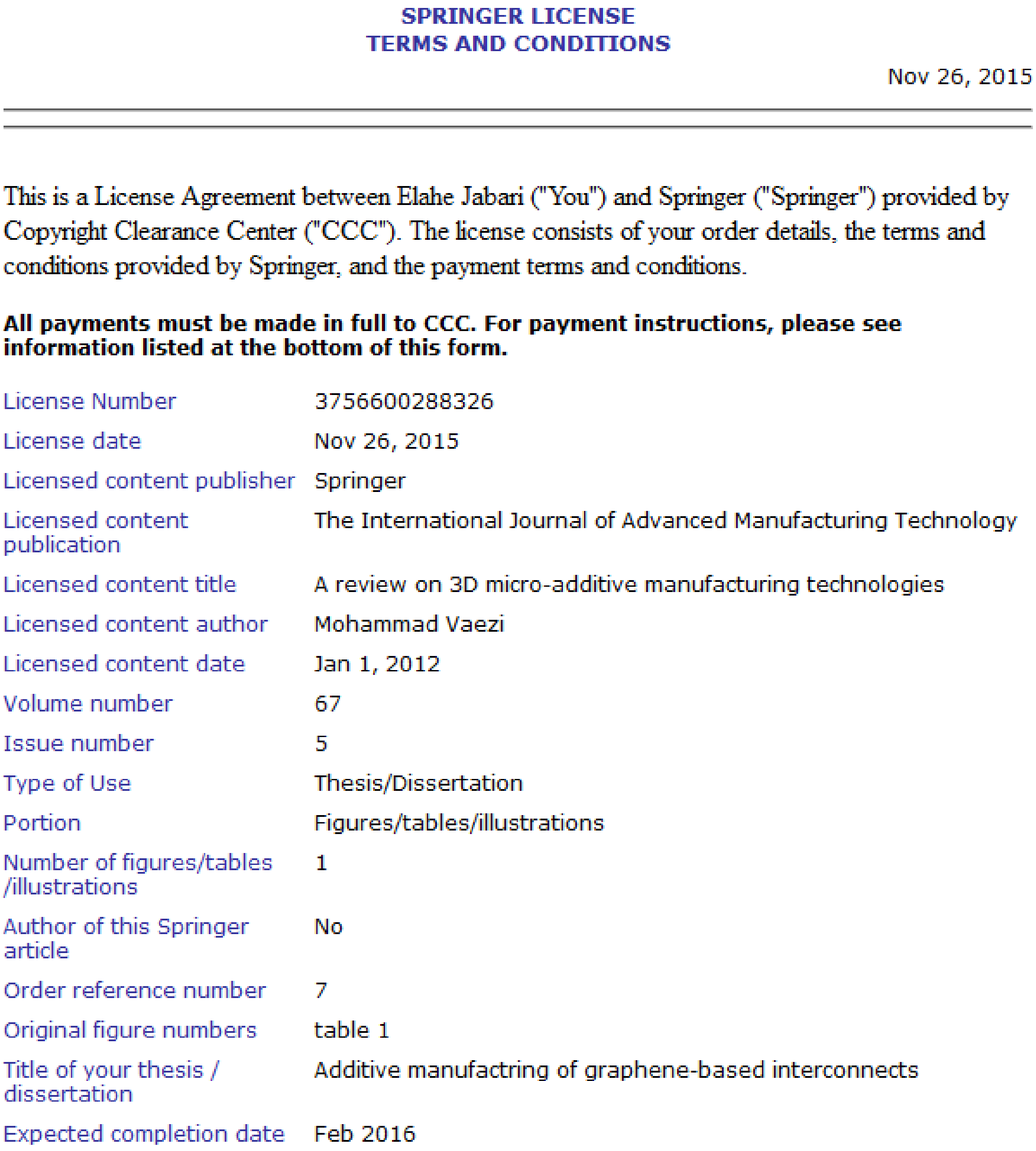

SPRINGER LICENSE
TERMS AND CONDITIONS

Nov 26, 2015

This is a License Agreement between Elahe Jabari ("You") and Springer ("Springer") provided by Copyright Clearance Center ("CCC"). The license consists of your order details, the terms and conditions provided by Springer, and the payment terms and conditions.

All payments must be made in full to CCC. For payment instructions, please see information listed at the bottom of this form.

License Number	3756600288326
License date	Nov 26, 2015
Licensed content publisher	Springer
Licensed content publication	The International Journal of Advanced Manufacturing Technology
Licensed content title	A review on 3D micro-additive manufacturing technologies
Licensed content author	Mohammad Vaezi
Licensed content date	Jan 1, 2012
Volume number	67
Issue number	5
Type of Use	Thesis/Dissertation
Portion	Figures/tables/illustrations
Number of figures/tables /illustrations	1
Author of this Springer article	No
Order reference number	7
Original figure numbers	table 1
Title of your thesis / dissertation	Additive manufactring of graphene-based interconnects
Expected completion date	Feb 2016

Figure C.9